# ABSTRACT


Title of Document: PROBING THE IGNITION MECHANISM OF ALUMINUM NANOTHERMITES

Snehaunshu Chowdhury, Ph.D., 2012

Directed By: Professor Michael R. Zachariah, Department of Mechanical Engineering, Chemistry and Biochemistry

Nanothermites are defined as intimate mixtures of metal and metal oxidizer particles usually below 100 nm in diameter. They belong to a class of energetic materials which have been of recent interest due to their high amounts of stored energy, and their potential for future use in a variety of applications. Once ignited, nanothermites undergo self-sustaining reactions. Such reactions are very poorly understood due to the lack of proper diagnostic techniques replicating the heating rates in self-sustaining reactions.

We use a temperature jump (T-jump) technique by heating a thin platinum wire to study the nanothermite reactions at heating rates of $10^5$K/s. First we study the ignition initiation mechanism in Al-CuO nanothermites and show that there is an inherent ignition delay, i.e., ignition occurs after the electric pulse is shut off. This ignition

delay increases progressively as the oxide shell thickness is increased, suggesting that the reacting species have to move across the shell. T-jump time of flight mass spectrometry (T-jump TOFMS) is used qualitatively to support such a claim. Several nanothermites are also tested for their ignition temperature. The oxidizers were chosen based on their behavior towards heating. For several oxidizers (CuO, $Fe_2O_3$, $KClO_4$ etc.) ignition in the nanothermites is noticed to occur when the oxidizers release oxygen using T-jump TOFMS. Complementary electron microscopy techniques show that Al-CuO reactions can occur even in the absence of oxygen, via reactive sintering mechanism. Furthermore, electron microscopy techniques are used to show evidence of condensed phase initiation in other nanothermites.

The role of positive ions in correlation to ignition in nanothermites is also studied for selected nanothermites using the T-jump TOFMS. Positive ions are seen to be generated during the ignition interval and are found to consist primarily of $Na^+$ ions. A hypothesis for such observation is proposed and is seen to be consistent with molecular dynamics simulations from literature.

# PROBING THE IGNITION MECHANISM OF ALUMINUM NANOTHERMITES

By

Snehaunshu Chowdhury

Dissertation submitted to the Faculty of the Graduate School of the

University of Maryland, College Park, in partial fulfillment

of the requirements for the degree of

Doctor of Philosophy

2012

Advisory Committee:

Professor Michael R. Zachariah, Chair

Associate Professor Bao Yang

Associate Professor Christopher Cadou, Dean's representative

Professor Greg Jackson

Assistant Professor Santiago Solarres




# Dedication

This dissertation is dedicated to my wife, family and friends for their unconditional support.

## Acknowledgements

I would like to take this opportunity to thank my advisor, Prof. Michael Zachariah for his consistent support throughout my years as a graduate student. His advice, in work and life in general has proved invaluable. I would also like to thank the committee members for serving in my committee and their suggestions in making this dissertation better. I am grateful to the Defense Threat Reduction Agency and Army Research Office for providing financial support necessary for conducting this research work.

I am much indebted to Dr. Lei Zhou and Dr. Nicholas Piekiel who introduced me to the basics of experimental work. In any trouble with equipment's, their helpful suggestions for troubleshooting have always been forthcoming. My sincere gratitude goes to Guoqiang Jian whose various suggestions have often been of great help to me. I am also much indebted to Dr. Kyle Sullivan with whom I had numerous stimulating discussions. I would also like to thank my group members for their help and support at various stages. To Dr. Purnendu Chakraborty, thank you for all your help since we became friends.

Finally, I am much indebted to my wife, Dolon, and my family and friends whose constant cooperation, encouragement and understanding have kept me motivated.

# Table of Contents

# List of Tables

**Chapter 3**



**Chapter 4**



**Appendix A.1**

# List of Figures

**Chapter 1**



**Chapter 2**



**Chapter 3**

**Chapter 4**

**Chapter 5**

**Appendix A.1**

# Chapter 1: Introduction

Energetics is a subject devoted to the study of the synthesis, characterization and the controlled release of energy during decomposition and/or reaction of an energetic material. Common energetic materials like nitroglycerine (NC), RDX, pentaethanotrinitol (PETN), trinitrotoluene (TNT) etc. are organic in nature. The role of the "fuel" and the "oxidizer" in such materials are served by different functional groups in the same molecule. Under heating, they decompose into several mutually reactive species leading to the formation of more stable product(s). The difference in enthalpy between the final and starting material(s) is released in the form of energy and is known as the heat of reaction. It is however very difficult to tune the release of energy from such materials as this requires manipulation at the molecular level during synthesis.

An easy way to overcome this drawback is to prepare the fuel and the oxidizer separately and mix them together to react under appropriate conditions. This allows the opportunity to choose either the fuel and/or the oxidizer individually. Metals have commonly been used as "fuels" and a very well-known case is the traditional "thermite reaction". This is a chemical reaction between aluminum metal and iron (III) oxide as the oxidizer. The heat of the reaction is high enough to melt certain metals which are not possible by conventional means. Naturally, this reaction has extensively been used for varied applications including welding railway tracks since the beginning of the twentieth century.

With recent progresses in the field of nanotechnology, it is now possible to

develop/synthesize metal particles whose dimensions are about 1-100 nanometers (nm). Such materials have become the subject of extensive research in the last decade or so because of their wide variety of possible applications ranging from the synthesis of novel materials to targeted drug delivery. Using different synthesis techniques fuel and/or oxidizer particles of sizes in the range of a few to hundred nanometers have been manufactured.

Reaction between nano-sized metal and oxidizer particles has received significant attention in the nanoenergetics research community in recent years. The primary goal of all ensuing studies is to have a clear understanding of the effect of size and other associated effects on reactivity by using "fuel" and the "oxidizer" nanoparticles. Although there is no strict cut-off limit for a nanoparticle, length scales <100 nm have commonly been used. Such intimate mixtures of nano-sized metal and oxidizer have been interchangeably referred to as nanocomposites, nanothermites, superthermites or metastable intermolecular composites (MICs) in existing literature.

## *1.1 Nanothermites*

A nanothermite is a mixture of "fuel" and "oxidizer" particles of dimensions less than 100 nm. A significant advantage of the use of metals nanoparticles as "fuel" is their high energy density. Figure 1.1 shows a graph from Fisher and Grubelich [1] demonstrating the advantage of the use metals as fuels over traditional energetic materials. Aluminum, which is a widely used metal, has approximately twice the energy on a volumetric basis than traditional explosives like TNT with any of the oxidizers although the energy release on a mass basis is almost the same.

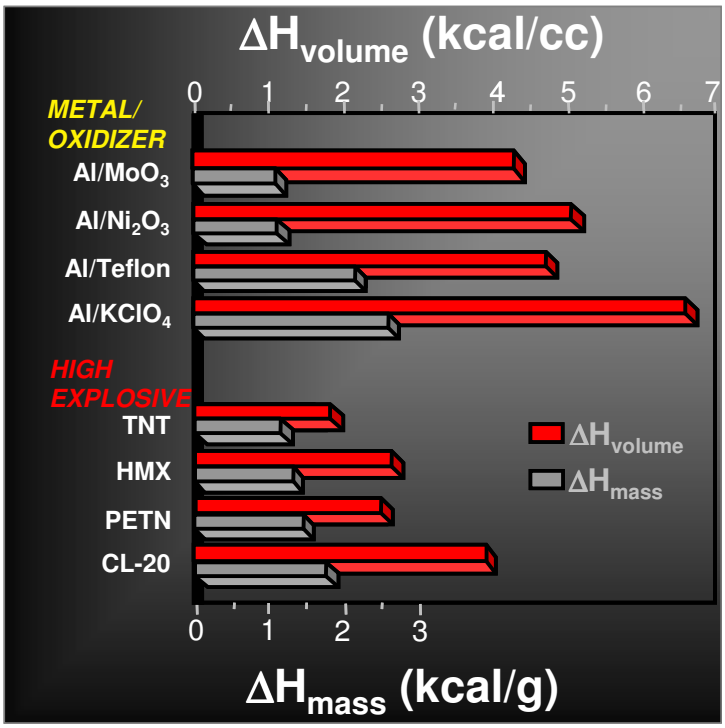


Figure 1.1 Comparison of the enthalpy of combustion on a volumetric as well as mass basis between thermites and common organic explosives [1].

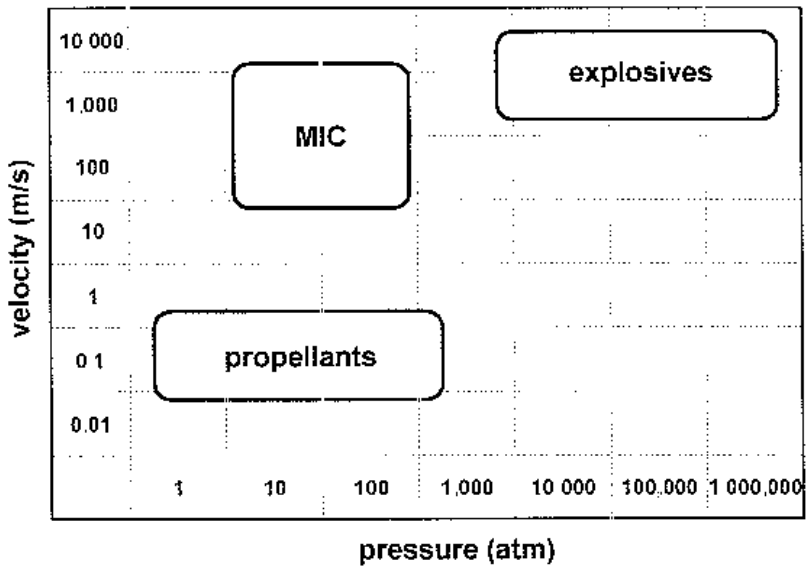


Figure 1.2 A comparison of the flame speed and pressure generated due to gas release during a MIC reaction [2]

Another important aspect of the use of nanothermites is that they generate gases which are in the intermediate range between explosives and traditional propellants. Figure 1.2, taken from Wilson and Kim [2], shows the relative gas generation abilities of nanothermites when compared with traditional organic explosives such as TNT and PETN. Clearly, the performance in terms of overpressure is not as good as the organic explosives but the MIC's bridge the gap nicely between explosives and propellants giving higher flame velocities than propellants and the same as that of organic explosives.

## *1.2 Nanoparticles*

During the last decade or so nanoparticles has been the subject of extensive research owing to their high reactivity as compared to micron-sized particles. Aumann and Skofronick [3] published the first paper reporting lower activation energy for oxidation of nanoaluminum than for bigger micron sized aluminum particles. A higher reactivity of nanoparticles in general can be attributed to the following reasons:

a) Reduced diffusion lengths: As the particles get smaller and smaller, the species do not have to diffuse across as much as they would have to for a larger particle. The diffusion lengths being smaller, the reaction timescales are faster than for larger particles.

b) Increased surface area to volume ratios: As the size of a particle gets smaller, a significantly large fraction of the atoms/molecules making up the particle reside on the surface. Figure 1.3 below shows the fraction of atoms on the bulk/surface as a function of the diameter of the iron particle [4]. As the size of the particle changes from 25 to 2.5 nm, the percentage of the atoms changes by a factor of 5. This can lead to significant changes in the thermochemistry of the metal including a reduction in melting temperature and enthalpy.

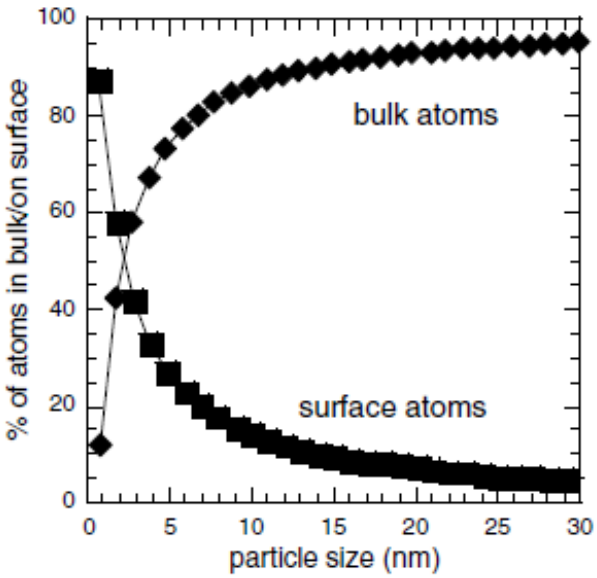


Figure 1.3 Percentages of atoms on the surface/bulk as a function of its diameter [4].

c) Surface molecules behave differently as they experience intermolecular forces only from the molecules underneath. On the other hand, molecules interior molecules experience forces from all directions. This causes the surface molecules to have larger energy as compared to interior molecules.

d) Greater Mixing: Smaller particles mix well as the length scales involved in the mixing is smaller. This produces more homogeneous mixtures.

e) Reduced melting temperature of the metal: Nanoparticles typically exhibit lower melting temperature and lower enthalpy of fusion when compared to the bulk materials. This is shown in Figure 1.4 below where the melting point of aluminum particles is plotted against particle size. For particle diameters below ~ 60 nm, the melting point starts deviating from the bulk melting point (633 $^{0}$C) of aluminum. For a 10 nm aluminum particle, the melting point is

only about 300 $^0$C, which is almost half the bulk melting temperature.

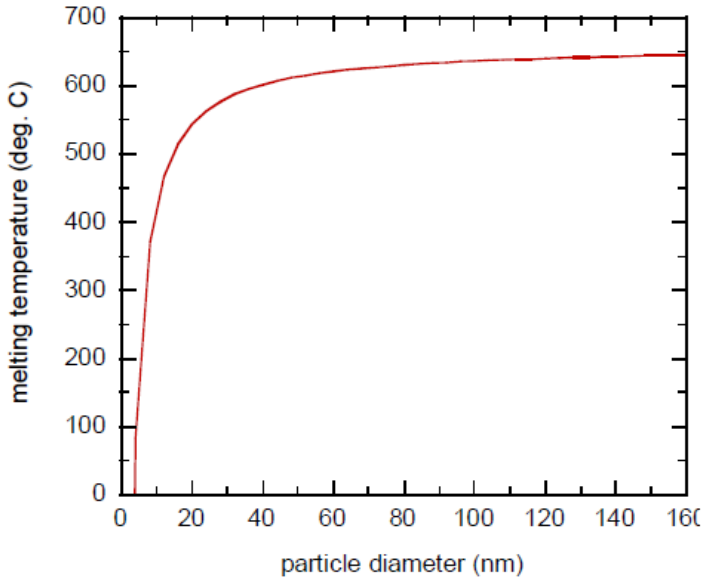


Figure 1.4 Variation of melting temperature of aluminum as a function of the particle diameter [5]. The bulk melting point is 633 $^0$C.

The reduction in melting temperature of the particle is a direct consequence of the number of molecules that reside on the surface and are subject to much less internal forces than the molecules in the interior.

f) Inherent instability of the nanoparticle: Metal particles of nanoscale dimensions are extremely reactive and a thin oxide coating is formed on them as soon as they are formed. This passivates the particles from being oxidized further under normal conditions. The thickness of the coating layer depends on the size of the particle. Figure 1.5 shows how the thickness of the oxide film on the particles varies with its size for an aluminum nanoparticle. Typically, for an aluminum particle of 50 nm diameter the oxide thickness

ranges between 2-3 nm and the effective aluminum content of the particle in terms of mass, also known as the % activity of the particle is around 75%.

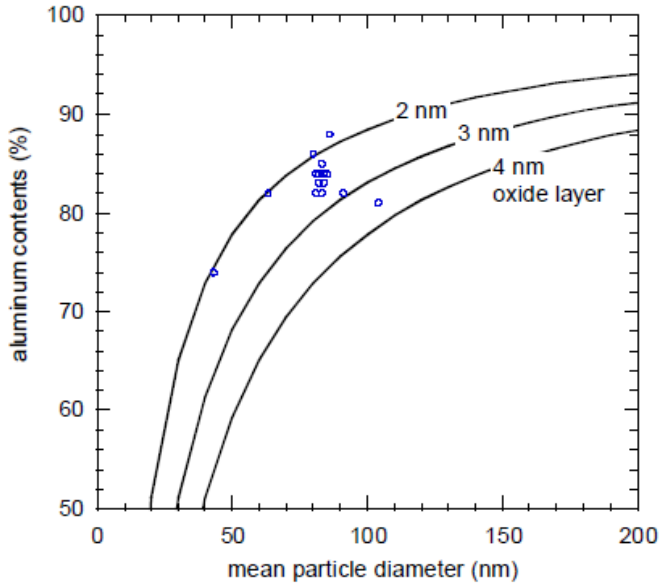


Figure 1.5 Percentage content of aluminum and the coating thickness as a function of aluminum particle diameter [5].

The presence of the passivation layer makes nanoparticles exhibit a core-shell structure. For aluminum nanoparticles, the aluminum core has a low melting temperature (933 K) whereas the oxide shell core has a higher melting temperature (2350 K). This has significant implications on the stress profiles inside the particle under heating and will be discussed in details in Chapter 3.

# Chapter 2: Common Measurement Techniques and Motivation

Research interests in nanothermite behavior have increased enormously since the first report of an increased reactivity with aluminum nanopowders was published by Aumann and Skofronick [3]. They measured enhanced reactivity in terms of the low activation energy for oxidation of aluminum nanopowders. Although activation energy is a common way of inferring enhanced reactivity, it is not the sole metric used for the purpose. Some other criteria include, but are not limited to, flame speed, reaction temperatures, ignition delay and ignition temperature. Various experimental techniques have been employed for measurement of these parameters. These are described in this chapter after a brief review of the literature on aluminum combustion.

## *2.1 Aluminum combustion*

Nanoaluminum plays a key role in nanothermites and consequently significant efforts have been dedicated to understand its combustion behavior. However, results on aluminum combustion have differed significantly, due to a large number of potential experimental variations.

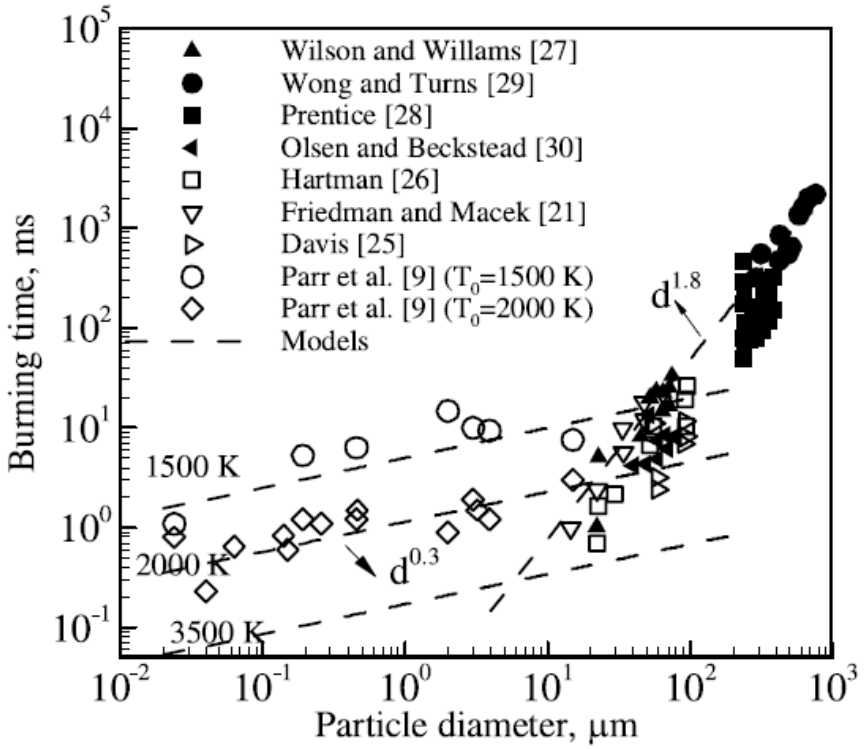


Figure 2.1 The burning time of aluminum particles as a function of their diameter [6].

Figures 2.1 and 2.2 show some examples of how the combustion kinetics in Al nanoparticles differ from those of micron sized particles, as the burn time and ignition temperature are both experimentally shown to be lower in nanoparticles. As shown in Figure 2.1 above, the burn time for particles of 5 micron in diameter or above scales with $d^{1.8}$. This is very identical to the burning of a droplet for which burn time is known to vary as $d^2$. However, burn times for smaller aluminum particles follow a $d^{0.3}$ law. The most interesting inference from the above figure is the cut-off diameter where a transition in the scaling law applies is ~ 5 micron.

Figure 2.2 plots the ignition temperature of aluminum particles as a function of their diameter. Beyond 15 micron in particle size, the ignition temperature is fixed at ~

2250 K and does not change with increase in size. This has been attributed to the fact that the shell melts around ~ 2350 K and allows for the molten core and the oxidizer to react forming a lifted flame. On the contrary, as the particle size goes below 15 microns, a decrease in ignition temperature is observed. For particles of 100 nm or less, the ignition temperature is very close to the melting temperature of aluminum.

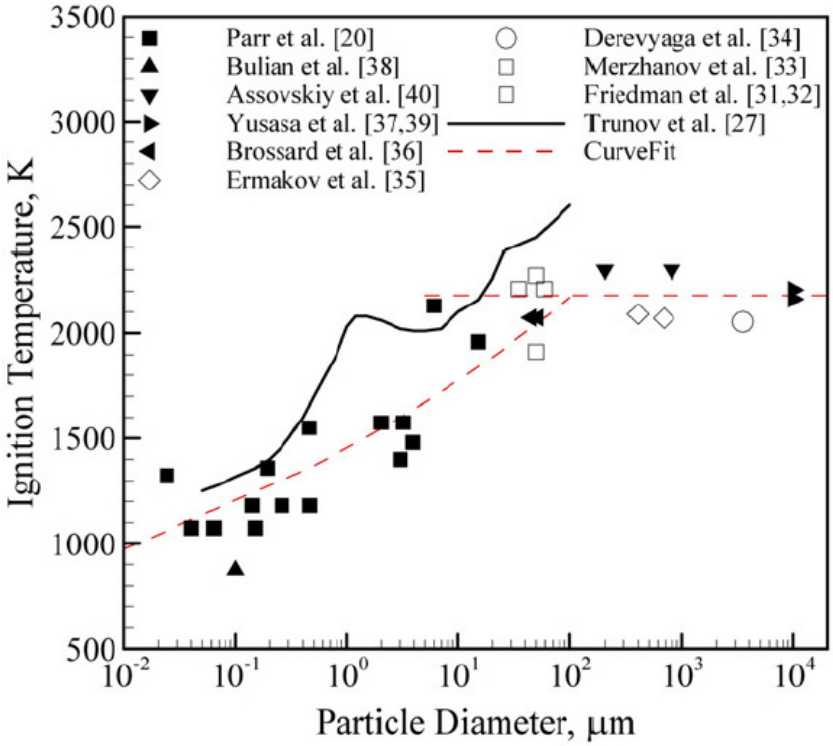


Figure 2.2 Particle ignition temperatures as a function of their particle size [7].

The pertinent question is why nanoparticles burn differently, and how do they actually initiate their ignition and combustion processes. Since aluminum nanoparticles show substantially different characteristics than micron-sized particles, and are primarily used in nanothermites, our studies will concentrate in understanding the Al nanoparticle combustion better.

A good deal of attention has been given to understanding the transport of aluminum with respect to its $Al_2O_3$ shell. Figure 2.3 shows a TEM image of the inherent $Al_2O_3$ of an aluminum nanoparticle. This shell is typically 2-5 nm in thickness, but can be grown larger in different environments. The $Al_2O_3$ shell essentially acts as a protective barrier for the aluminum fuel and prevents further oxidation of its core. In order for the core aluminum to undergo a reaction, it must either escape from the $Al_2O_3$ shell, or an oxidizer has to diffuse through. During slow heating, aluminum ions can diffuse outwards out of the $Al_2O_3$ shell, and $O_2$ can diffuse inwards, thus making the reaction diffusion controlled.

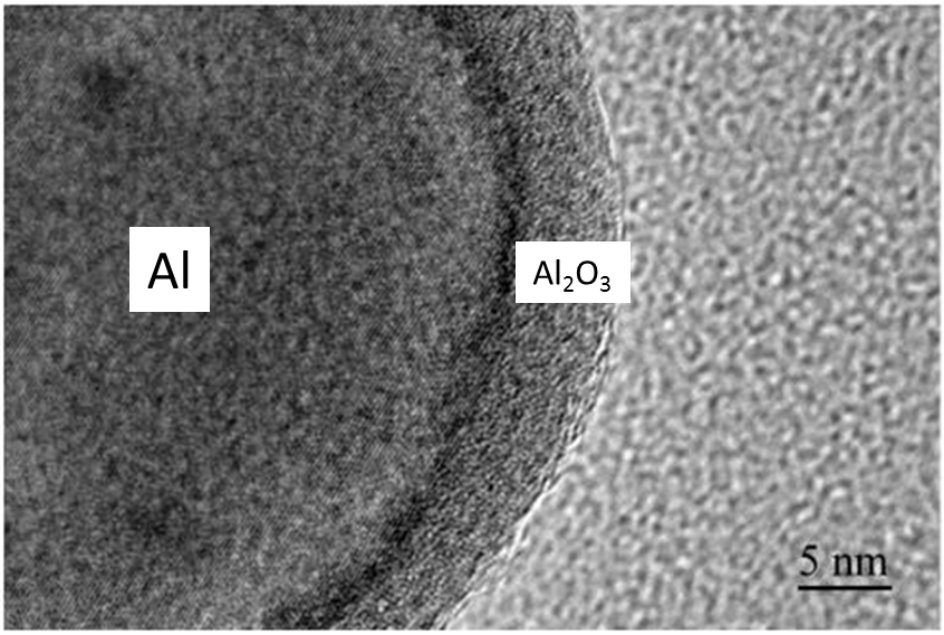


Figure 2.3 TEM image of aluminum ~50 nm aluminum nanoparticle [8].

If the aluminum nanoparticle is rapidly heated, the nearly instantaneous melting of the aluminum could have considerable effects in aiding the transport processes. The

exact nature of aluminum transport in this case is unknown, but several models have been proposed.

Levitas *et al* suggest that aluminum escapes from the oxide shell via a "melt dispersion" mechanism [9, 10]. This mechanism proposes that under rapid heating conditions as the aluminum core melts, and the alumina shell remains in the solid phase, the aluminum volumetrically expands by up to 6% creating an intense force on the outer shell. The $Al_2O_3$ shell ruptures and creates an unloading wave through the molten Al, which creates a spallation into bare Al clusters that travel at speeds of up to 250 m/s. Based on a more moderate heating rate experiment, Rai *et al* proposed a diffusion based model to help explain the appearance of hollow core aluminum particles after heating [11]. They suggest that oxidation of nanoaluminum occurs in two regimes, a slow regime and a fast oxidation regime. The oxidation in the slow regime occurs below the melting point of aluminum while oxidation in the fast regime occurs above the melting point of aluminum. The slow heating regime occurs when the Al core is still in the solid phase and is primarily dependent on oxygen diffusion through the $Al_2O_3$ core, while the fast oxidation occurs after the melting of Al and depends on the diffusion of both oxygen and aluminum, and can be further enhanced by breaking of the alumina shell. While Levitas suggests that the extreme pressure within the alumina shell causes spallation of the aluminum core [10], Rai suggests that this pressure serves to enhance the diffusion through the shell [11]. For the ignition of an aluminum nanoparticle, a mechanism involving cracking of the alumina shell has also been suggested by Trunov *et al*. [12]. This mechanism is designed to explain the burning of a wide variety of aluminum particles, at the micro

or nanoscale, and is based on the transforming morphology of the $Al_2O_3$ shell. For nanoparticles they suggest that the alumina shell can quickly transform from the amorphous phase to γ-phase. This caused a volumetric change in the shell coverage and produce cracks in the shell exposing the bare aluminum for oxidation [13].

There has been much debate on the mode of aluminum transport through the $Al_2O_3$ shell. This transport is even believed to depend on the heating rate of the aluminum nanoparticles. It was suggested by Dreizin [14] that at low temperatures the oxidation rate of aluminum is governed by the inward diffusion of oxygen while at high temperatures the oxidation is predominantly due to the outward diffusion of aluminum through the shell. Rapid heating of an aluminum nanoparticle to high temperatures melts the aluminum core and it can be concluded that this increased the mobility of aluminum leading to a positive effect on the transport of aluminum. With enhanced transport of aluminum, oxidation occurs at a much faster rate and if the transport rates are really high, the reaction eventually becomes limited by the kinetics of the reaction. In some nanothermite systems, where rapid combustion occurs, inherent heating rates can reach up to $10^6$ K/s [10]. Thus self-heating of the nanothermite allows for fast transport processes and promotes further reaction. It is difficult to investigate the intermediate steps of these reactions as they occur very rapidly along with a high amount of energy release. The various experimental techniques used to study nanothermite reactions are given in the next section.

## *2.2 Experimental Techniques*

### 2.2.1 Thermal Analysis Techniques

The most common technique that has widely been used in the study of nanothermite reactions are thermal analysis techniques. These include thermogravimetric analysis (TGA) and digital scanning calorimetry (DSC). These techniques are used to heat up the required samples to a prescribed temperature at a fixed heating rate. The heating rate is usually low and is on the order of 1-50 K/s. TGA is used to study the onset of gain/loss in weight of the sample due to oxidation/dehydration during the heating profile. This gives an accurate representation of the temperature at which oxidation starts. No change in weight is recorded in case of phase change of the material. On the other hand, DSC traces show the heat release/intake by the sample as a function of temperature. Melting is thus easily identified by an endothermic event. The total area under the DSC trace provides the amount of heat gained/lost during the various changes undergone in the prescribed temperature range. Kinetic analysis could also be performed from the DSC scans. These are detailed in references [13, 15-17]. DSC scans are thus helpful in identifying the start of a chemical reaction/phase change as these events are known to be either exothermic or endothermic.

### 2.2.2 Instrumented Burn Tube Tests

Instrumented burn tube tests were first reported by Bockmon [18, 19]. This is a setup containing a set of pressure and optical probes at fixed axial distances on diametrically opposite sides of an acrylic tube. The tube is filled with the material of

interest and is ignited at one end. The location of the flame front is identified by a sudden rise in the corresponding optical and pressure sensor placed at the axial location. From knowledge of the distances between the sensors and the time of arrival the flame speed could be calculated. For example, flame speed for Al/CuO nanothermites has been measured to be ~ 800 m/s which are typically 3 orders of magnitude faster than HMX, which is a popular traditional energetic material. However, a severe drawback of this technique is that the heating rate is not directly known.

### 2.2.3 Shock tubes

Shock tube tests are a way of studying the reactions in nanothermites under rapid heating [20, 21] rates on the order of $10^6$ K/s. The nanothermite of interest is kept on a knife edge and is heated by the passage of a shock over it. The shock is generated in a tube partitioned by a diaphragm. On one side of the diaphragm the sample is kept at atmospheric pressure in the required gas environment. The other side of the diaphragm is filled with a pressurized gas. Conditions are so maintained that the pressure ratio on both sides of the diaphragm gives rise to a shock wave. The sample is heated as the shock wave passes over it. The heating rate depends on the strength of the shock which is a factor of the pressure and density ratio of the driver to the driven gas. Heating rates achieved using this technique is ~$10^6$ K/s. However, this setup requires extreme safety care owing to the high pressure waves generated. Another drawback of this setup is that reacted material is tossed around and cannot be collected for microscopy or material analysis.

### 2.2.4 Laser Heating

Lasers serve as a coherent source of energy capable of being focused over a very small area of interest. Hunt and Pantoya [22] used a carbon dioxide ($CO_2$) laser to heat pellets of nanothermite mixtures as well as micron sized particles. Ignition delay times for nanothermites were found to be 2-3 orders of magnitude lower than micron sized counterparts. Lower ignition delay indicates enhanced heat transfer characteristics of the pellet and could be adjudged as another indication of improved reactivity of nanothermites/nanopowders.

In chapter 3 of this work, we will show how ignition delay could be used to infer a diffusion based ignition mechanism for Al-CuO nanothermites. However, our definition of ignition delay is different from what has been traditionally used and is elaborated in chapter 3.

### 2.2.5 Cryogenic High Heating Rate TEM/SEM Stage

This is a heating holder designed primarily for heating samples at ~ $10^6$ K/s by passing an electrical pulse and cooling the sample down instantly for morphological studies by in-situ transmission electron microscopy (TEM). Details about the principle of operation could be found in reference [8, 23]. Only the final products are known and could be studied under TEM. In this method, a reaction event is characterized by a change in morphology associated with products characterized by elemental mapping. This holder is yet to be available commercially in the market and has only been available for limited studies.

### 2.2.6 Ignition studies

Ignition temperature is an inherent property of a nanothermite. It is the temperature at which the material turns to a heat source via chemical reactions as opposed to a heat sink. Once the material attains ignition temperature, the reaction becomes self-sustaining and a thermal runaway occurs. This is usually associated with the release of a lot of heat and light.

A controlled way of measuring the ignition temperature of nanothermites experimentally is by using what is known as the wire ignition experiments. A thin wire is heated electrically by passing a known current through it. The temperature of the wire at any instant of time could be determined by using a pyrometer as in reference [17] or by correlating the resistance of the wire to the temperature. The nanothermite of interest is coated on the wire and ignition event is monitored using a photodetector. However, the highest heating rate reported by this method prior to our work is on the order of $10^4$ K/s [17].

## *2.3 Motivation*

The motivation for conducting the work presented in this dissertation is twofold. Firstly, as mentioned earlier in this chapter, the understanding of the combustion mechanism for aluminum nanoparticles is not well understood. Secondly, although there has been a lot of research in the combustion of aluminum nanothermites, most of the studies have been conducted under low heating rates due to the lack of experimental techniques to characterize nanothermite reaction at high heating rates. Low heating rates are not the typical application conditions as these self-sustaining

nanothermite reactions are expected to occur in the range of $10^4$-$10^8$ K/s. Consequently, there is a lack of data under high heating rates in a very controlled manner. This becomes all the more important when one considers the fact that ignition temperature of nanothermites have been reported to be dependent on the heating rate employed. In the work described here, we have designed an experimental setup based on the temperature jump (T-jump) method by electrical heating of a wire to study the effect of high heating rates on the ignition mechanism as well as the ignition temperature of various nanothermite mixtures. Unless otherwise mentioned, all experiments are conducted at a heating rate of ~ 1-5 x $10^5$ K/s.

The work presented here follows a top-down approach. First, the work in Chapter 3 investigates the ignition mechanism which has been postulated to depend on heating rate. Using the results of Chapter 3, an attempt is made in Chapter 4 to explain the experimentally observed ignition temperatures and arrive at a phenomenological understanding of the nanothermite reactions. Chapter 5 investigates the ignition mechanism in the light of ion generation due to the intense electrical fields associated at the interface of the core and shell of an aluminum nanoparticle upon heating. Finally, a summary of conclusions and recommendations for future work are proposed in Chapter 6.

# Chapter 3: Diffusive vs. Explosive Reaction at the Nanoscale

Nanoscale particles composed of a metal and metal oxide can undergo a violent thermite reaction. Furthermore it is well known that making the particles smaller increases the reaction rate dramatically. An example of such a system is aluminum (Al) + copper oxide (CuO), which under stoichiometric conditions yield an adiabatic flame temperature of ~ 2840 K, with an energy density more than a factor of 3 over TNT on a volumetric basis. Nevertheless because of the interrelationship between many complex processes occurring, considerable debate continues as to the nature of initiation of the thermite event. Close proximity between the fuel and oxidizer reduces the diffusion length and increases the reaction rate [18]. Fuel nanoparticles usually have lower melting point than their micron size counterparts [5, 24, 25] making them easier to ignite. However, for very small particles, heat transfer rates are extremely fast and hence reaction characteristics such as onset of reaction, ignition temperature, ignition delays etc. are known to depend on the particle size [16, 26, 27].

We consider the Al/CuO nanoscale thermite system as representative of the wide class of such reactions. The aluminum fuel component is actually a core shell structure of an aluminum core with an aluminum oxide passivation layer. Typically such layers are on the order of a few nanometers [2]. The interaction between the low melting core and high melting shell is critical in understanding the ignition mechanism at the nanoscale. Nominally, we consider the nanoscale regime to be those where both components (metal and metal oxide) are below 100 nm in diameter.

Reactions in general have been known to be fall in one of the following two regimes:

a. Diffusion controlled

b. Reaction or kinetics controlled.

These reaction regimes and their relevance to aluminum combustion are discussed in more details in the sections below.

### *3.1 Diffusion Related Regime*

Combustion in this regime is characterized by reaction timescales which are limited by the mass transport of the reactants to the reaction zone. Burning of micron sized aluminum in an oxygenated environment is an excellent example of a diffusion controlled reaction where homogenous reaction takes place in accordance with the Glassman criterion [28]. The flame front is lifted off the surface of the aluminum particle as the flame temperature is above the boiling point of aluminum (2791 K). Ignition studies [13, 20, 21, 29-32] on micron size aluminum have revealed that the ignition temperature is close to the melting point (2350 K) of the metal oxide ($Al_2O_3$) shell.

As the diameter of the aluminum particle is reduced, the transport rates are enhanced and the reaction may occur in the condensed phase. The primary mechanism for such a reaction is governed by the diffusion of aluminum ions and oxygen ions across the solid oxide layer. A mechanism that has been suggested previously is known as the shrinking core model [33]. Depending on the relative diffusion rates, aluminum ions can move across the shell and react with oxygen or

oxide ions can diffuse into the particle and react with the aluminum core. In the former case, the reaction takes place on the surface of the particle while in the latter case the reaction front is inside the particle. The matter is even complicated as the ignition temperature of nano-aluminum thermites have been expected to depend on the heating rate.

When probed by conventional dynamic thermal techniques at low heating rates (1-10's of K/s) by thermogravimetric analysis (TGA) or digital scanning calorimeters (DSCs), reaction of nanoaluminum has been shown to start much below its melting temperature in many studies. Umbrajkar et al. [17] reports evidence of Al and CuO nanothermite reactions occurring at temperature as low as 400 K in thermal analyses experiments. Pantoya et al. [15] conducted thermal analyses on nano-Al+$MoO_3$ and results suggest the onset of reaction at ~ 540 K. Trunov et al. [34] suggests that low temperature oxidation of nano-Al occurs due to the polymorphic phase changes of the natural oxide shell present on the particle and is limited by diffusion across the oxide shell. Past studies in our group by Park et al. [35] did not find any evidence of reaction below 973 K while heating nanoaluminum in air. Rai et al. [36] has shown that even with low heating rate, the aluminum core melts and exerts pressure on the oxide shell causing it to crack (not violently). However, the reaction rate in such systems is not high enough to lead to thermal runaway and ignition. Furthermore, it is very well known that such results can be altered due to the heat and mass transfer effects which are hard to account for [37, 38]. Consequently, investigations with faster heating rates are preferred.

Ignition studies in reference [17] with heating rates ranging between $10^3$-$10^4$ K/s showed ignition of nano-Al+CuO to occur below or around the melting temperature of bulk aluminum. In shock tubes with heating rates of ~ $10^6$ K/s the ignition temperature of nanoaluminum has been observed to be in the range 1200-2100 K at elevated pressures [20]. Nanoaluminum, thus, has been reported to have a wide range of ignition temperatures suggestive of a different initiation mechanism as compared to micron sized aluminum which requires melting of the aluminum oxide shell.

For heating rates exceeding those of the shock tube, a very different model has been proposed. This is known as the melt dispersion mechanism and is discussed in the next section.

### *3.2 Kinetics Controlled Regime (Melt Dispersion Mechanism)*

Melt dispersion mechanism (MDM) was proposed by Levitas et al. [10] to account for the high reaction rates observed for nanoaluminum under very rapid heating on the order of $10^7$-$10^8$ K/s. According to this mechanism, the aluminum core (melting point = 933 K) would melt upon heating. Melting causes an increase of 12% in the volume of the core [36]. This creates huge internal pressure on the solid oxide shell. The shell is thus under tensile stress while the molten aluminum core is under compression [36]. As the internal stress exceeds the yield strength of the oxide, the shell ruptures violently releasing the molten aluminum in small clusters of a few nanometers in size. This sudden exposure to the oxidizer presents no diffusion barrier to the fuel and the reaction is therefore entirely kinetically controlled. The fast reaction is hypothesized to be the result of short distance scales present at the

nanoscale regime and a sudden exposure of the fuel to the oxidizer with no diffusion barrier.

There are several controlling parameters that can contribute towards this mechanism. Some of them, as outlined by Levitas et al. [9] are:

a) Ratio of the core to shell thickness: This is the most important parameter that would determine the occurrence of melt dispersion mechanism. For melt dispersion mechanism to occur, a critical core to shell thickness ratio of ~ 20 is required. Going below this limit does not promote the mechanism; however going above this critical number reduces the chance of melt dispersion mechanism.

b) Thickness of the shell: This is an important parameter controlling the melt dispersion mechanism. In this mechanism, the shell was treated as a single crystal and assumed to be free of any defects primarily due to its small thickness in 2-6 nm range. Increase in thickness would introduce defects in the crystal thereby lowering its yield strength.

c) Temperature of formation of the shell: The temperature at which the shell forms governs the porosity of the shell. For aluminum nanoparticle, the oxide shell thickness typically ranges between 2-6 nm. The yield strength of the shell is assumed to be on the order of a few gigapascals (GPa).

It must however be noted that our current understanding about the exact physical mechanism is far from being complete. A resolution of the two opposing views is the work described in this chapter. Levitas et al. [10] has suggested that an initiation event via the melt dispersion mechanism would be promoted if the temperature of formation of the oxide shell is increased. The above ideas are tested through a simple

experiment where nano-Al is mixed with copper oxide (CuO) in stoichiometric proportions taking into account the amount of active aluminum. The assessment of the prevailing mechanism is done by systematically changing the thickness of the oxide shell to determine the ignition temperature and characteristic reaction time.

It is important, before proceeding further, to define some terminologies. Ignition temperature is defined as the temperature at which a particle/mixture can sustain chemical reaction on its own, without the aid of an external heat source. Ignition temperature is a strong function of experimental conditions as well as material property.

## *3.3 Experiment*

In this study we prepare mixtures of Al/CuO nanoparticles that are coated onto a fine wire. The wire is rapidly joule heated using a pre-programmed voltage pulse and the point of ignition is recorded with a photomultiplier tube. In separate experiments with the same samples, time resolved time-of-flight mass-spectrometry is carried out us to obtain temporal speciation during the reaction. The key point is the preparation of metal with different oxide thicknesses, and our ability to accurately measure temperature during heating rates of ~$10^5$ K/s.

### 3.3.1 Sample Preparation

Commercially available aluminum powder ALEX procured from Argonide Corporation has been used in this study. The particles have a nominal size of ~50 nm with an active aluminum content of ~70% determined by thermogravimetric analysis (TGA). This would indicate an aluminum oxide shell thickness of ~ 2 nm which is

consistent with TEM analysis. This also corresponds to a core to shell ratio of 11.5 which is well below the critical limit specified in [9]. To increase the oxide thickness, particles were oxidized at 500 $^0$C, (i.e. below the melting point of aluminum) for various lengths of time, and subsequently weighed to determine the oxide growth. This ensures that the oxide shell thicknesses are formed at the same temperature, an important criterion in the melt dispersion mechanism. The shell thickness is calculated based on the weight gain and assuming spherical particles and bulk densities for Al and $Al_2O_3$. The process was repeated until the gain in weight corresponded to thickening of the oxide shell to ~3 nm and 4 nm. The active aluminum content in those samples is thus changed to 59 and 50 % respectively. These measurements have an accuracy of ±3% limited by the precision of the mass balance (0.1 mg). Table 1.1 shows the preparation procedure and the % aluminum by wt. in the prepared aluminum nanoparticles.

Table 3.1 Preparation and composition of the three samples

| Sample | Time in preheated furnace at 500 $^0$C (mins) | Shell Thickness calculated from weight gain (nm) | Activity (%) |
|---|---|---|---|
| 1 | - | 2* | 70 |
| 2 | 5 | 3 | 59 |
| 3 | 10 | 4 | 50 |

* Estimated from weight gain measurements by thermogravimetric analysis.

A question whether the particles retain their spherical shape after heat treatment is relevant at this point. Since the product ($Al_2O_3$) has different density than the starting material (Al), it is possible that a change in volume could shrink the particle

and not necessarily grow it. A quick back of the envelope calculation calculating the volume of the $Al_2O_3$ formed is shown in Table 3.2 below. The initial particle is assumed to be of diameter 50 nm, and a shell thickness of 2 nm. The mass of aluminum reacting with oxygen to form $Al_2O_3$ is calculated from the stoichiometric equation

$$4Al + 3O_2 \rightarrow 2Al_2O_3$$

Table 3.2 Calculation showing the relative change of volume when Al oxidizes to $Al_2O_3$.

| Change in core thickness (nm) | Vol of Al ($x10^{24}$) ($m^3$) | Mass of Al ($x10^{21}$) (kg) | Mass of $Al_2O_3$ ($x10^{20}$) (kg) | Volm of $Al_2O_3$ ($x10^{24}$) ($m^3$) | Increase in volume (%) |
|---|---|---|---|---|---|
| 0.5 | 3.25 | 8.78 | 1.66 | 4.15 | 27.5 |
| 1.0 | 6.36 | 17.2 | 3.25 | 8.11 | |
| 1.5 | 9.34 | 25.2 | 4.76 | 11.9 | |
| 2.0 | 12.2 | 32.9 | 6.21 | 15.5 | |

The above calculation makes it clear that there is an increase in volume due to the oxidation of the core. This creates additional tensile forces on the shell. The shell would thus crack if the forces exceed the yield strength of the shell. A 28% volume change would cause a particle of 46 nm core to expand to a particle of 58 nm diameter. However due to the inflexibility of the shell, the chemical reaction would exert extra pressure on the shell.

In order to calculate this extra pressure, we treat this single aluminum particle as a

pressure vessel having a pressure P (~ 1 GPa, from molecular dynamics simulations in [39, 40] ) on the inside surface of the shell. There is a tensile stress created on the shell due to this pressure and is known as hoop's stress. The hoop's stress σ is tensile in nature on the shell and is given by

$$\sigma = Pr/t$$

where P is the radial stress on the shell (internal gage pressure as the core aluminum exerts pressure ), r is the radius of the particle and t is the thickness of the shell. In our case, r/t = 23 nm/2 nm = 11.5. So the initial hoop's stress on the particle before heating is ~ 11.5 P = 11 GPa. The pressure due to change of volume is usually accounted for by what is known as the hoop's stress. A 28% increase in volume would have increased P at the most by 28%. However, under these circumstances, r/t = 29 nm/2 nm = 14.5. The hoop's stress is thus given by

$$\sigma = (1.28P)*14.5 = 18.6 \text{ GPa}$$

The hoop's stress is thus more when we heat the particle and the particle has greater chance of cracking as the internal pressure has increased. However, it must be remembered that this process has taken place extremely slowly, on the order of minutes. This would cause thickening of the shell and hence the use of 2 nm shell thickness is probably not appropriate and overestimates the hoop's stress. We use TEM images to show that the final product does not exhibit any cracks in the shell.

Transmission electron microscopy (TEM) was conducted on sample 3 to look for morphological changes. This is done as sample 3 would have the maximum change in volume and hence the chances of cracking the shell are also higher. Figure 3.1(a) below shows a particle with ~ 70 nm in diameter after heating. The oxide layer is not

clearly visible. Figure 3.1 (b) shows the close up view of the same particle. The shell is noticed to be about 6 nm in thickness including a contamination layer of about 1.5 nm. The most important aspect to notice in those images is that the aluminum particles retain their spherical shape on heating. Cracking of the shell is not observed and the shell maintains its structural rigidity. It is possible that several micro-cracks are formed during the heating process, but due to the slow heating rate, oxygen in the atmosphere can diffuse in and heal up the cracks leaving no visual evidence. It should also be remembered that the formation of cracks in this case would purely be due to the shrinkage of the core. Since the temperature of oxidation is maintained at 500 $^{0}$C, no additional tensile stresses are generated (in addition to what mentioned above) as this temperature is well below the melting point of aluminum causing no additional volume change.

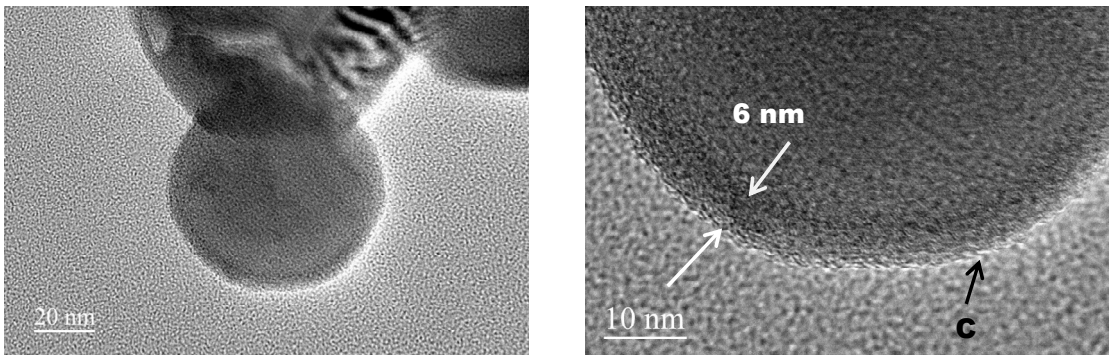


Figure 3.1 (a) TEM image of a 70 nm particle after heating (b) Close up view of the shell. The shell is almost 6 nm with ~ 1.5 mm carbon contamination layer.

Appropriate amount of copper (II) oxide nanopowders (<50 nm size) from Sigma Aldrich is weighed and mixed with the aluminum powders with different shell thicknesses to make 3 stoichiometric mixtures. Hexane is then added to the samples and sonicated for ~ 30 minutes to intimately mix the fuel and oxidizer.

### 3.3.2 Experimental Setup

A very thin platinum wire (length ~ 12 mm, diameter ~ 76 um) is joule-heated by a tunable voltage pulse generated by a home built power source. For any applied voltage (i.e. heating rate) the temperature to which the wire is heated can be controlled by varying the amplitude of the pulse. The current passing through the circuit is measured transiently by a current probe. Figure 3.2 shows a schematic representation of the setup used for the experiments.

The ignition event is recorded using a photomultiplier tube (PMT), and is identified by the appearance of a sudden emission of light above the background signal from the heated wire. In the context of this work, ignition delay is defined as the time difference between the appearance of the ignition signal, identified as a sharp spike in the optical detector, and the end of the applied voltage pulse.

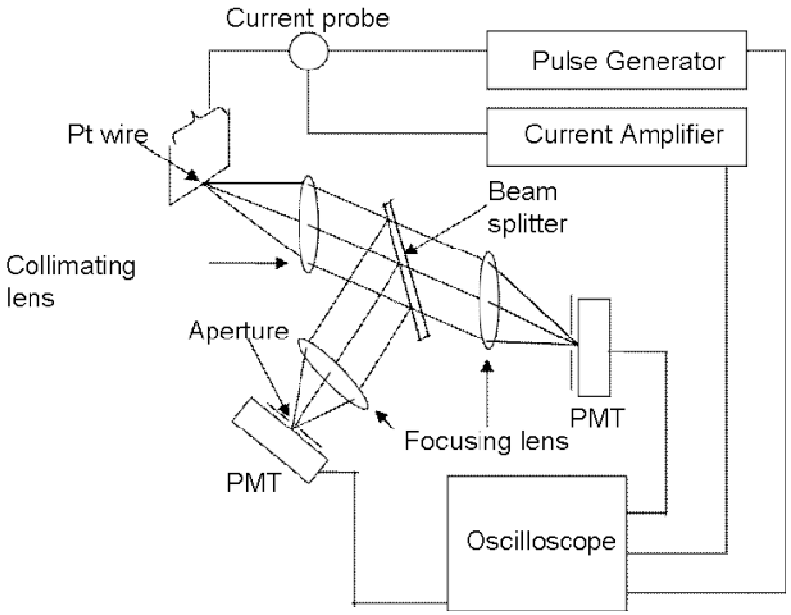


Figure 3.2 Schematic of the experimental setup

The average resistance of the platinum wire is calculated from the voltage and current history. From the resistivity of the wire, its temperature history could be established from the well-known Callendar-Van Dusen equation [41] given below or from calibration as mentioned in Appendix A.1.

$$R_T = R_{T=0}(1 + 3.907x10^{-3}T - 5.91x10^{-7}T^2)$$

where $R_T$ = Resistance at T K and $R_{T=0}$ = Resistance at 0 ℃ for the given length of the platinum wire. The resistance of the wire at 0 ℃ is calculated from the relation

$$R_{T=0} = \frac{\rho L}{A}$$

where ρ, L and A are the known resistivity, length and cross sectional area of the wire at 0 $^{0}$C. In our calculations, we have ignored any change in length and cross sectional area.

The heating rate of the wire is given by the ratio of the difference in temperature between the end and start of the pulse to the duration of the pulse. A new wire is used each time a sample is heated.

A small portion of the central region of the wire (~5 mm) is coated with the samples using a micropipette and the hexane is allowed to evaporate. Once the hexane dries off, the coating left on the wire is very dense. Figure 3.3 shows a SEM image of the central region of the coated wire.

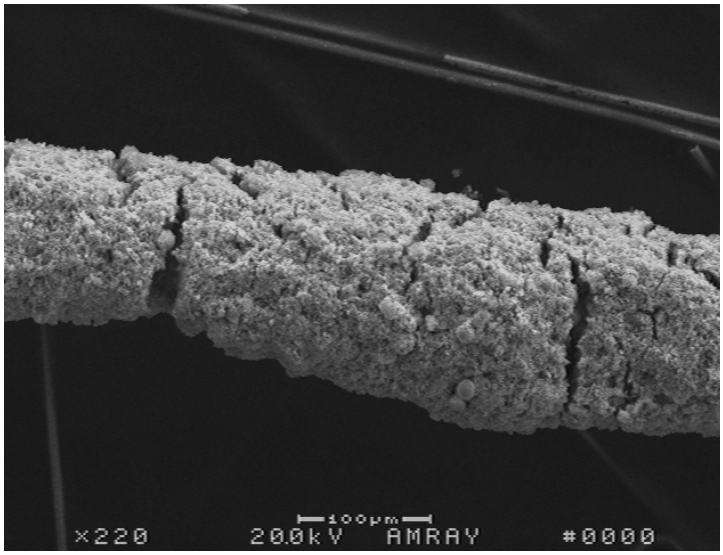


Figure 3.3 An SEM image of a coated wire. The wire is approximately 76 micron thick and the coating is another 50 microns at the thickest part.

The thickness of the platinum wire is ~75 microns and the average coating thickness as estimated from Figure 2.2 is ~ 25 microns.

### *3.4 Results*

Figure 3.4 shows the temperature of the wire and the PMT signal recorded as a function of time for such an event, for the three samples in Table 1 under condition of a heating rate of $1.7 \times 10^5$ K/s. Heating rates were fairly repeatable with uncertainty ~ $10^4$ K/s. The uncertainty associated with the measurement of temperature is ± 50 K. The sharp rise in the PMT signal indicates the start of the reaction. The results show an apparent increase in ignition temperature from 1050 K to 1200 K as the shell thickness is increased. It should be noted that the wire temperature is being ramped past the ignition temperature in this case.

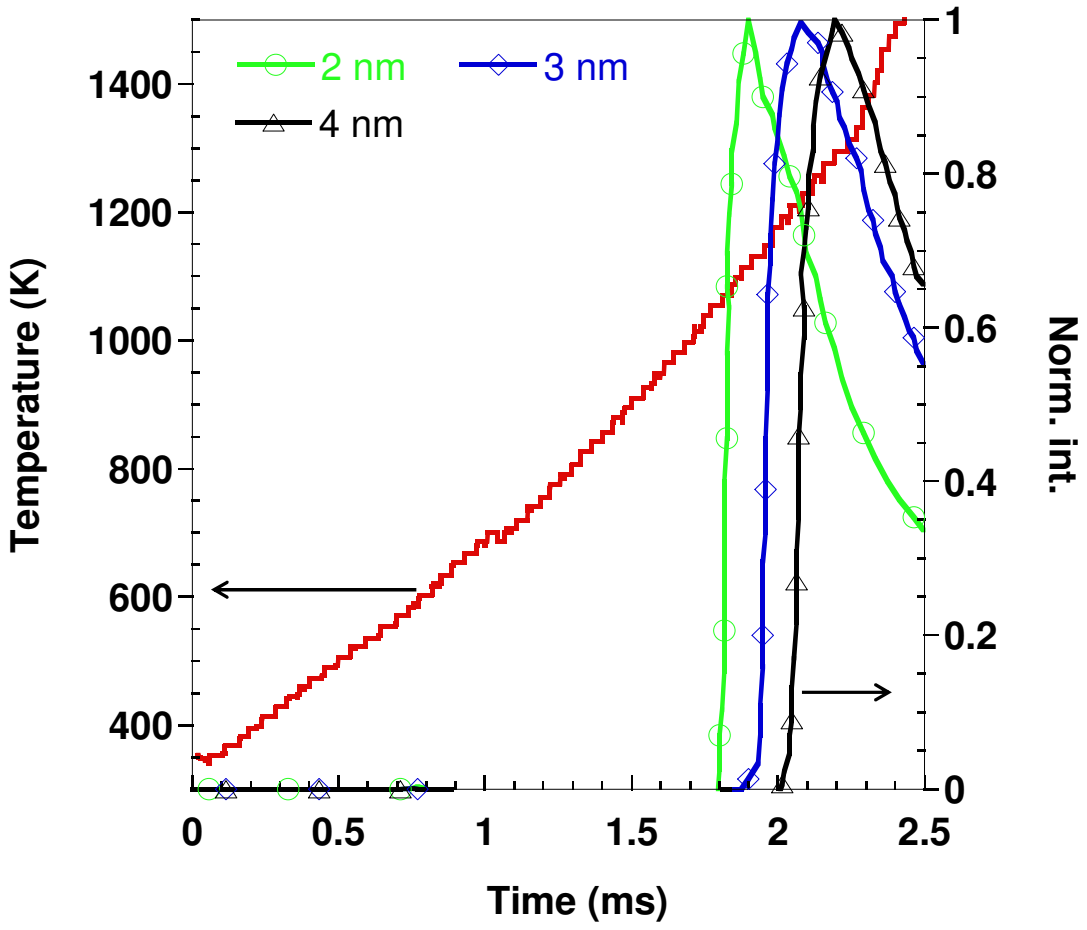


Figure 3.4 The ignition temperature for samples 1, 2 and 3. Heating rate is ~ $3x10^5$ K/s.

In a second experiment we vary the heating rate of $1.7x10^5$ and $5.2x10^5$ K/s and plot the result in Figure 3.5 for a particle with a 2 nm shell. Clearly observed is that the ignition temperature is heating rate independent in the range of heating rates carried out in this study. Similar behavior is observed for sample 2 and 3. The maximum heating rate is limited by the power supply and the shortest pulse duration that would not melt the platinum wire.

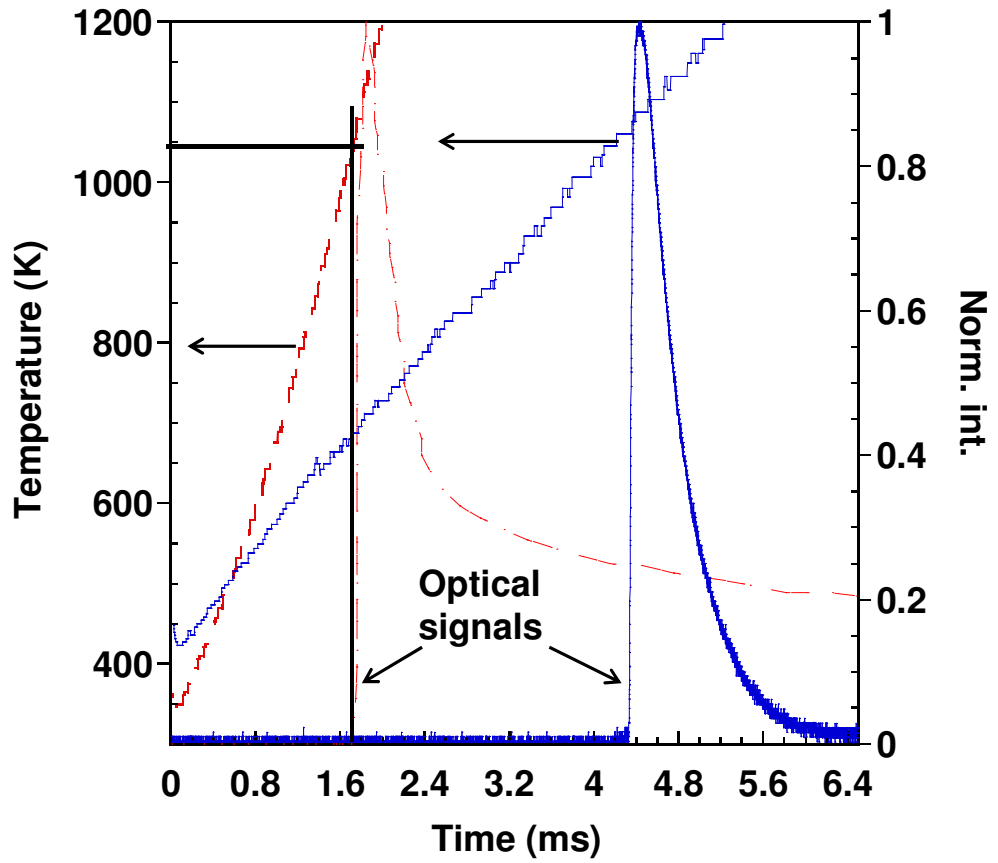


Figure 3.5 Ignition temperature of sample 1 at heating rates of $1.5x10^5$ (red dotted line) and $5x10^5$ K/s (blue solid line).

A next set of experiments are conducted in which we shut off the off the voltage pulse at a temperature below where the optical emission was observed in Figure 3.4. What we observed was that the powders could still be ignited even after the pulse had been shut off - *there is a very clear delay associated with ignition.* We define the ignition delay as the time difference between when the pulse is shut off and the onset of optical emission. The maximum temperature of the wire is 1015 K in all runs, and was decided by iteratively lowering the maximum temperature until just before no

ignition was seen. Therefore, we are only heating the particles just to their ignition temperature and then observing as the ignition subsequently occurs.

The experimental data for the three different oxide shell thicknesses are shown in Figure 3.6. In all three samples, the wire was heated to 1015 K at $3.2 \times 10^5$ K/s and then shut off. This temperature is just around the lowest ignition temperature of any particle determined in Figure 3.4. The ignition delays were fairly repeatable, sample 1 (~ 20 μs) and 2 (~50 μs) show lesser variability than sample 3 (~100 μs). Since the heating pulses for the three samples are the same, in the absence of any reaction, the T-jump probe would be cooling down. Despite this, a thermite event occurs, and the event time correlates with oxide shell thickness. *This is the key result which we will interpret.*

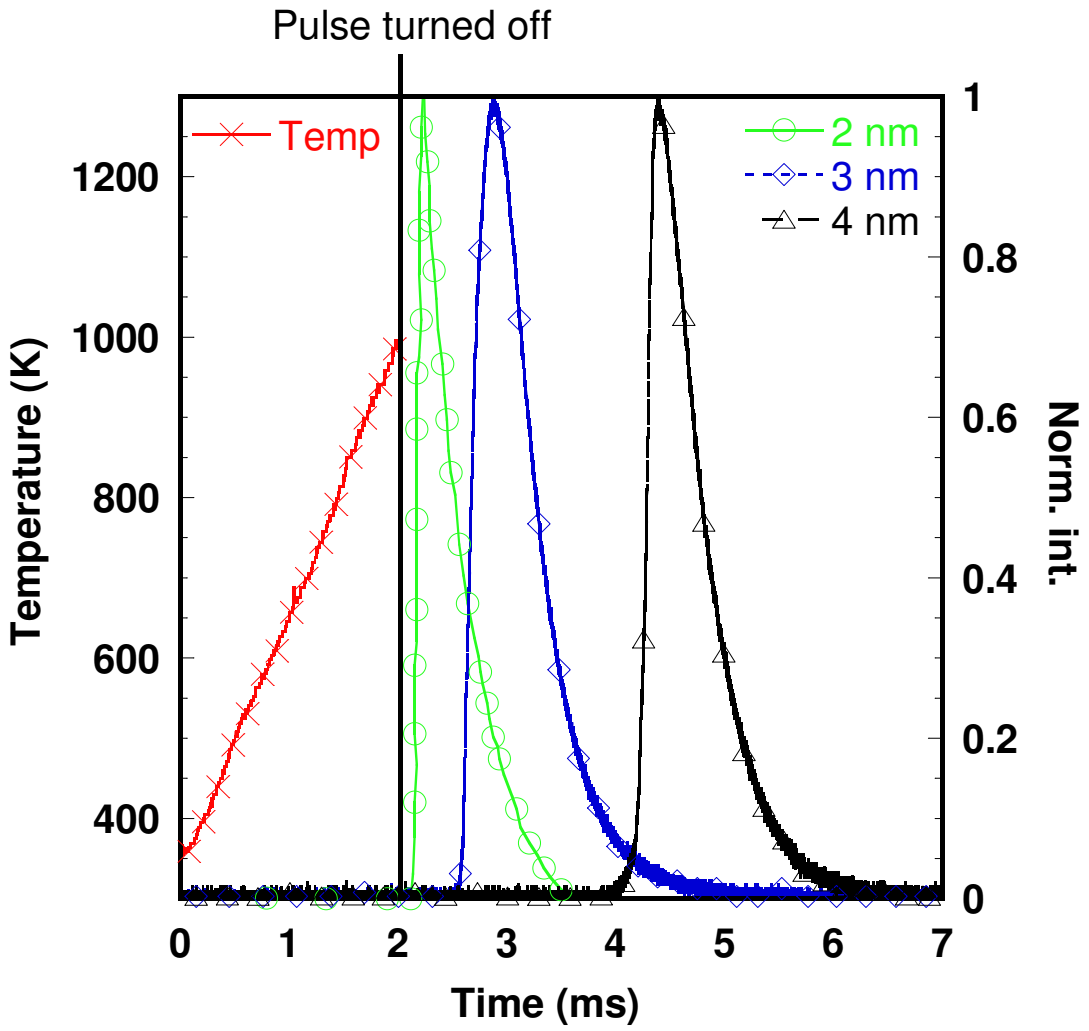


Figure 3.6 Ignition delay as observed for samples 1, 2 and 3. The pulse is shut off at 1015 K.

Finally time resolved time of flight mass spectrometry of Al-CuO nanothermite is also conducted on the samples as a qualitative tool to verify the delay in ignition. A description of the instrument, its operating procedures and verification could be found elsewhere [42]. Figure 3.7 shows time resolved mass spectra taken at 100 μs intervals for sample 1, the 2 nm shell thickness case. Species with strong signals, such as $H_2O^+$ (m/z = 18) and $N_2^+$ (m/z = 28) are background species while $HCHO^+$ (m/z = 30) and

$CO_2^+$ (m/z=44) appears from small amount of copper carbonate formed on the surface of CuO. In this experiment, the heating pulse was turned off around 2.35 ms. Very relevant is that no $Al^+$ (m/z = 27) is seen before 2.35 ms, but appears at ~ 2.4 ms. $Cu^+$ (m/z = 63.0) starts appearing at ~ 2.5 ms, suggesting an ignition delay of ~ 150 µs. This compares very closely to the optical measurement which has better time resolution. Cu is never observed when CuO alone is heated and its appearance in mass spectrometry is analogous to the sharp rise in the PMT signal, as Cu is present only as a product species, and indicates start of the reaction. $O_2^+$ (m/z = 32) appears from the decomposition of CuO, $2CuO \rightarrow Cu_2O + ½ O_2$ and is seen before the pulse is turned off. Cu always appears in the same or after one spectrum of the appearance of Al. Another product species $Al_2O^+$ (m/z=70) appears around the same time as copper. A more detailed description of the mass spectrometric measurements on Al-CuO thermites is available in Zhou et al [43]. Similar results were seen for sample 2 and 3, except that copper seemed to appear even later in the spectrum with increase in shell thickness.

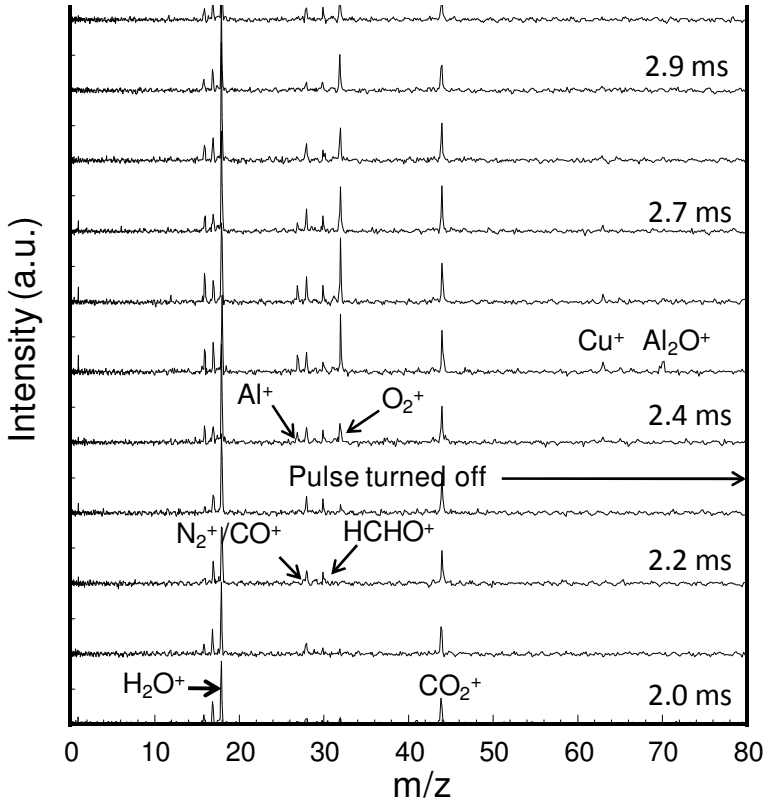


Figure 3.7 Mass spectrometry of sample 1 when the pulse is shut off at 1000 K. Note that there are species emanating from the background ($N_2$) and species that come off due to interaction with hexane ($CO_2$). Al is noticed after the pulse is turned off and so is $Al_2O$. The delay is counted as the time difference between the appearance of a product species (Cu) and turning off of the pulse.

### *3.5 Heat Transfer Model*

From the measured voltage and current data, it is possible to compute the temperature of the platinum wire with respect to time. But we still do not know the temperature of the coated powder on the wire. So a pertinent question to ask is what would be the temperature of the powder in contact with the wire at any given instant

of time. Faster timescales for heat transfer would prevent any thermal gradient between the wire and the powder whereas longer timescales for heat transfer would create a huge thermal gradient along the direction of the powder. So it is necessary to ascertain the temperature of the powder in comparison to the wire.

Before we develop the model it is necessary to estimate the amount of powder coated on the wire as packing density plays a role in heat transfer. In order to estimate the amount of powder put on the wire, we calculate the number of particles, each assumed to be 50 nm in diameter, to be put in order to attain an outer diameter of 175 microns. The diameter of the $i^{th}$ layer of particles, $D_i$ is given by [44]

$$D_i = D_w + d_p [2 + \sqrt{(8/3)} * (i-1)] \quad (3.6.1)$$

where i=1,2,3, … and $d_p$ is the diameter of the particles and $D_w$ the diameter of the wire. The number of particles on the $i^{th}$ layer per unit length is calculated from the equation

$$n_i = \pi * D_i/d_p^2 \quad (3.6.2)$$

Based on the calculations mentioned above, we estimate the amount of powder on the wire to be ~ 300 µg. Using closed packing assumptions as mentioned in Ward et al. [44], the packing density is about 64%. But we still do not know the actual packing density which has to be calculated from the temperature profile of the heated wire. Therefore, the packing density is used as a parameter to fit the measured temperature profile of the wire in the manner described below.

The temperature profile of the powder developed here is based on a model proposed in reference [44]. Since we measure the voltage and current passing through the wire, we can calculate its resistance with time. This enables us to calculate the

amount of electrical energy delivered to the wire over a small amount of time. The energy balance equation for the wire is thus

$$m_w C_w \, dT_w/dt = I^2R - \sigma\varepsilon A_w T_w^4 - (T_w - T_1)/R_1 \qquad (3.6.3)$$

where I is the current flowing through the wire, R is the resistance of the wire, both measured directly from the experiment. $m_w$ and $C_w$ are the mass and specific heat of the platinum wire. The second term on the right in equation 3.6.3 represents the loss of energy due to radiation and the third term denotes the heat conducted to the first layer of the powder. $T_w$ is the wire temperature at any instant, $T_1$ is the temperature of the first layer of the powder and $R_1$ denoted the contact resistance between the wire and the first layer, $\sigma$ is the Stefan Boltzmann ($=5.67 \times 10^{-7}$ $Wm^{-2}K^{-4}$), $\varepsilon$ is the emissivity of platinum and $A_w$ is the surface area of the wire. We neglect any convection term as the heat transfer coefficient is coupled to the temperature which is to be solved for.

For the first layer of powder, the energy equation becomes

$$m_1 C_{powder} \, dT_1/dt = (T_w - T_1)/R_1 - (T_1 - T_2)/R_{2\text{-}n} + \sigma\varepsilon A_w (T_w^4 - T_2^4) \qquad (3.6.4)$$

Here, $m_1$ is the mass of the first layer of the powder, $T_1$ and $T_2$ are the temperature of the first layer of coated powder and $T_2$ is the temperature of the layers 2 to n with $R_{2\text{-}n}$ as the corresponding thermal resistance. The second term thus represents the energy transferred from the first layer to the layers 2 to n. The third term represents the fact that the radiation from the wire is an energy source for the first layer. $C_{powder}$ represents the bulk specific heat of the powder assuming stoichiometric proportion between the fuel and the oxidizer.

The energy equation for the rest of the layers is given by

$$m_{2\text{-}n} C_{powder}\, dT_{2\text{-}n}/dt = (T_1 - T_2)/R_{2\text{-}n} \qquad (3.6.5)$$

For our calculation purposes, $m_w$ is the mass of the platinum wire calculated based on the volume of approximately 5 mm length of wire with 76 µm diameter, density of platinum is taken to be 21450 kg/m$^3$ and $C_w$ is taken to be 133 Jkg$^{-1}$K$^{-1}$. Equations 3.6.3-3.6.5 is discretized explicitly and a time marching calculation is carried out to calculate the temperature of the wire and the first layer of the powder. The calculation for the thermal resistances essential to solve the abovementioned equations is described below.

The thermal resistance $R_1$ is the sum of the thermal resistances $R_{contact}$ arising from the contact points of $n_1$ particles with the platinum wire in parallel. A schematic of the packing on the wire is shown below in Figure 3.7.

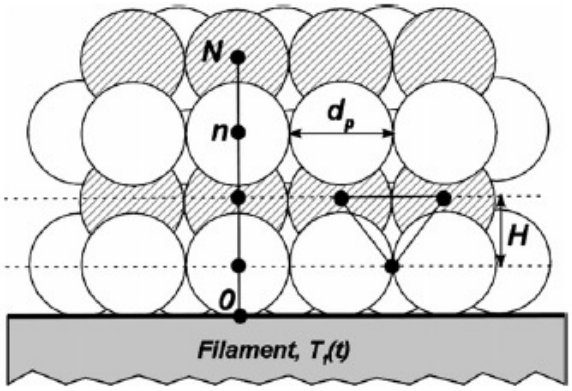


Figure 3.8 Schematic showing the arrangement of the particles on the wire.

Assuming dense packing, the number of contacts of each particle in the first layer is 1, while each successive layer will have 3 contact points for each particle. Therefore,

$$R_1 = R_{contact}/n_1 \qquad (3.6.6)$$

and $$R_i = R_{contact}/(3n_i) \quad \text{for layer } i=2,3,.. \qquad (3.6.7)$$

Based on Equation 3.6.4 it is clear that the heat transfer to the first layer of the powder for a given difference in temperature between the wire and the powder is solely dependent on the contact resistances between the spherical particles of the thermite powder and the wire. The resistance $R_1$ calculated for the first layer of coating from reference [44] is 0.25 K/W.

Figure 3.8 shows the temperature profile of the wire as calculated from the model without any heat transfer to the powder and with heat transfer to the powder. The temperature of the wire calculated assuming perfect packing density of 64% is less than that of the measured temperature. A packing density of 10% slightly overestimates the wire temperature while 20% is right about the wire temperature. Thus, the actual temperature profile measured for the wire matches with the model predictions for packing densities of ~ 20%. Furthermore, the model predicts that the temperature of the first layer of the powder closely follows the temperature profile of the wire, the difference between them being no more than 5 K. Calculations for a packing density was made by assuming that the number of contacts were reduced by the same factor as the packing density and thereby reducing the contact resistance of the first layer.

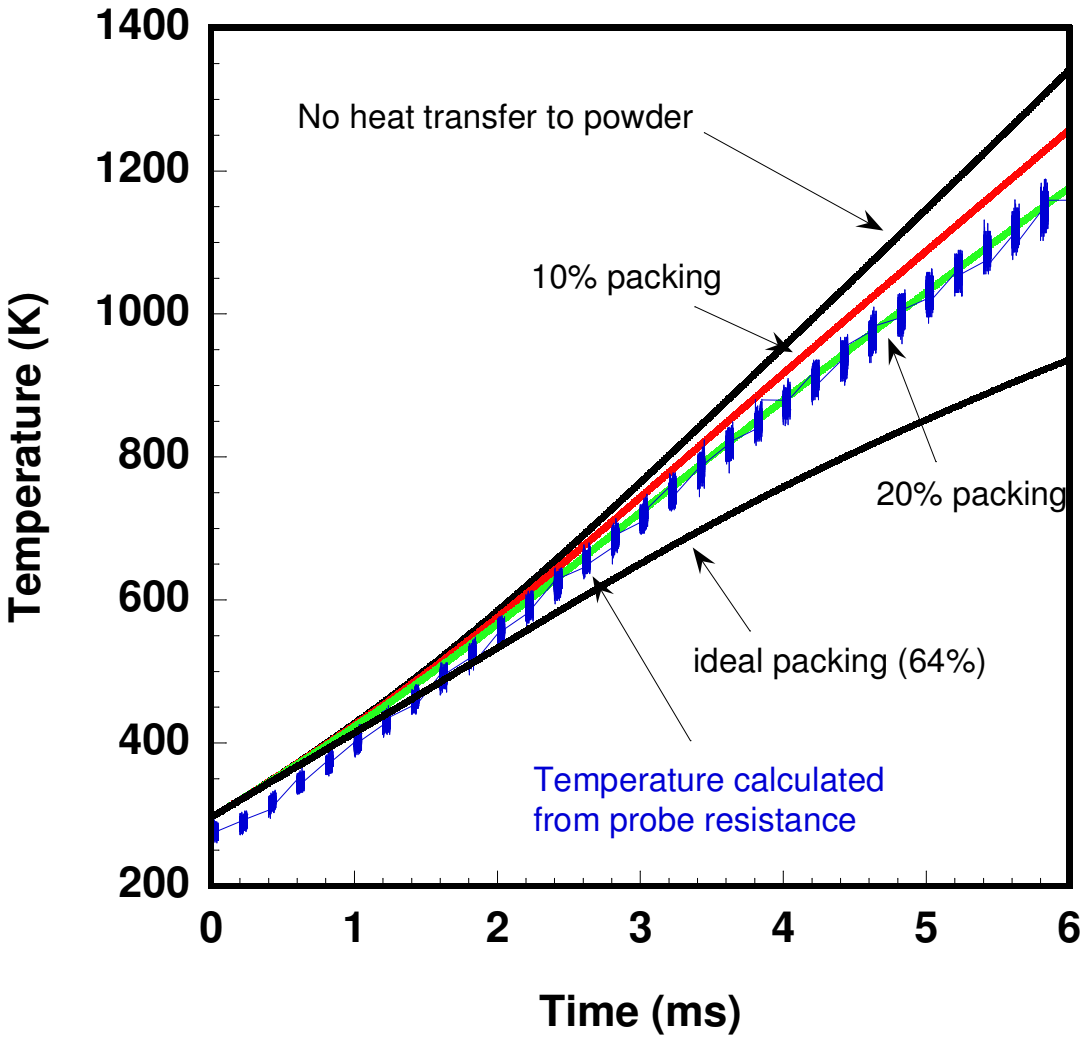


Figure 3.9 Temperature of the wire as calculated using the heat transfer model. Different packing densities are used to match the measured temperature profile of the wire. The coating thickness assumed was 50 microns which was the maximum thickness observed in SEM.

### *3.6 Discussion*

The independence of ignition temperature on heating rate for any given shell thickness is possibly a first suggestion against the melt dispersion mechanism, as it is

expected be very sensitive to heating rate. However, the range of heating rates is fairly small in our case, which is restricted by the power supply. The change in ignition temperature in Figure 3.3 with oxide thickness could be explained as due to a longer path to diffusion through the oxide shell, rather than an increase in temperature. This point is most reinforced by the key observation in this work (Figure 3.5), where ignition occurs after the wire is turned off and thus energy input to the system ceases. Furthermore, the thicker the oxide shell, the greater the ignition delay - again consistent with a diffusion mechanism. According to the melt dispersion mechanism, reaction would occur at the melting point of aluminum owing to the maximum mismatch in thermal expansion coefficient between the molten aluminum core and the solid oxide shell.

Results from our heat transfer model showed that the powder temperature is <5 K from the wire temperature. Also, once the pulse is shut off, the heat loss from the wire due to convection and radiation is minimal, which over the relevant time of the experiment decreases no more than ~ 50 K. This would indicate the ignition temperature of the powder exceeds the melting point of aluminum (~933 K) and contrary to what is expected according to the melt dispersion mechanism. The characteristic heat transfer time across a nanoparticle is on the order of a few nanoseconds, so that melting should occur essentially instantaneously once the melting point is exceeded. This would cause a huge buildup in internal pressure, and hence explode violently, in time scales on the order of ~ ns. However, we see no evidence of reactions at such time scales, rather we see delay times of ~100's of microseconds.

The melt dispersion mechanism is expected to happen at very high heating rates of $10^6$-$10^8$ K/s [45]. This was suggested on a phenomenological basis from the rise time observed in pressure traces in burn tube experiments [18]. However, in those experiments, the powder was set off by an electrical igniter. The external heating rate is thus unknown and hence, the above mentioned rate is clearly the "intrinsic" heating rate once the powder has ignited. The adiabatic flame temperature of Al-CuO mixture is ~2840 K and the ignition temperature seen in this study is ~1020 K. The rise time (time for the optical signal to go from 0 to 1 in Fig. 3.5) observed in the optical signal is ~ 100 µs. This would suggest an intrinsic heating rate of ~ $1.8x10^7$ K/s, which is within the range of the melt dispersion mechanism. As a result, we would assume that the "intrinsic" heating rate of the powder is sufficient to observe the melt dispersion mechanism if it were to happen.

Table 3.3 Ignition delay and effective diffusion coefficient with oxide shell thickness.

| Oxide shell thickness, L (nm) | $t_{delay}$ (µs) | $D_{eff}$ ($cm^2/s$) |
|---|---|---|
| 2 | 100 | 4.0E-10 |
| 3 | 500 | 1.8E-10 |
| 4 | 2000 | 8.0E-11 |

An order of magnitude estimate of the effective diffusion coefficient (= $L^2/t_{delay}$) is presented in Table 3.2 for the tested samples. The delay times are an average of 2 experiments. The characteristic diffusion length (=L) is assumed to be the shell thickness. These diffusion coefficients agree reasonably well with other results [11].

The appearance of $Cu^+$ signal in mass spectrometry follows the same trend that we see in our optical experiments. We use Cu as evidence of reaction since it does not appear when we heat pure CuO, but rather only when the aluminum is present. Cu gas is a major reaction product of stoichiometric Al/CuO under vacuum, and so its signature is good proof that the reaction is occurring. The appearance of copper later in the spectrum for samples 2 and 3 (relative to sample 1) indicates a delay in the initiation of those reactions. This qualitatively supports the statement that the reaction is diffusion controlled. In addition to that, there is no evidence of aluminum clusters $Al_2$, $Al_3$, $Al_4$ etc. as proposed by the melt dispersion mechanism. Smaller clusters are usually unstable in nature and may avoid detection. However, the lack of identification of any of these clusters point towards the absence of evidence for melt dispersion mechanism.

Based on the observed ignition temperature, the aluminum core would be molten. Although the purpose of this work is not to determine the diffusing species, it is the aluminum ions from the molten core which are more likely to diffuse because of their smaller size relative to oxygen ions. Evidence of the dominance of the diffusion of aluminum has been observed in other studies too. Prior studies in our group [11] have shown the formation of hollow particles during aluminum oxidation where the molten aluminum in the core has leaked out and reacted. Similar hollow particle formation has also been reported by Nakamura et al. [46]. Henz et al. [47] has also recently showed that intrinsic electric fields within the nanoparticle promote the movement of aluminum ions through the oxide shell, which significantly enhance the initial transport over Fickian diffusion.

Once the reaction starts, an increase in temperature will cause an enhancement in the diffusion rate for all diffusing species. Although, based on references [11] and [46], we would expect all the aluminum in the core to leak out faster. However, we do not have direct evidence of this and would avoid making such conclusions.

Figure 3.10 summarizes the ignition delay observed for the various cases tested. Ignition delay increases with increase in shell thickness, with 4 nm shell showing the longest delay. The mass spectrometric data compares well qualitatively with the optical data and shows the same trend as identified by the appearance of the Cu signal. These observations point out an initiation mechanism governed by diffusion across the oxide shell.

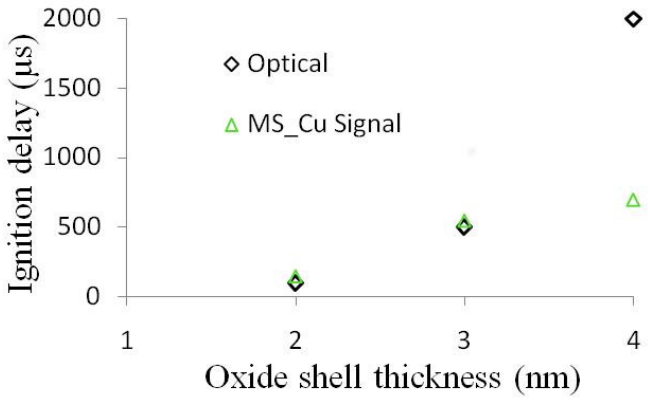


Figure 3.10 Comparison of ignition delay as observed with the MS and PMT. Qualitatively they follow the same trend with sample 2 and 3 showing higher ignition delay.

## *3.7 Conclusions*

Experiments were conducted at high heating rates to investigate the ignition mechanism of nano-thermites. Aluminum nanoparticles were prepared with varying

oxide shell thicknesses, and were mixed with CuO to investigate the ignition behavior at high heating rates of ~$10^5$ K/s. We find the ignition temperature is well above the melting point of aluminum, and ignition was not observed below 1015 K. Furthermore *an ignition delay consistent with a diffusion limited reaction is observed.* The delay increased with increase in shell thickness of aluminum particles in the samples, and from this effective diffusion coefficients were extracted. Fast time-of-flight mass spectrometry shows that the appearance of copper, which is a product species, is progressively delayed in the mass spectra with increase in the shell thickness and agrees with the order of ignition delay observed. Based on our data, we would conclude that ignition under the heating rates investigated has a *diffusion governed mechanism.*

# Chapter 4: Nanothermite Reactions: Is Gas-phase Oxygen from the Oxygen Carrier Necessary?

Metal-oxidizer mixtures of nanoparticles have recently generated considerable interest in the combustion community due to their enhanced reactivity and high energy density on a mass/volumetric basis as compared to traditional organic compounds. Such mixtures are often called nanothermites or metastable interstitial/intermolecular composites (MICs). By using nanoparticles, the fuel and oxidizer can be finely intermixed, thus improving the interfacial contact and greatly reducing the characteristic mass diffusion length between the reactants.

While fuels like boron [48] and silicon [49] have been explored, nano-aluminum (n-Al) is predominantly the fuel of choice due to a combination of its high energy density, reactivity, low cost, and nontoxic nature. A variety of oxidizers have been studied, and the choice often depends on the particular application. Copper oxide (CuO) [17, 50], iron oxide ($Fe_2O_3$) [50], molybdenum oxide ($MoO_3$) [18, 26, 51-54], tungsten oxide ($WO_3$) [52] and bismuth oxide ($Bi_2O_3$) [52, 55] are the commonly used oxidizers in nanothermites.

Nano-aluminum particles typically have a thin (~ 2-5 nm in thickness) amorphous aluminum oxide shell surrounding the elemental core of aluminum, protecting the particle from further oxidation in air. The aluminum in the core has been shown to be under compressive stress while the shell is under tensile stress [11]. These particles are typically aggregates of spherical primary particles, although recent work has shown the formation of single domain aluminum crystals [56]. For

nanoparticles, the oxide shell can represent a significant portion of the particle mass. Oxidizer particles used in prior studies, on the other hand, display various morphologies. They have been used in the form of platelets [52, 54], crystalline sheets [52], spheres [50, 55] and nanorods [52, 55, 57].

An interesting and unresolved question in the study of nanothermites is the way they ignite/react depending on the heating rates involved. At lower heating rates (~ 1-20 K/min), Trunov [13] has shown the oxide shell to undergo phase transformations making it permeable to the mass transport of aluminum and oxygen across the shell. Since reaction was observed to occur below the melting temperature of bulk aluminum (933 K), the authors argued that reaction must be caused due to the inward diffusion of oxygen ions as aluminum is fairly immobile in the solid state. At faster heating rates (~ $10^3$ K/s), Rai [11] showed the formation of hollow aluminum particles after oxidation. He argued that the aluminum in the core must have leaked out by diffusion due to concentration and/or pressure gradient across the shell. Similar experimental evidence has also been demonstrated by Nakamura [46]. Pursuing this idea, we have shown in a previous work [58] that diffusion of reactive species is controlling even at heating rates on the order of $10^5$ K/s. Based on the observed ignition delay, an effective diffusion rate of ~$10^{-10}$ $cm^2/s$ was calculated. In another recent study by our group, Sullivan and Zachariah [23] used a specially-designed heating holder to heat n-Al at $10^6$ K/s inside a scanning electron microscope. In this particular study, a significant heating pulse (300-1473 K at $10^6$ K/s, and then held at 1473 K for 10 ms) was necessary before shell breakdown occurred, and outwards migration of Al could visually be identified. A smaller heating pulse,

although above the melting temperature of Al, induced no changes within the very fast heating and cooling timescale of this experimental technique. Using Al-$WO^3$ nanothermite mixture, the authors suggested a condensed phase initiation/reaction. At even higher heating rates (~ $10^7$-$10^8$ K/s) Levitas et al. [10] proposed the "Melt Dispersion Mechanism (MDM)" in which the aluminum core melts and exerts mechanical stress on the solid oxide shell. This causes spallation of the shell, and is predicted to happen at or near the melting temperature of aluminum, viz. 933 K. The violent rupture of the shell causes tensile stress on the molten Al core, thus unloading small molten clusters of aluminum at high velocities. The reaction rate in this mechanism is inherently not rate-limited by the diffusion of oxidizer/fuel through the shell. In a separate study using time resolved mass spectrometry of rapidly heated (~$10^5$ K/s) nanothermites [43], no evidence of aluminum clusters were found but only elemental aluminum was detected. Based on our previous work and the lack of aluminum clusters being detected, our current speculation is that aluminum migrates through its shell via a diffusion mechanism.

The correlation between oxygen release and nanothermite reaction have been suggested by Schoenitz [53]. They conducted thermal analysis at low heating rates on Al-$MoO_3$ nanothermites and tentatively concluded that the appearance of the first exothermic peak at ~ 470 K is indicative of the decomposition of $MoO_3$ into $MoO_2$ and oxygen (O). The authors commented that the in-situ oxygen produced due to decomposition of the oxidizer could readily escape if the nanothermite mixture is prepared from the individual components in powder form. Similar suggestions of the possible decomposition of the oxidizer have been put forth to explain the kinetic

behavior for Al-CuO nanothermite reactions observed under low heating rates by Umbrajkar et al. [17]. Direct experimental evidence of oxygen release from the oxidizer and its correlation to the ignition of nanothermites was first shown in our prior publication [43] using a T-jump time of flight mass spectrometer (T-jump TOFMS). Details of the operation of this instrument are available in a previous publication [42]. In short, the nanothermites were ignited on a platinum wire by heating them by an electrical pulse (~$10^5$ K/s) and the species produced during the reaction were sampled every 100 µs. With a high heating rate (~5 x $10^5$ K/s) we detected the release of molecular oxygen ($O_2$) from CuO and $Fe_2O_3$ in the reaction of Al-CuO and Al-$Fe_2O_3$ thermites. The liberated $O_2$ was one of the first species to be detected temporally thus suggesting that $O_2$ release played a critical role in the ignition mechanism. This also suggests the role of gas phase oxygen towards ignition of Al-CuO and Al-$Fe_2O_3$ nanothermites.

Bazyn et al. [21] studied the ignition temperature and burn time of Al-$MoO_3$ and Al-$Fe_2O_3$ at high heating rates (~$10^6$ K/s) using a shock tube. They found evidence for ignition of both materials at 1400 K and 1800 K respectively. It's important to note that these temperatures are significantly higher than the melting temperature of aluminum. The findings of ignition temperatures well above the melting temperature of aluminum, and the fact that ignition temperature depends on oxidizer type, indicate that the oxidizer must play some role in the ignition mechanism at high heating rates. The thermal response of a metal oxide to heating depends on the particular oxidizer; some materials can melt, others decompose into sub-oxides prior to melting, some can even sublimate. It has recently been shown [23] by in-situ high heating rate

electron microscopy ($10^6$ K/s) that Al-$WO_3$ nanothermites can react via condensed phase reactions. In a separate study [59] the reaction product particles were also found to be larger than the original reactant particles. The changes in morphology for only those fuel and oxidizers particles touching each other, leads one to consider that reactive sintering may be an important driving mechanism. In the context of this paper, it is important to remember that the reactive sintering mechanism [59] can serve as an alternative mode to the gas-solid reactions. This opens up the question regarding the importance of gas phase oxygen on nanothermite initiation, and is the focus of the present article. We will chose a wide range of oxidizers which release oxygen at a widely different range of temperature, and measure the ignition temperature for nanothermites to verify if gas phase oxygen is essential for the initiation of nanothermite reactions.

## *4.1 Experiment*

### 4.1.1 Sample Preparation

Commercially available n-Al (Argonide Corp.) was used for all the experiments. The nominal size of the particles as specified by the supplier is 50 nm, and was determined to be 70% active using thermogravimetric (TGA) analysis, indicating an oxide shell of approximately 2 nm in thickness. The various materials and the relative size of the primary particles as specified by the manufacturers are given below in Table 4.1.

Table 4.1 Oxidizers, source and primary particle size

| Material | Supplier | Particle size (nm) |
|---|---|---|
| ALEX | Argonide Corp. | 50 |
| Copper oxide (CuO) | Sigma-Aldrich | < 50 |
| Iron oxide ($Fe_2O_3$) | Sigma-Aldrich | < 50 |
| Tungsten oxide ($WO_3$) | Sigma-Aldrich | < 50 |
| Bismuth oxide ($Bi_2O_3$) | Sigma-Aldrich | < 50 |
| Silver iodate ($AgIO_3$) | NSW-China Lake | ~ 236 |
| Potassium Perchlorate ($KClO_4$) | Aerosol synthesized in our lab | ~ 300 |
| Tin (IV) oxide ($SnO_2$) | Sigma-Aldrich | < 50 |
| Cobalt(II, III) oxide ($Co_3O_4$) | Sigma-Aldrich | < 50 |
| Molybdenum oxide ($MoO_3$) | US Research Nanomaterials | 13-80 |
| Antimony (III) oxide ($Sb_2O_3$) | US Research Nanomaterials | 80-200 |

For the gas release experiments, approximately 10-15 mg of the bare oxidizers were dispersed in hexane, sonicated for 10 minutes and then heated as described in the experimental approach section below. Additionally, appropriate amounts of n-Al and various oxidizers listed in Table 1 are weighed to make stoichiometric sample, and then dispersed together in hexane. The mixture is then sonicated for 25 min before being subjected to ignition tests.

### 4.1.2 Experimental Approach

In order to achieve the high heating rates for T-jump TOFMS experiments, a thin platinum wire (length ~ 12 mm, diameter ~ 76 μm) is joule-heated by a tunable

voltage pulse generated by a custom built power source. The transient current passing through the circuit is measured by a current probe. A small portion of the central region of the wire (~ 3-4 mm) is coated with the samples by pipetting a dispersion of the samples in hexane onto the wire, then allowing the hexane to evaporate. The amount of material coating the wire is estimated to be around 300 µg. From the recorded voltage and current data, the temperature of the wire at the point of ignition can be calculated from the resistivity of the wire using the well-known Callender-Van Dusen equation [41]. Since the application of this equation is limited to 933 K, the resistance of the platinum wire was calibrated against a NIST calibrated blackbody source (Mikron M350) based on two color pyrometry centered about 970 nm and 1550 nm as described in the previous chapter. An extrapolation of the calibration based on Sakuma Hattori equation [60] enables one to extend the calibration up to ~1700 K. The maximum uncertainty associated with the determination of temperature is approximately ± 50 K. Heating rate is defined as the ratio of the difference in maximum temperature and initial temperature to the pulse duration and is assumed to be linear. The optical emission is monitored using a photomultiplier tube (PMT), and the ignition temperature is taken as the wire temperature corresponding to the onset of optical emission with appropriate background correction from the heated bare wire. For each test, a new wire is used since reacted material may adhere to the wire and change the electrical properties, thus presenting uncertainty in the temperature calculation.

For the gas release experiments, the bare oxidizers are coated on the platinum wire and heated in the T-jump TOF mass spectrometer. These experiments are

conducted to measure the temperature of $O_2$ release from the individual oxidizers under heating. To measure the ignition temperature, a separate set of experiments are carried out by coating the platinum wire with the prepared nanothermite samples. The T-jump TOFMS system [42, 43] was modified by adding a photomultiplier tube (PMT), thus allowing for simultaneous collection of the mass spectra and the optical emission. This allows for a direct comparison between the optical emission, commonly used as a measurement of ignition, and the time-resolved species evolved during the reaction.

### *4.2 Thermochemical behavior of oxidizers on heating*

Before discussing the thermite results, we first consider what happens when the individual oxidizers are heated. Certain oxidizers melt directly to the liquid phase, whereas other oxidizers decompose first to form a sub-oxide, which then melts and decomposes upon further heating. Some of the thermodynamically predicted phase changes or decompositions are calculated using the NASA-CEA software [61]. These calculations were performed at constant temperature and pressure. The pressure is fixed at $5x10^{-9}$ atmosphere, which is characteristic of the pressure existing in the mass spectrometer chamber. Starting at around 600 K, successive calculations were performed in increments of 50 K in temperature until decomposition is observed. Phase change/decomposition data from other sources are listed for oxides which are not included in the species library of the CEA software. A summary of the behavior of the various oxides are shown below in Table 4.2.

Table 4. 2 Summary of the behavior of the oxidizers under heating. The parentheses indicate the phase(s) of the product(s).

| Oxidizer | Temperature (K) | Event | Products | Temperature (K) | Event | Main Product (s) |
|---|---|---|---|---|---|---|
| CuO | ~800[a] | Decomposes | $Cu_2O$ (s), $O_2$ (g) | 1100[a] | Decomposes | Cu (s), $O_2$ (g) |
| $Fe_2O_3$ | ~1100[a] | Decomposes | $Fe_3O_4$ (s), $O_2$ (g) | 1500[a] | Decomposes | Fe (s), $O_2$ (g) |
| $WO_3$ | 1200[a] | Decomposes | $(WO_2)_2$ (g) $(WO_2)_3$ (g) etc. | - | - | - |
| $SnO_2$ | 1175[a] | Decomposes | SnO (g), $O_2$ (g) | - | - | - |
| $AgIO_3$ | 678[b] | Decomposes | AgI (s), $O_2$ (g) | 831[c] | Melts | AgI (l) |
| $Co_3O_4$ | 1173[c] | Decomposes | CoO (s), $O_2$ (g) | 2103[c] | Melts | CoO (l) |
| $KClO_4$ | 865[d] | Decomposes | KCl (s)[d] $O_2$ (g)[d] | - | - | - |
| $MoO_3$ | 1075[c] | Melts | $MoO_3$ (l) | 1428[c] | Boils | $MoO_3$ (g) |
| $Bi_2O_3$ | 1098[e] | Melts | $Bi_2O_3$ (l) | - | - | - |
| $Sb_2O_3$ | 929[c,e] | Melts | $Sb_2O_3$ (l) | 1703[c], 1823[e] | Vaporize | $Sb_2O_3$ (g) |

[a] Constant T,P calculations in CEA [61]
[b] Reference [62]
[c] Reference [63]
[d] Reference [64]
[e] Reference [65]

It is clear from Table 4.2 that under the conditions of our experiments, CuO and $Fe_2O_3$ would decompose into respective sub-oxides $Cu_2O$ (s) and $Fe_3O_4$ (s), releasing oxygen, before decomposing to the zero-valent metal at higher temperatures. $WO_3$ and $SnO_2$ on the other hand directly decompose into products which are all in the gas phase. The behavior of $SnO_2$ is somewhat similar to that of CuO and $Fe_2O_3$ as it decomposes into a sub-oxide, SnO (g) and $O_2$ (g).

$AgIO_3$ on heating decomposes into AgI (s) and $O_2$ (g) [62]. AgI (s) then undergoes melting at 831 K. Cobalt (II, III) oxide ($Co_3O_4$) decomposes around 1173 K into CoO (s) and $O_2$ (g). The decomposition product CoO (s) is comparatively stable and does not melt until 2103 K [63]. $KClO_4$ is known to decompose into its potassium chloride (KCl) and $O_2$ (g) at 865 K [64]. Our results come very close at 875 K. $MoO_3$ melts at 1075 K to $MoO_3$ (l) and boils at 1428 K [63].

Alternatively, oxidizers such as $Bi_2O_3$ and $Sb_2O_3$ melt first. Not much is known about the behavior of $Bi_2O_3$ above its melting point at 1098 K [65]. On the other hand, antimony (III) oxide ($Sb_2O_3$) melts around 929 K [63, 65], and then vaporizes without decomposition producing $Sb_2O_3$ (g) at 1703 K according to reference [63] and at 1823 K according to reference [65].

Before proceeding to discuss the results, it is worth mentioning that melting temperatures are generally not highly sensitive to the surrounding atmosphere or pressure. On the other hand, the traditional definition of decomposition temperature is

somewhat confusing under the experimental conditions used in this study. The decomposition temperature of the oxidizer into a gas, based on an equilibrium calculation, is computed under a constraint of the equilibrium mole fraction of the gas phase product of the solid. Thus increasing the total system pressure also increases the decomposition temperature, so that the sum of the partial pressures of the decomposition products to sum to the total pressure, such that at equilibrium the leaving (from solid) and arrival rate (to solid) of species are equivalent. However the escape probability of a decomposing molecule on a surface is independent of the total pressure and only depends on temperature. As a result when one considers the initial decomposition one is operating far from equilibrium, the initial decomposition is independent of the total pressure. Thus one should consider the equilibrium calculations as a relative measure of products formed, and the temperature of their transformations.

## *4.3 Results*

### 4.3.1 Oxygen Release

Molecular oxygen is observed to be released from a majority of the oxidizers under heating. Figure 4.1 depicts a representative temporal plot for $O_2$ release from CuO during a temperature ramp of $5x10^5$ K/s.

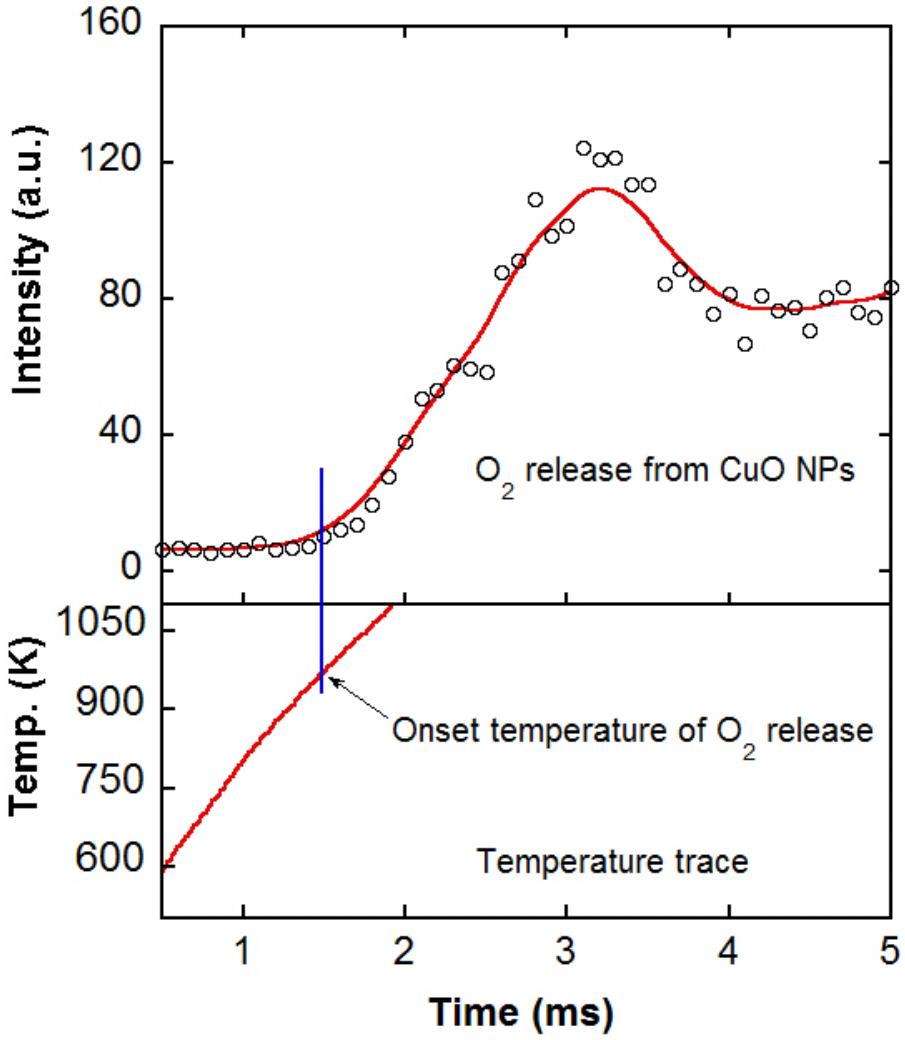


Figure 4.1 Representative plot showing the temporal release of molecular oxygen from CuO when heated at $5x10^5$ K/s.

The results show that oxygen release is first observed at a temperature of ~975 K. Similar experiments on other neat metal oxides enable us to determine the primary evolving gas phase species and there threshold decomposition temperature. Table 3 lists the oxygen release temperature for various oxidizers along with the major gas species detected.

Table 4. 3 Gas release temperature and primary gas species detected during heating of various oxidizers (average of two experiments). Blank spaces indicates that no vapor phase species was observed for neat oxide heating.

| Oxidizer | Gas release temperature (K) (± 50 K) | Primary gas species detected |
|---|---|---|
| CuO | 975 | $O_2$ |
| $Fe_2O_3$ | 1340 | $O_2$ |
| $WO_3$ | - | - |
| $SnO_2$ | 1675 | $O_2$ |
| $AgIO_3$ | 892 | $O_2$ |
| $Co_3O_4$ | 1025 | $O_2$ |
| $KClO_4$ | 875 | $O_2$ |
| $MoO_3$ | - | - |
| $Bi_2O_3$ | 1615 | $O_2$, Bi, $Bi^+$ |
| $Sb_2O_3$ | - | - |

The data presented in Table 3 above is an average of 2 experiments. Most of the oxidizers release $O_2$ (except for $Bi_2O_3$ which, in addition to $O_2$, generates Bi gas) while some oxidizers do not. CuO, $Fe_2O_3$, $Bi_2O_3$, $KClO_4$, $AgIO_3$, $SnO_2$ and $Co_3O_4$ release oxygen on decomposition which has been detected by the mass spectrometer. $AgIO_3$ has the lowest oxygen release temperature at ~ 900 K, while $SnO_2$ exhibits the highest temperature of 1675 K. No gaseous species were detected for $MoO_3$ and $Sb_2O_3$ when the neat oxidizers are heated.

The oxygen release temperature for an oxidizer is unique and specific. This presents us with the opportunity to use ignition data for various nanothermite mixtures to gain an understanding of the effect of gas phase oxygen on the ignition/reaction of the corresponding nanothermite. If gas phase oxygen is essential for ignition initiation/combustion, then one would expect ignition temperature, to closely track the oxygen release temperature.

### 4.3.2 Ignition Experiments

The temporal oxygen and aluminum signal as detected by TOFMS during the reaction of Al-CuO nanothermite is shown in Figure 4.2 (top) while the optical emission is shown below. Ignition as identified by broadband optical emission occurs ~1040 K, and is close to the temperature at which oxygen is released from the bare oxidizer (975 K), within the experimental uncertainty of ± 50 K for both measurements. The optical signal is also observed to be correlated with the appearance of both the aluminum and oxygen species in this case. This is in agreement with what has been reported before in reference [43]. This raises an important question as to whether the release of oxygen gas is an essential precondition to ignition. To explore this hypothesis, we compare the release of oxygen from neat oxidizers, in the thermite mixture, and the corresponding ignition temperature when used as an oxidizer for aluminum.

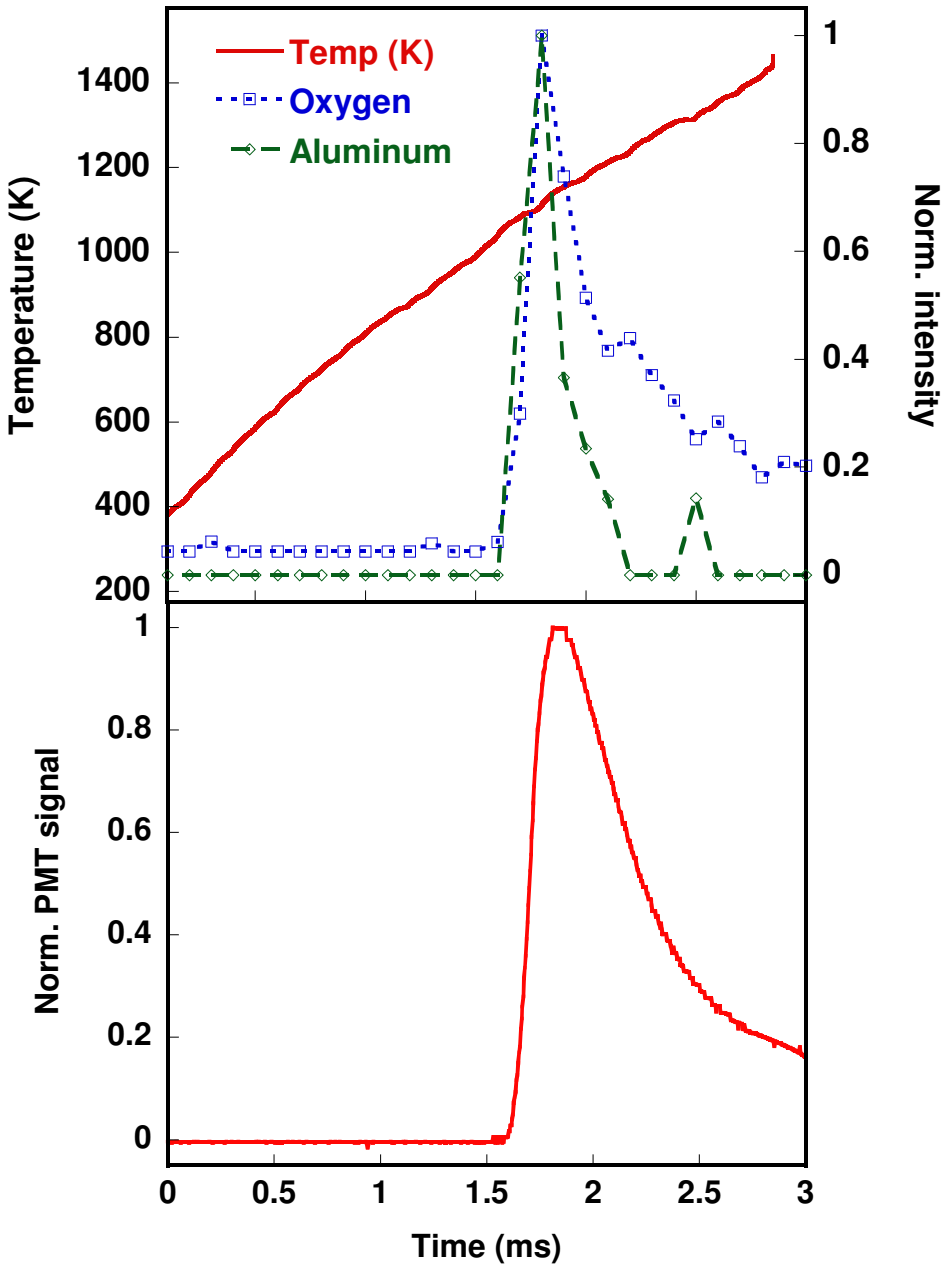


Figure 4.2 (top) Temporal profile of aluminum and oxygen species during the reaction of Al-CuO nanothermite mixture of stoichiometric composition. (bottom) Optical emission showing ignition as recorded by a PMT simultaneously.

The results of this comparison is shown in Table 4.4, which presents the observed ignition temperature, the temperature at which oxygen is detected during the nanothermite reactions, and the temperature where $O_2$ release from the neat oxidizer is seen.

Table 4.4 Ignition temperature of various n-Al based nanothermites listed in terms of the oxidizer. The oxygen release temperature from the nanothermite reactions and the bare oxidizer as detected by TOFMS is also tabulated.

| Nanothermite (Al +oxidizer) | Ignition temperature (K) (± 50 K) | $O_2$ release temperature in thermite (K) (± 50 K) | $O_2$ release from bare oxidizer (K) (± 50 K) |
|---|---|---|---|
| $AgIO_3$ | 890 | 880 | 890 |
| $KClO_4$ | 905 | 905 | 875 |
| CuO | 1040 | 1050 | 975 |
| $Fe_2O_3$ | 1410 | 1400 | 1340 |
| $Co_3O_4$ | 1370 | 1020 | 1030 |
| $Bi_2O_3$ | 850 | 930 | 1620 |
| $Sb_2O_3$ | 950 | - | - |
| $MoO_3$ | 850 | - | - |
| $WO_3$ | 1030 | - | - |
| $SnO_2$ | 1050 | MS shutdown | 1680 |

We now analyze the ignition temperature data in the context of our original motivation to determine if gas phase oxygen is essential for ignition. Figure 4.3 plots the observed oxygen release temperature from the neat oxide against the observed ignition temperature.

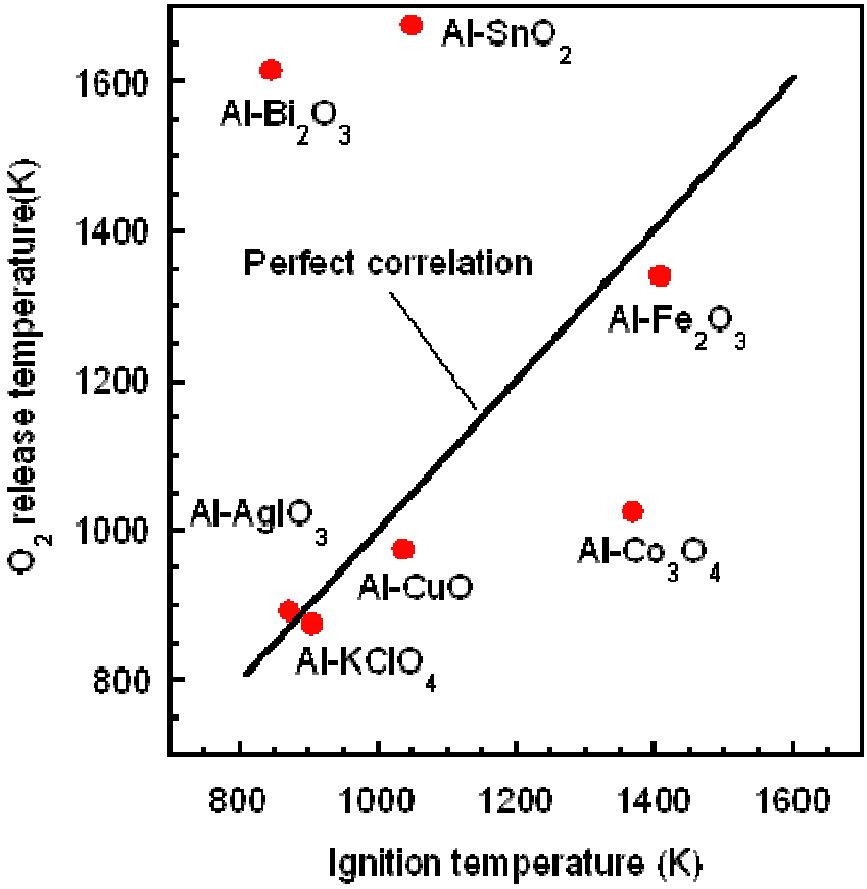


Figure 4.3 Oxygen release temperature from neat oxide vs. ignition temperature for various n-Al based nanothermites. The straight line indicates a perfect correlation. Nanothermites where the oxidizers do not release any oxygen are not shown.

It is evident from Figure 4.3 above that there exists a good correlation between oxygen release from the oxidizer and ignition for CuO, $Fe_2O_3$, $AgIO_3$, $KClO_4$ nanothermites as they lie close to the diagonal line. However, $Bi_2O_3$ and $SnO_2$ nanothermites ignite (850 K and 1050 K respectively) much below their oxygen release temperatures (1620 and 1680 K). $Co_3O_4$ nanothermite on the other hand, is seen to ignite after oxygen release. Furthermore, nanothermite samples made from $WO_3$, $MoO_3$ and $Sb_2O_3$ oxidizers ignite even though we observe no oxygen release at all. These results suggest that at least in part some of these systems may rely on a heterogeneous-condensed state reaction process. Most striking is the Al-$Bi_2O_3$ case where oxygen is released at 930 K during the nanothermite reaction, almost 700 K lower than the temperature when $Bi_2O_3$ releases oxygen. For several other nanothermites, we find that the oxygen release temperature from the nanothermites and the bare oxidizer are the same with experimental uncertainty. It may also be noted that the Al-$Bi_2O_3$ and Al-$MoO_3$ are also the nanothermites which react slightly below the melting point of aluminum. Due to the generation of intense ion peaks associated with ignition, the MS was shut down during the Al-$SnO_2$ reaction. Consequently, only the ignition data is available for this reaction.

## *4.4 Discussion*

The oxygen release and ignition temperature data reported in this study indicate clearly that gas phase oxygen is not an essential species required for ignition. However, as seen from Figure 4.3, there are some nanothermites whose ignition correlates very well with the release of gas phase oxygen from the oxidizer.

Recently, we reported on a study in which Al-CuO nanothermites were subjected to heating in a transmission electron microscope (TEM). Figure 4(a) and (b), taken from reference [59] shows images before and after the nanothermite was subjected to a heating pulse of 300-1473 K @ $10^6$ K/s, and held at 1473 K for 10 ms. The broader implications of these results are discussed in a separate article [59]. In brief, the occurrence of morphological structures larger than the particle sizes we started with suggests a reactive sintering mechanism as is confirmed by the formation of $Al_2O_3$ by the energy dispersive spectroscopy (EDS) shown in Figure 4(b). We have also shown that these large scale structures were predominantly formed just before/during the initiation of the reaction. The timescales of such formation is at least 1-2 orders of magnitude smaller than the reaction timescales, suggesting that reactive sintering mechanism can be an alternative mode of initiation as opposed to the heterogeneous gas phase reaction hypothesized in another previous publication by our group [43]. In the context of this study, under the extremely low pressure in the TEM chamber during the experiment, any gas species (for example, oxygen) produced from CuO would leave the site of the reaction immediately. We have thus shown evidence of a nanothermite reaction in the absence of any gas phase oxygen via the reactive sintering mechanism. This is significant as Al-CuO is a nanothermite where apparently the release of oxygen from CuO correlates well with ignition as shown in Figure 4.3.

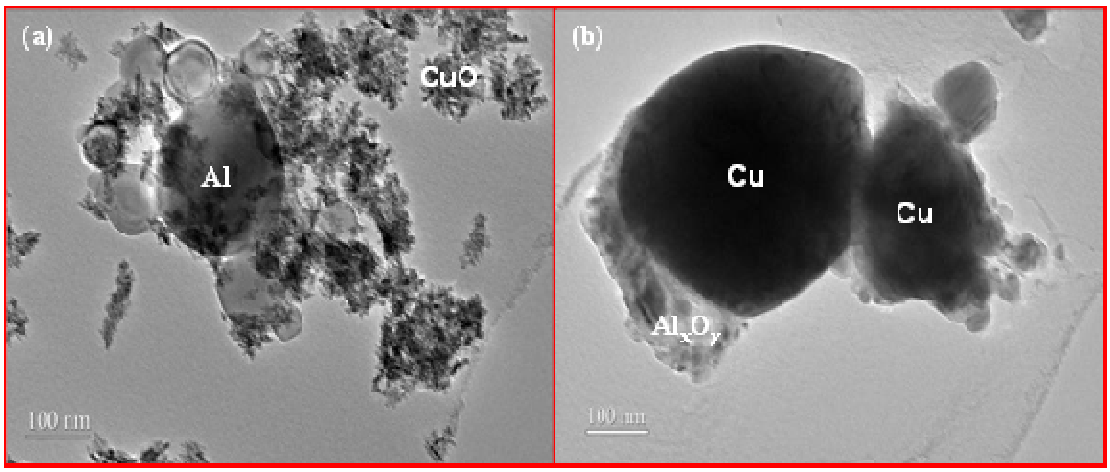


Figure 4.4 TEM images showing the morphology of Al-CuO nanothermites (a) before and (b) after reaction, imaged in the same location. The heating pulse provided is 300-1473 K at $10^6$ K/s, followed by a 10 ms hold at the maximum temperature. The elemental mapping is done in a separate microscope [59].

Reactive sintering has also been shown to be the initiation mechanism for Al-$Fe_2O_3$, another nanothermite whose ignition correlates well with the release of oxygen from $Fe_2O_3$. Consequently, it is highly possible that the nanothermites, whose ignition has been found to correlate with the release of gas phase oxygen from the oxidizer, actually initiate via reactive sintering which is a condensed state process. The simultaneity observed between oxygen release and ignition of these nanothermites may just be pure coincidence.

Let us now discuss some of the nanothermites whose oxidizers do not decompose into any gas products upon heating ($WO_3$, $MoO_3$ and $Sb_2O_3$). From the very fact that they ignite, we argue that ignition occurs via a condensed state reaction. As it turns out, a reactive sintering mechanism has also been shown to occur in Al-$WO_3$

nanothermites. Figure 4.5 below shows the backscattered SEM image of Al-$WO_3$ nanothermites being heated from 300-1473 K and held for 10 ms [23, 59]. Consequently, the brighter areas correspond to W/$WO_3$ while the lighter gray areas correspond to nano-aluminum.

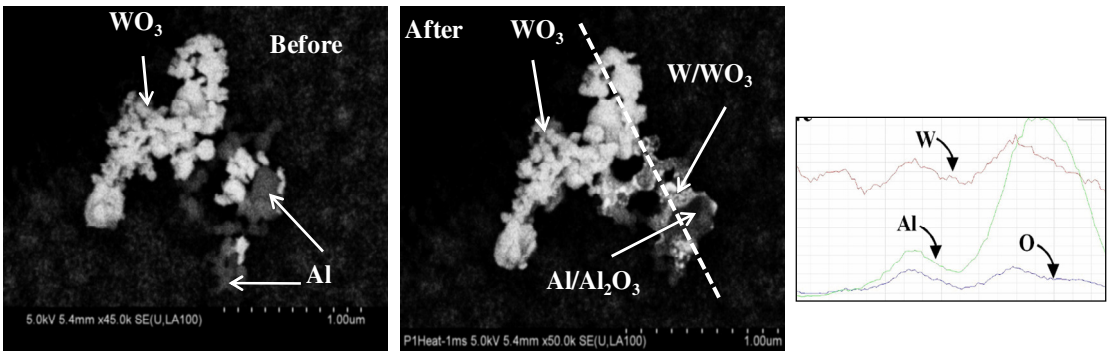


Figure 4.5 SEM image of Al/$WO_3$ nanothermites before and after heating. The heating pulse is 300-1473 K at $10^6$ K/s. Only the areas where Al is in contact with $WO_3$ seems to have undergone reaction and morphological changes. The rightmost picture shows a line scan along the dotted line shown in the middle picture and confirms that a reaction has occurred.

A few interesting features are easily identified. Noticeably only the areas where interfacial contact between aluminum and $WO_3$ exists have reacted/undergone phase change. No morphological changes are noticed in areas away from binary contacts where primarily $WO_3$ is present. This clearly indicates that the sintering is due to the reaction and not because of melting of $WO_3$. The melting point of $WO_3$ is 1746 K, which is 273 K higher than the maximum temperature of the pulse. From the context of this investigation, it is important to note that this clearly proves a condensed state reaction as no gas could be present in the low pressure SEM chamber. Furthermore, in our gas release experiments we have seen no oxygen release from $WO_3$.

Al-$Bi_2O_3$ ignites (845 K) well below their oxygen release temperature (1615 K) and below the melting point of aluminum (933 K). The aluminum core is thus in the solid phase and is fairly immobile. This makes it a strong contender for condensed phase reactions. Although not shown, aluminum is detected during the ignition tests in the T-jump TOFMS during the thermite reaction. It may be noted that we detect aluminum by heating the aluminum nanoparticles alone. Heating causes the aluminum in the core to melt and diffuse across the shell. To eliminate the possibility of aluminum being the initiating gas phase species, additional experiments are carried out by replacing aluminum with nano-sized carbon (C) powder (Cabot Inc.) which will not vaporize but has a volatile oxide ($CO_2$).

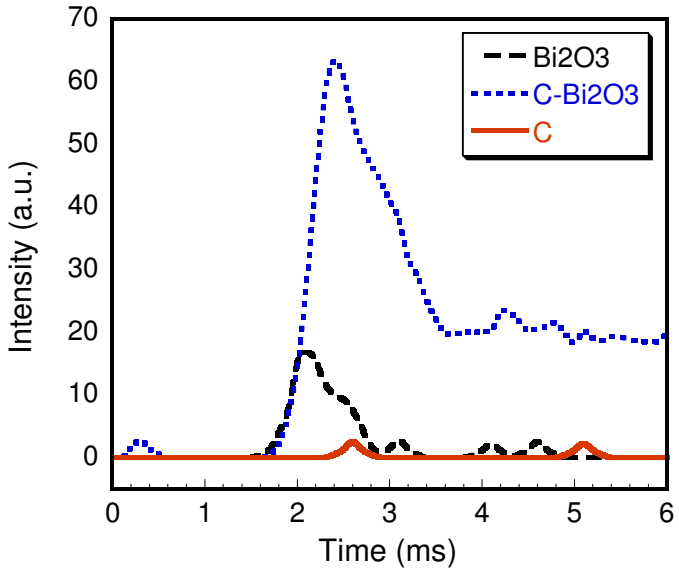


Figure 4.6 $CO_2$ release profile from $Bi_2O_3$, C powder, and C-$Bi_2O_3$ thermite under similar heating rates. The ignition temperature of C-$Bi_2O_3$ is ~ 875 K, the same as Al-$Bi_2O_3$. Reproduced from reference [66]

A careful look at Figure 4.6 shows that the $CO_2$ release from the carbon powder

occurs around 2.2 ms while the $CO_2$ release from $Bi_2O_3$ powders occurs much earlier at ~ 1.6 ms. When the C-$Bi_2O_3$ mixture is heated, the $CO_2$ release is around 1.6 ms, almost the same time when $CO_2$ is seen to come off $Bi_2O_3$. The intensity of the $CO_2$ signal from the thermite exceeds the individual oxidizer and the carbon powder and is indicative that excess $CO_2$ has been formed as a result of the reaction with the oxygen from $Bi_2O_3$ in the thermite. The $CO_2$ seen from $Bi_2O_3$ and C powders is due to the fact that they have been sonicated in hexane. Appearance of $CO_2$ in the spectra for materials sonicated in hexane is quite regular.

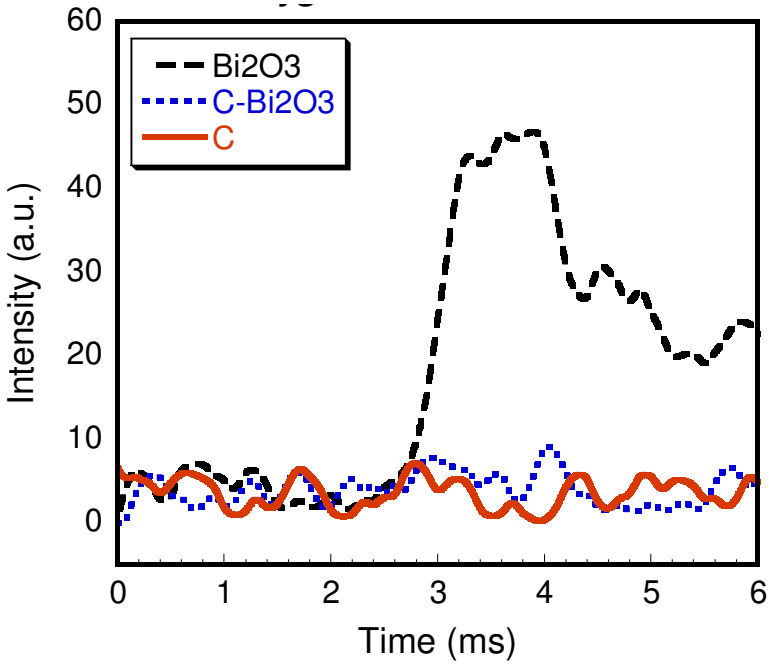


Figure 4.7 Oxygen release from T-Jump/TOFMS experiments on $Bi_2O_3$ and C powders, and the C/$Bi_2O_3$ thermite [66]

The corresponding profile for oxygen is shown below in Figure 4.7. No oxygen is

detected in the mass spectra for the C-$Bi_2O_3$ reaction while $Bi_2O_3$ shows oxygen release at around 2.5 ms. Comparing with Figure 4.5, this is after the $CO_2$ release observed from C-$Bi_2O_3$ reaction. We thus conclude that the entire oxygen has reacted with carbon, confirming a condensed state reaction. More details about Al-$Bi_2O_3$ reaction can be found in another reference [66]. It may be interesting to mention that we have also observed reaction between C-CuO, and thus eliminating the role of any gas phase aluminum as a possible initiator.

At this point we can speculate that a reactive sintering mechanism might be responsible for the initiation of the other nanothermites. $MoO_3$ and Al-$Sb_2O_3$ ignite close to their melting temperature and can thus sinter. However, in order to undergo sintering, it is not necessary to reach the melting temperature of the material. Sintering has been known to start as early as $0.5T_m$, where $T_m$ is the melting temperature [67]. The CoO formed from the decomposition of $Co_3O_4$ can only start sintering at approximately, 0.5*2103 K, i.e. 1152 K. The ignition temperature for $Co_3O_4$ is 1370 K, only about 200 K more than when it can start sintering. Similarly $SnO_2$ cannot be expected to sinter before 0.5*1903 K, i.e. 952 K. The observed ignition temperature is 1049 K, again about 100 K more. Although this does not prove reactive sintering to be the initiation mechanism, it is plausible that reactive sintering is the main initiation mode for these nanothermites. It must be emphasized that the Tammann temperature is not the sole determining factor in the initiation of the reactions. Even though the Tammann temperature for some oxidizers may be less than their ignition temperature (for example, CuO has a Tammann temperature of 678 K [68]), a reaction may not initiate until the aluminum core is molten and mobile, i.e.

until 933 K. There may be exceptions to this if the oxidizer is an excellent conductor of oxide ions enabling transport of reactive species, as is the case with Al-$Bi_2O_3$ [66, 69], and is beyond the scope of this study. The initiation of a nanothermite reaction is probably a combination of factors which includes increased mobility of molten aluminum, sintering of the reactive components and the role of ion conduction. The role of ions with regard to ignition is discussed in details in the next chapter.

## *4.5 Conclusions*

In this study we have investigated if gas phase oxygen is an essential prerequisite to the initiation of nanothermite reactions by comparing the oxygen/gas release (if any) temperature and ignition temperature for a variety of nanothermites. The oxidizers in the nanothermites are heated in the T-jump TOFMS and their oxygen release temperature were found to have a range of almost 775 K. No oxygen/gas release was detected for the oxidizers $MoO_3$, $Sb_2O_3$ and $WO_3$.

In separate T-jump TOFMS ignition experiments, we were able to measure the ignition temperature of a variety of nanothermites. A good correlation between ignition temperature and oxygen release temperature was observed for Al-CuO, Al-$Fe_2O_3$, Al-$KClO_4$ and Al-$AgIO_3$ nanothermites. Experiments conducted in a TEM on Al-CuO nanothermites however supported a condensed phase reaction. Similarly Al-$Fe_2O_3$ can ignite via reactive sintering mechanism.

Several nanothermites tested did not support the hypothesis requiring gas phase oxygen as a requirement for initiation of the nanothermite reactions. Among them, Al-$Bi_2O_3$ and Al-$SnO_2$ ignited below the oxygen release temperature from the

corresponding oxidizers, while Al-$Co_3O_4$ ignited above its oxygen release temperature. Al-$Bi_2O_3$ is known to react via condensed phase reactions. Nanothermites like Al-$MoO_3$, Al-$Sb_2O_3$ and Al-$WO_3$, where the oxidizers did not release any oxygen/gas, were seen to ignite as well showing that oxygen/gas release cannot be the sole deciding factor towards initiation of these reactions. We believe that nanothermites showing late oxygen/no oxygen release also initiated via the reactive sintering mechanism, similar to Al-$Bi_2O_3$. The essentiality of gas phase oxygen as a precursor to the initiation of a nanothermite reaction can thus be ruled out.

# Chapter 5: Correlation between Ignition and Ion Generation in Nanothermite Reactions

In the previous chapter we have established that the ignition in nanothermites is being caused as a result of condensed state reactions initiating between aluminum and the oxidizer. Some reactions are seen to occur at somewhat low temperatures. For example, Al-$Bi_2O_3$ reacted at ~ 850 K, at which temperature the core remains in the solid phase. Ionization is a phenomenon known to occur during combustion processes and a complete understanding of the reaction mechanism/propagation is often incomplete without such knowledge. More significantly, reaction characterization for nanothermites are often done via properties like flame speed, reaction rate etc. These phenomena are largely related to the ionization properties of a flame. Consequently, study of ionization during the reaction is of huge importance.

## *5.1 Background*

There is abundant literature showing that ionization is an integral part of many combustion phenomena and has been observed in several combustion systems [70-72]. Ershov [73] studied the detonation front of solid explosives such as TNT and PETN and observed high degrees of ionization. Nonthermal channels of ion generation were suggested by them as the ion density exceeded the predicted value from Saha equation by several orders of magnitude. Martirosyan et al. [74] investigated the dependence of the electric field generated during the combustion of zirconium and titanium particles and reported that a large electric field is generated

just as combustion initiated. The creation and duration of this electrical field was on the order of milliseconds (ms). Figure 5.1 below shows a plot of the electric voltage generated during the oxidation of a titanium particle of 0.8 mm diameter. The transient nature of the electric field is clearly demonstrated. The electric field is negative to begin with, during the very initial phases of heating up the particle. But once the particle ignites around 800 $^{0}$C, the electric field rapidly becomes positive. The induction time of this electric field is 18 ms while the duration of this positive voltage is about 25 ms.

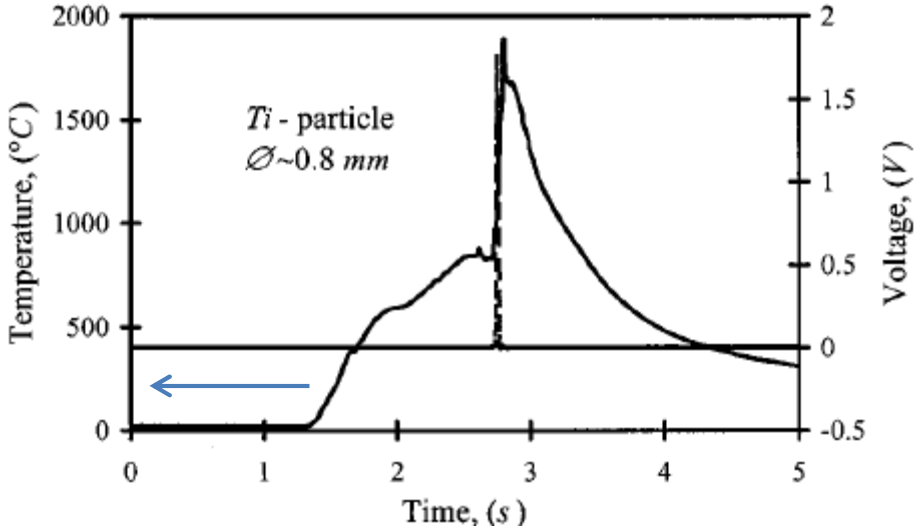


Figure 5.1 Temporal evolution of temperature and electric field during the combustion of a 800 nm titanium particle [74].

The maximum positive voltage generated is also dependent on the thickness of the oxide shell surrounding the core metal. In the same study as above, Martirosyan et al. [74] showed that the voltage generated decreases as the size of the particle is increased.

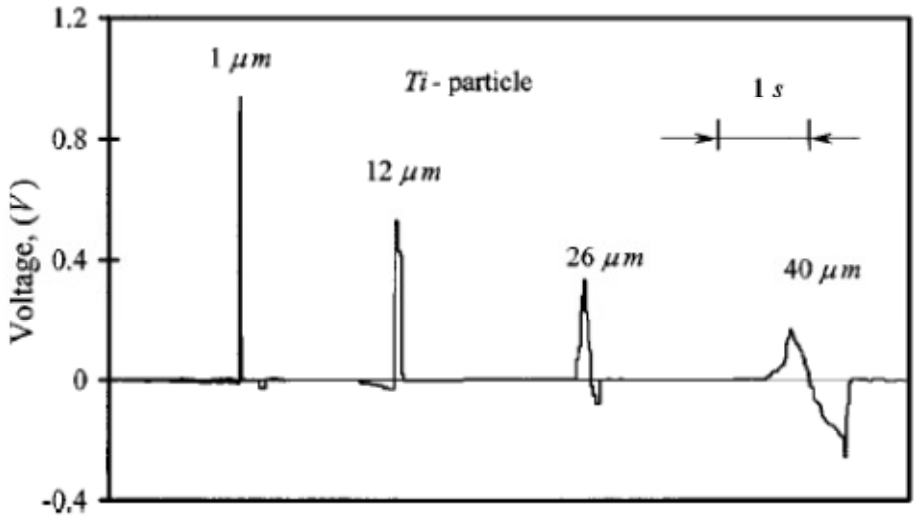


Figure 5.2 Plot showing the variation of electric field generated during combustion of different titanium particles of different sizes. Inset show a time scale for comparison of the duration of those electrical pulses [74].

Figure 5.2 above shows the electric voltage generated during the combustion of particles of increasing size as reported in reference [74]. Clearly, the intensity of the generated voltage is maximum for the smallest particle and decreases monotonically with an increase in the diameter of particles. The sharpness (gradient with respect to time) in the appearance of the electrical signal also decreases as the combusting particles are made larger in size. Thus, reactions between metal-gas can generate transient electric fields which could probably be attributed to the diffusion of ionic species across the oxide shell.

Molecular dynamics simulations on aluminum nanoparticles have been conducted in our group by Henz. and Zachariah [47]. These simulations show that strong electric fields are generated intrinsically across the oxide shell of aluminum nanoparticles.

Furthermore, the ion flux due to this built in electric field is orders of magnitude more than the Fickian diffusion. These results suggest that the electric field generated during the combustion event can be considered as an inherent parameter of the reaction. Any ignition model for a nanothermite should account for this parameter and nanothermite reactions could be initiated/controlled by applying an external field [75-77].

Studies of ionization in nanothermite reactions has been far and few. Electrical conductivity in a nanothermite flame front has been studied by Tasker et al. [78] They reported the presence of a conduction zone in the reaction front. Korogodov et al. [79] measured the pulsed microwave radiation due to the combustion of Al/$Fe_2O_3$ nanothermites and found this to be of much higher magnitude than thermal radiation.

Transient ion generation during the reaction of nanothermites has recently been studied in our group [80]. Four different nanothermites Al-CuO, Al-$Bi_2O_3$, Al-$WO_3$ and Al-$Fe_2O_3$ were tested for the relative timing/amount of positive and negative ion generated during those reactions in the T-jump time of flight mass spectrometer (T-jump TOFMS). A high speed camera was used to monitor the optical emission during the event to identify ignition. It was noticed that the positive ions were generated before/during ignition in all cases. Identification of the positive spectra led to the detection of $Na^+$ ions as the major species. Experiments were also conducted to measure the negative ion signals for the above mentioned nanothermites except for Al-$Bi_2O_3$ which caused intense arcing. It is interesting to note that the negative ion signals were typically found to be generated coincident with or after ignition. Identification of the negative ions failed as there was intense arcing due to the ion

optics. We concluded that these results pointed towards the existence of two primary means of ionization around the ignition event. The first step is the generation of positive ions and preceded/concurrent to ignition while the other one generated negative ions concurrent to/after ignition. The generation of a positive ion signal can thus serve as a precursor to ignition.

The prior investigations thus present a compelling case of the necessity to understand the ionization behavior in nanothermites and their correlation to ignition. In particular, we are interested in finding out whether the positive ion signal could always be correlated to the ignition of a wide variety of nanothermite as an alternate indicator to ignition. Consequently, the work in this chapter deals with the investigation of the positive ion pulse only and its relative appearance with respect to ignition for selected nanothermites mentioned in the section below.

## *5.2 Experimental Approach*

Three different oxidizers are used for this study. They are tin (IV) oxide ($SnO_2$), molybdenum oxide ($MoO_3$) and antimony (III) oxide ($Sb_2O_3$). In a previous study [80] oxidizers were chosen to represent the various categories with different oxygen release behaviors. In this work we include the above oxidizers which complement the previous study. $Sb_2O_3$ and $MoO_3$ do not release any gas during heating of the neat oxidizers while $SnO_2$ releases oxygen at a much higher temperature as mentioned in Chapter 4. The behavior of $Sb_2O_3$ and $MoO_3$ thus resembles the behavior of $WO_3$ (studied previously) while $SnO_2$ is similar in behavior to $Bi_2O_3$. Consequently, we expect some similarities in their behavior towards positive ion generation.

Nanothermites are prepared by mixing appropriate amounts of aluminum and the oxidizer taking into account that the aluminum is 70% active by weight. The nanothermites are put in hexane and then sonicated for about 30 minutes before being coated on a platinum wire of ~ 75 micron diameter and acts as the T-jump probe. This wire is heated by sending an electric pulse as has been detailed in Chapter 3. Only about 4-5 mm of the central portion of the platinum wire is coated and the mass of the coating is estimated to be about 0.3 mg.

The principles of operation of the T-Jump TOFMS are described in details in a previous publication [42]. The configuration for the ion optics used in this set of experiments is similar to what has been used before, except that the voltage applied to the microchannel plate (MCP) detectors is -3150 V instead of -3400 V before. Figure 5.3 below shows a schematic of the ion optics used for this experiment.

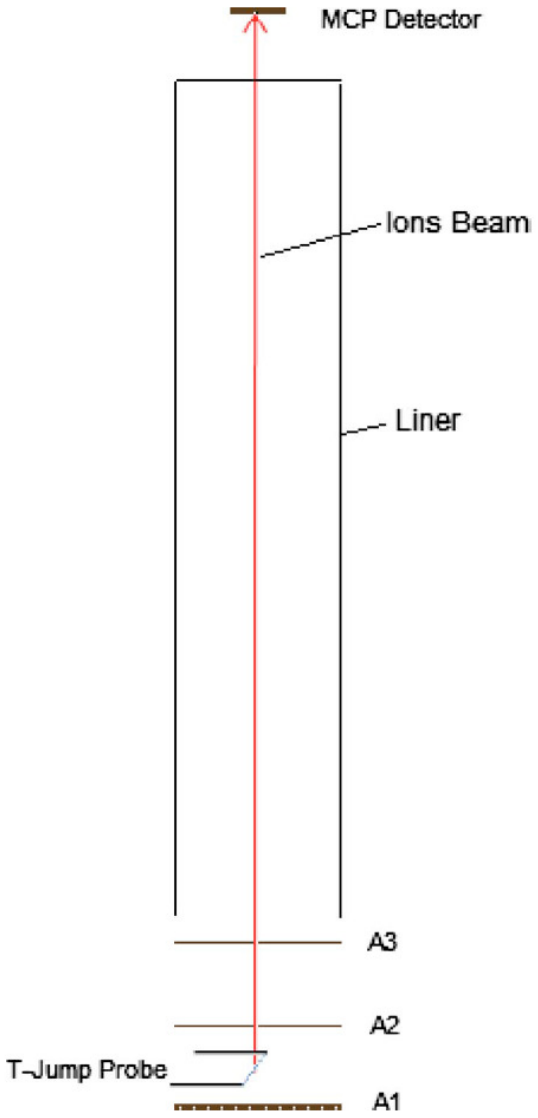


Figure 5.3 Schematic of the ion optics in the T-jump TOFMS [80].

The T-jump probe is inserted between the repeller (A1) and ground plate (A2). The extraction plate is labeled as A3. For positive ions extraction, the A1 is kept at +200 V, A2 is maintained as ground and A3 is kept at -1300 V. The electron gun is kept turned off during these experiments.

## *5.3 Results*

Figure 5.4(a) shows the positive ion signal from Al-$SnO_2$ reaction as a function of the start of the heating pulse. A sharp rise in the ion signal is observed at ~ 1.97 ms. An enlarged view of the ion peak in Figure 5.4(a) is showed in Figure 5.4(b) confirming that the positive ion signal from Al-$SnO_2$ reactions started to rise at ~ 1.97 ms. The duration of this pulse is rather short and lasts only about 150 µs.

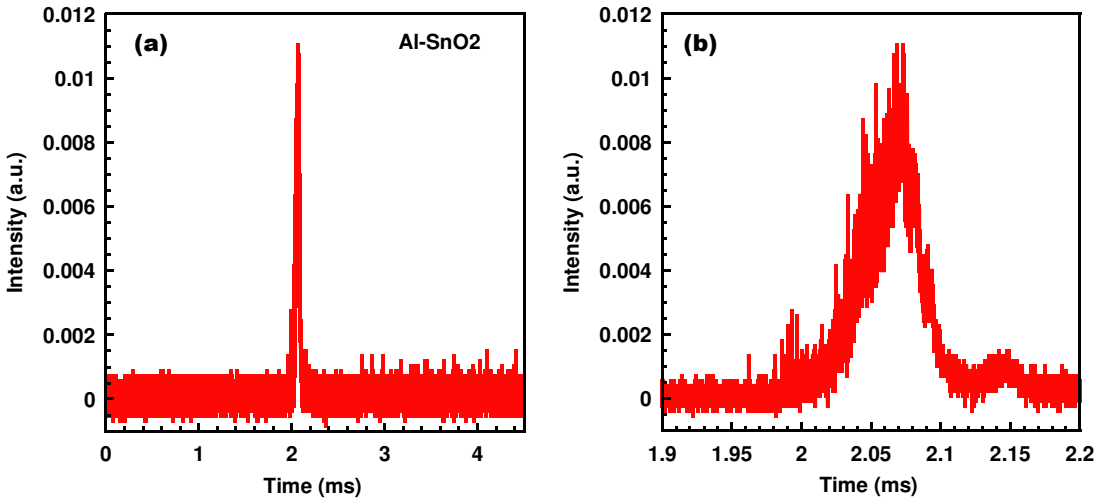


Figure 5.4 (a) Positive ion signal generated during Al-$SnO_2$ reaction. (b) An enlarged view showing the ion structure. The peak ion signal is noticed to be around 2.06 ms. The time on the abscissa represents the time since the probe was being heated.

The corresponding event as recorded by the high speed camera is shown in a few snapshots below in Figure 5.5(a)-(e). The time interval since triggering is shown in the label below each snapshot. Although, we have triggered the camera and the T-jump probe simultaneously, there is a delay of ~ 10 µs in the detection of the ion

signal due to the drift of ions inside the time-of-flight tube. However, we will neglect this difference for all the results presented here. Ignition is seen to occur around 1.968 ms as seen in Figure 5.5(a), starting at the two ends, progressing towards the center region and finally reaching the center region at 2.088 ms. Ignition thus occurs in the interval 1.968 to 2.088 ms. This is known as the ignition interval and is around 120 µs long. Comparing Figure 5.5(a) to the ion pulse shown in Figure 5.4(b), we can clearly see that ignition occurred simultaneously to the appearance of the ion pulse. This result of a one to one correspondence between the positive ion generation and ignition is similar to what has been suggested in [80]. Comparing further we see that the ion signal peaks around 2.06 ms, (some time interval between Figure 5.5(c) and (d)). However it is evident that the reaction continues even after the peak signal. For example, in Figure 5.5(e), we see the brightest plume at 2.128 ms whereas the ion signal has already decayed by the same time as noticed in Figure 5.4(b). We can thus conclude that these positive ions have been generated simultaneous to ignition and largely during the initial stages of ignition interval for Al-$SnO_2$ reactions.

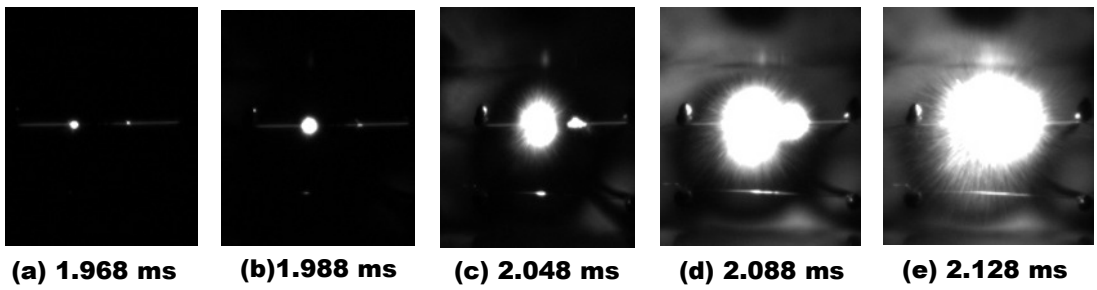


Figure 5.5(a)-(e) High speed images of Al-$SnO_2$ reaction as observed using a high speed camera. The time displayed below each snapshot is synchronized with the time on the ion

signals.

Figure 5.6(a) and (b) shows the positive ion signal and a zoomed in view of the ion signal as generated from Al-$Sb_2O_3$ reactions respectively. It could be seen that the data is noisier than Al-$SnO_2$. However, the salient features are clear and unambiguous. The ion signal starts at around 1.43 ms and continues until almost 1.75 ms for duration of 320 µs. This ion pulse thus lasts almost twice as long as the Al-$SnO_2$ pulse with the peak ion spike occurring at roughly 1.606 ms. We neglect any of the spikes that appears after 1.8 seconds as they are in no way related to ignition of the nanothermite which is our prime subject of interest.

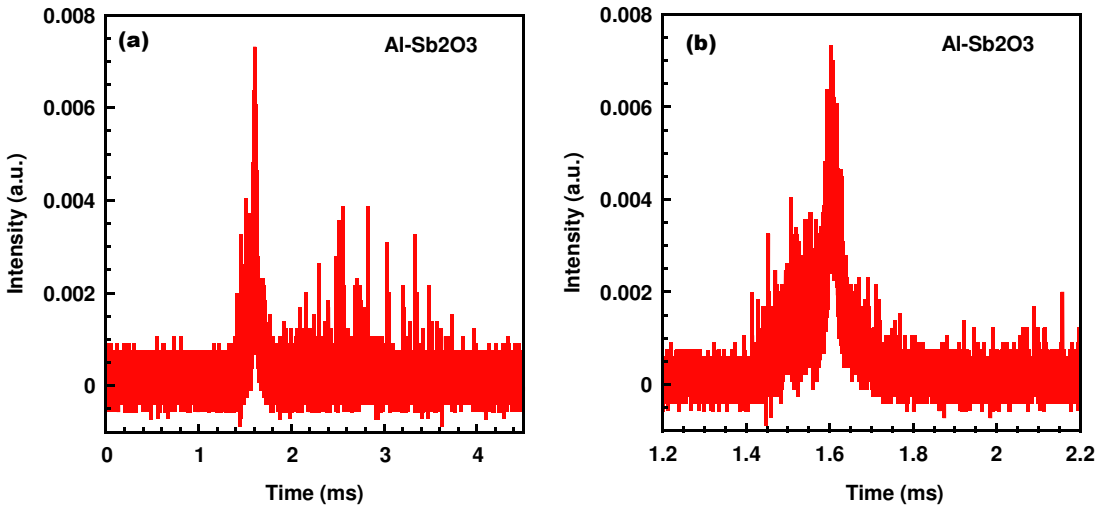


Figure 5.6 (a) Positive ion signal from Al-$Sb_2O_3$ reactions and (b) Details of the ion peak.

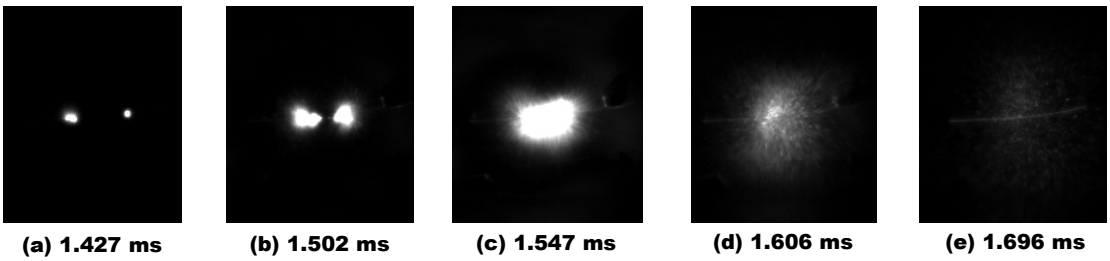


Figure 5.7(a)-(e) Images during the combustion of Al-$Sb_2O_3$. The time stamps shown below each frame correspond to the time from the start of the heating pulse.

Snapshots of the reaction of Al-$Sb_2O_3$ nanothermites is shown in Figure 5.7 above. It is seen that ignition occurs at the ends of the T-jump probe at 1.427 ms and the whole mixture has ignited by 1.547 ms. The ignition ignition interval is thus around 120 µs. Compared to the ion signal shown in Figure 5.6(b), we see that the signal appears at around 1.43 ms, around the same time as ignition occurs. The ion peak seen around 1.606 ms occurs well after the ignition interval and continues until 1.8 ms. It is clear from Figure 5.7(e) that ion generation continues until towards the very end of the combustion event. Correspondingly, we conclude that the positive ion generation starts with ignition but lasts during the entire combustion event for Al-$Sb_2O_3$. This is in stark contrast to prior results where the majority of the positive ions were reported to be generated during the initial part of the ignition interval [80] and also from what we observed for Al-$SnO_2$ nanothermites. Al-$Sb_2O_3$, where the behavior of $Sb_2O_3$ on heating is similar to $WO_3$, thus differs vastly in its positive ion generation timeframe.

The positive ion signal obtained for Al-$MoO_3$ nanothermites is shown in Figure

5.8(a). Also shown in Figure 5.8(b) is a zoomed in view of the ion structure. These ions are generated starting at ~1.6 ms after the initiation of heating and lasts until about 1.95 ms giving a duration of ~ 300 µs. It is important to note that the sharp spike in ion signal in Figure 5.8 (a) suggest strong arcing. This is entirely different from the ionization behavior for all the nanothermites as we never saw any evidence of arcing for positive ion measurement. In addition to that, the arcing was observed after the ion pulse is over, suggesting some other ion generation mechanisms.

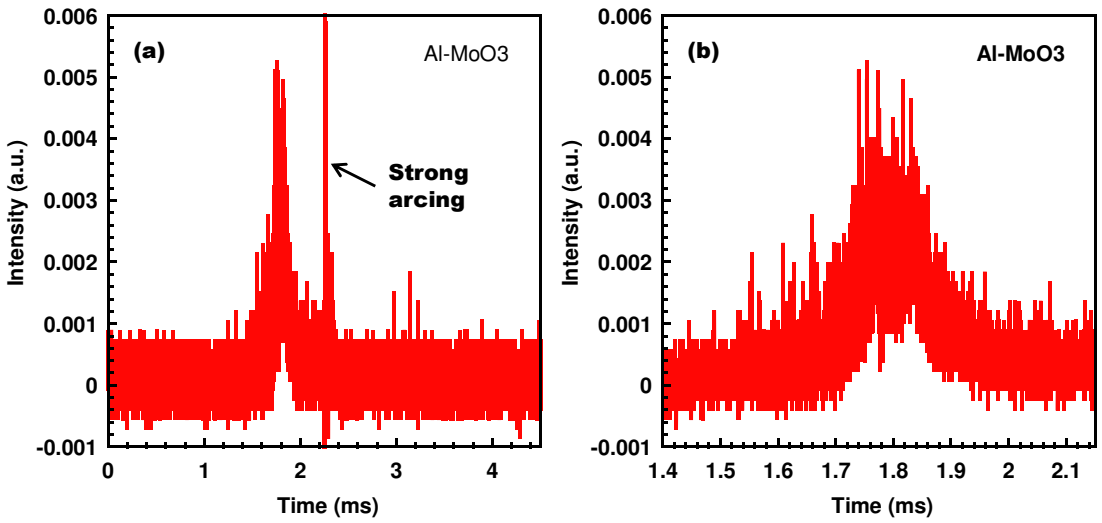


Figure 5.8 (a) Positive ion signal from Al-$MoO_3$ nanothermite reactions. A strong signal generated due to arcing is also seen subsequent to the major ion signal (b) Zoomed in view of the ion pulse.

Figure 5.9(a)-(e) below shows a few snapshots of the Al-MoO3 combustion event with ignition occuring at 1.421 ms. In this case, we can clearly see that the positive ions are generated slightly after ignition at 1.6 ms. This is just prior to the

end of the ignition interval (Figure 5.9 (d)) which is about 280 µs. However, the ion pulse is over by 2.1 ms (Figure 5.8(b)) whereas the combustion event is still ongoing. The ions are thus generated between the end of the ignition interval and before the bulk of combustion are over. It is interesting to observe that the arcing only takes place after the ions generation is over.

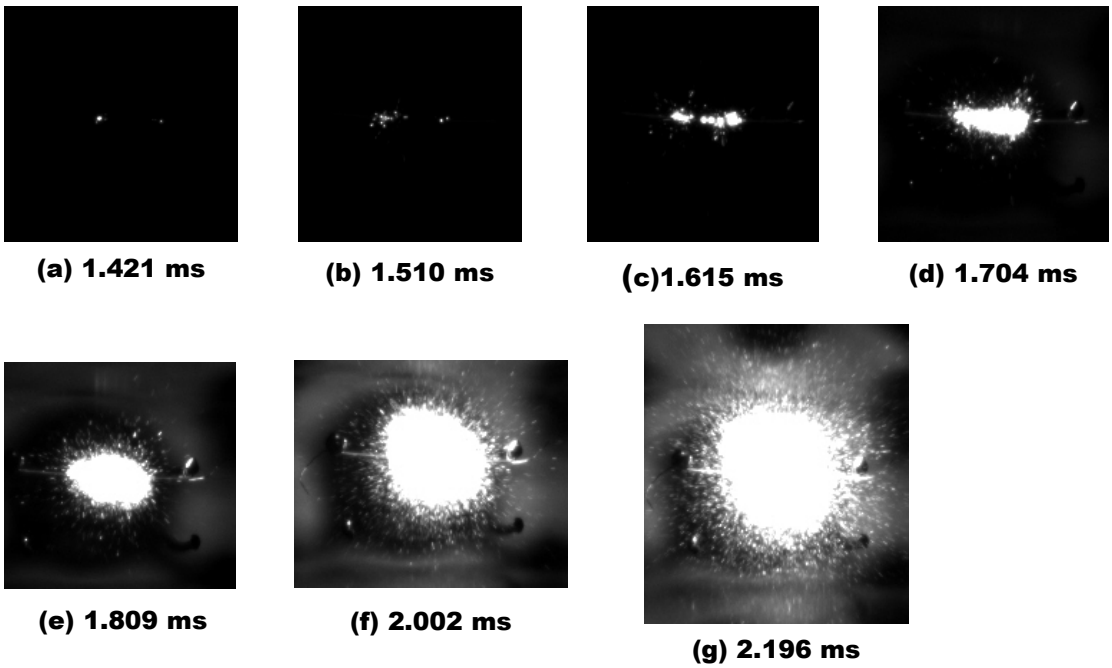


Figure 5.9 (a)-(e) Snapshots from high speed videos of Al-$MoO_3$ nanothermite reactions at different time intervals from initiation of heating.

## *5.4 Discussion*

Figure 5.4 through Figure 5.9 enables us to compare the relative appearance of the positive ion signal and its correlation to ignition. Except for Al-$MoO_3$ nanothermites, for the cases shown above, the ion signal starts to rise just when ignition occurs.

However, in all cases, we find the ion signal to appear during the ignition interval. This is in line with what has been reported for other nanothermites in reference [80] before. In general, we conclude that the appearance of the positive ion signal precedes ignition or occurs before the end of the ignition interval and could possibly be used as a measure to start the onset of reaction. These ions are therefore not a product of combustion process but are produced intrinsically during pre-ignition. When the identification of the positive mass spectra was done for Al-CuO nanothermites mentioned in [80], it was noticed that the predominant species detected is $Na^+$ ions while there are weaker peaks of $K^+$ and $Al^+$ ions. Similar results were observed for Al-$WO_3$ and Al-$Bi_2O_3$ reactions. The only exception is the presence of $Bi^+$ ions in Al-$Bi_2O_3$ reactions, suggesting stronger ionization. Due to the loss of resolution in the absence of an electron ionization source, no species could be detected for Al-$Fe_2O_3$ reactions. The strong ion pulse thus comprised mostly of Na and K salts which are present as contaminants in the reactants and are minor species on a mass basis. However, the mass spectra suggest a common underlying mechanism governing the generation of the positive ions. This is discussed in the next section.

### *5.5 Ion generation mechanism*

In chapter 3 we have showed the evidence that ignition in nanothermites is the result of a diffusion based mechanism where the reactants diffuse across the shell. We did not identify the species by mass spectrometry but qualitatively showed that diffusion time increased with the increase in shell thickness. In this chapter however, we have showed that the positive ions simultaneous to ignition. Identification of these

species by mass spectrometry in our previous work [80] has showed the presence of aluminum ions as minor species. We can thus hypothesize that the aluminum ions are probably detected due to the diffusion of aluminum ions across the shell.

Metal oxidation has long been studied by several authors [81-86]. Studies of oxidation of various metals at various temperatures have suggested a parabolic law for oxide layer growth dependence [87, 88]. Several theoretical models have also been put forward to account for the physics of metal oxidation. It is generally believed that this $t^2$ dependence is caused due to the diffusion of ions or electrons across the oxide shell due to concentration, pressure or electric gradient that exists across the oxide shell [89, 90]. This oxidation is thus controlled by a mass transport mechanism.

On the other hand, when the electric field across the oxide shell is extremely high and on the order of $10^7$ V/cm, tunneling of electrons can take place as has been suggested by the Cabrera Mott theory [91]. Transport under such circumstances is purely governed by the ion transport driven by the existing electric field across the shell [11, 92]. A modified version of Cabrera Mott model was applied to nanoparticles by Zhandov et al. [93] arguing that the effect of the induced electric field is more intense for smaller particles when compared to a flat surface. Ermoline [94] modified the model proposed by Zhandov to account for the change in volume of the core as well as the shell.

Molecular dynamics simulations of aluminum nanoparticles heated to high temperatures have shown an identical behavior. In the work of Chakraborty and Zachariah [95], a 16 nm aluminum particle with a 2 nm thick oxide shell was

simulated. The particle was stabilized at 500 K and then heated to 2000 K in 150 ps. Figure 5.10(a)-(b) shows the density of the core aluminum, shell aluminum and oxygen present in the shell at different instances of time respectively. In Figure 5.10 (a), the core-shell structure is clearly visible. The density in the core (~6 nm) is 2.7 g/cm$^3$, which is consistent with the density of bulk aluminum. The shell however has a density of ~ 3.1 g/cm$^3$ which is less than the bulk density of $Al_2O_3$ of 4 g/cm$^3$. This is primarily because the shell has increased in volume upon heating to 500 K, which is less than the melting point of aluminum. As the particle is heated to 2000 K, the aluminum core melts, becomes more mobile and diffuses out across the shell. Oxygen and aluminum from the shell would also start diffusing inwards towards the core. As the particle is kept at 2000 K, the aluminum in the core diffuses out as is evident from Figure 5.10 (b). Clearly, the simulation indicates that the at this instant of time, aluminum from the core and shell as well as shell oxygen are well mixed and cannot be distinguished. The shell can now no longer be considered to be pure alumina. It has become aluminum rich due to the movement of aluminum ions from the core. It is probable that this softens the core and permits enhanced diffusion of ions across the shell. A uniform particle consisting of core aluminum, shell aluminum and oxygen is formed eventually as plotted in Figure 5.10 (b).

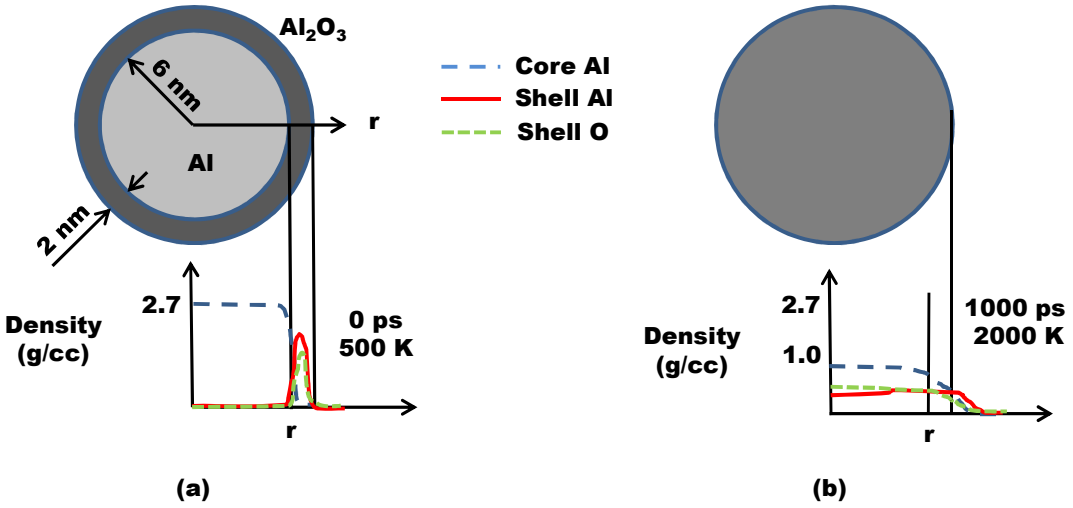


Figure 5.10 Radial density plot at different instances of time (a) 0 ps, 500 K (b) 1000 ps, 2000 K. as found in reference [95]. The movement of aluminum and oxygen is clearly noticed.

The diffusion of aluminum outwards from the core across the shell shown above does not prove whether the diffusion is due to concentration, pressure or the built in electric field. In order to understand the nature of the aluminum ions in the core and the shell, we plot the charge density of the particle. This is shown in Figure 5.11(a)-(b) to represent the charge density as a function of radial distance at the start of heating (0 ps, 500 K) and after the particle is heated to 2000 K in 150 ps respectively. The radial density profiles are shown too for comparison.

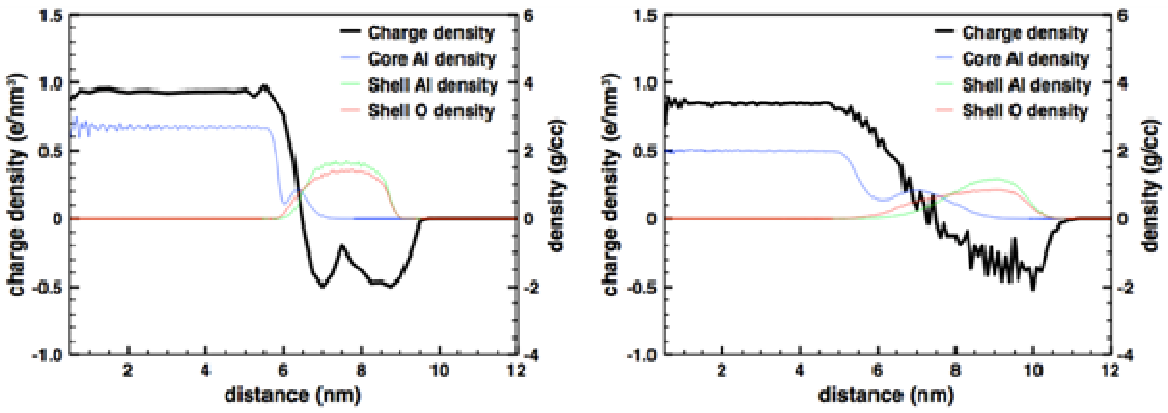


Figure 5.11 Charge density profile, averaged over 40 ps, for the aluminum particle before and after heating [95].

At the start of the simulation, both the core and the shell are charge neutral. However, as the particle was stabilized at 500 K, the core became positive and the shell became negatively charged. This charge gradient is significant at the core-shell interface as shown in Figure 5.11 (a). On the other hand, on being heated, the charge gradient becomes more diffused. Using results from Figure 5.10 (a)-(b) we conclude that this decrease in the charge density gradient is caused by the diffusion of core aluminum.

Figure 5.13 (a)-(b) for shows the radial component of the electrical field associated with the unheated and heated particle respectively. Figure 5.13(a) is at 500 K and is before the particle has been heated up. A sharp radially outwards electrical field is noticed at the interface. A positive charge at the interface would thus move radially outwards across the shell under these conditions. Since the core aluminum is present mostly as positive ions as suggested by the charge density profiles, they would tend to diffuse outwards under the influence of this electric field. This is despite the fact that

the core has not melted completely (<933 K, m.p. of Al). As the particle is heated to 2000 K, the core would melt, become more mobile which would causing it to diffuse outwards even more. While the peak value of the radial field is about 11 V/angstrom, it has decreased to 0.4 V/angstrom in Figure 5.12 (b), a factor of 27. We can thus confirm that this change in electric field is associated with the movement of aluminum ions across the shell under the influence of the strong electric field directed radially outwards at the interface. As diffusion continues further, the core shrinks and the electric field moves inwards along with the interface between the core and the shell. Eventually the electric field dissipates further and is much diminished as shown in Figure 5.12(b).

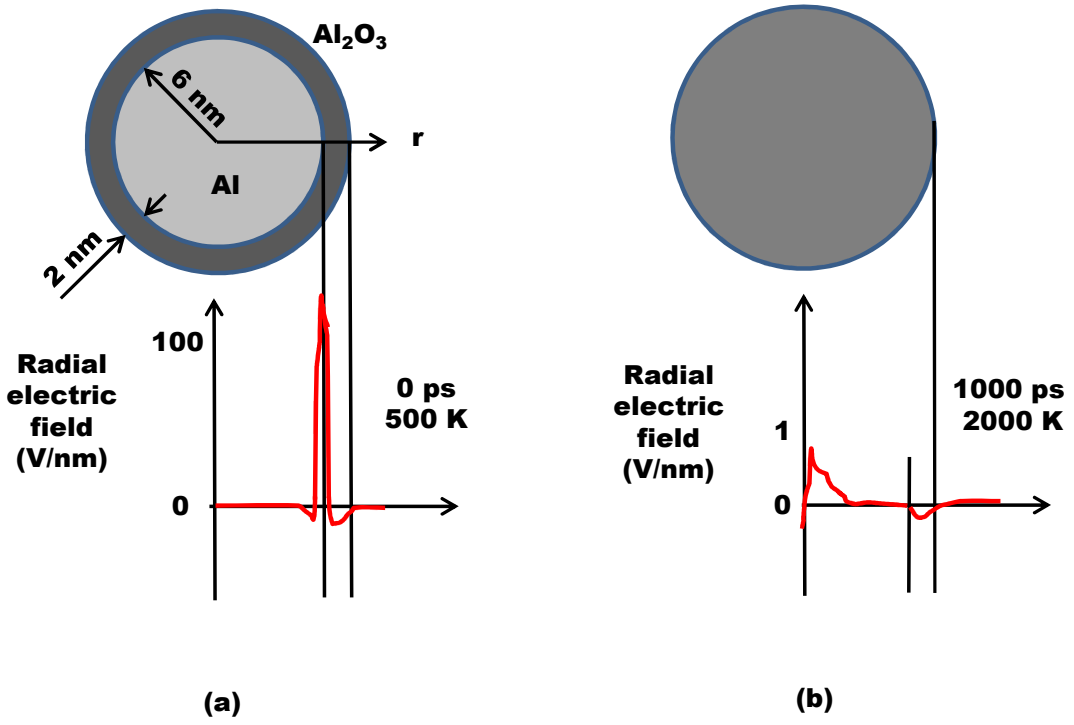


Figure 5.12 Radial component of induced electric field acting on the aluminum particle [95].

Since Chakraborty and Zachariah [93] have established through molecular dynamics simulations that aluminum ions would move outwards due to the radially outward electric field, we can start to theorize the origin of the ions during nanothermite reactions. Prior to the reaction, the nanothermites are already at high temperatures (i.e. ignition temperatures as mentioned in Chapter 4) causing the creation of an intense electric field across the oxide shell. Aluminum ions move outwards through the shell. The salts of Na and K, present as contaminants, exist on the particle surface as $Na^+$ and $K^+$. Once the aluminum ions reach the surface, these are ejected from the particle surface by electrostatic repulsion. The ion flux due to the presence of the electric field has been reported to be about ~20 moles/$cm^2$/s at 1100 K by Henz and Zachariah [47]. For larger aluminum particles, the flux could be expected to be much more significant. Correspondingly, about $10^{11}$ aluminum ions would be moving towards a single $Na^+$ and $K^+$ ions per second, causing them to be ejected from the surface [80]. This results in them being the dominant ions even though the salt contaminations are low. Additionally, the fact that the peak area under the positive ion signal found by Zhou et al. [80] is the same regardless of the nanothermite suggests that they are generated from a common source irrespective of the particle type. This was further validated by identifying the major species from mass spectra of Al-$Fe_2O_3$ mixed with sodium chloride which was found to compose of $Na^+$ ions while Al-$Fe_2O_3$ itself did not generate enough signal to identify the positive species.

## *5.6 Conclusions*

Using the T-jump/TOFMS setup we have demonstrated the formation of a strong positive ion pulse during nanothermite reactions. Measurement of the positive and ion signals generated from the reactions simultaneously with a high speed video recording suggests that positive ions are generated concurrent to ignition. Detection of the positive spectra without an electron ionization source found in literature identified $Na^+$ ions as the major species with $Al^+$ and $K^+$ ions as minor species. This was attributed to the ejection of $Na^+$ ions from the surface of aluminum particles due to the outward diffusion of charged aluminum ions in response to the strong electric field created at the interface of the core and the oxide shell. Molecular dynamics simulations from the literature are shown to support an electric field driven aluminum ion flux mechanism.

# Chapter 6: Conclusions and Future Work

## *6.1 Conclusions*

In this work we have investigated the mechanism of aluminum nanothermite ignition using the newly developed T-jump technique. Based on literature study, it was observed that there were no suitable experimental techniques to study these reactions under rapid heating conditions to mimic their behavior of these nanothermites during application conditions. Owing to this necessity, the T-jump technique was developed and is used to study the ignition behavior of aluminum nanothermites at heating rates ~ $10^5$ K/s.

Increased reactivity noticed for nanothermite reactions raises the question whether this enhancement is a consequence of a scaling behavior or due to an entirely new kinetically limited mechanism. This led us to probe the nature of the ignition mechanism using the T-jump technique for different samples of Al-CuO nanothermites. These nanothermites were identical in nature except for the oxide shell present on the aluminum nanoparticles. The samples were all heated on the T-jump probe and the electrical pulse was shut off before ignition. All the prepared samples were seen to ignite after a delay. The delay correlated well with the oxide shell thicknesses suggesting that the reactive species had to cover longer diffusion paths across the shell. This confirmed that the ignition of these nanothermites was governed by the mass transport of the reactants across the shell.

Once we have established mass diffusion to be the primary mechanism for ignition initiation, we then probed the reactivity in terms of ignition temperature of various nanothermites by changing the oxidizer. The choice of the oxidizer was governed by the behavior of the oxidizer upon heating. Equilibrium thermochemical calculations suggest that several of these oxidizers should decompose into a sub-oxide on heating with the release of gas phase oxygen. Others would melt before decomposition. The temperature of oxygen/gas release was measured by heating the oxidizers in a T-jump TOFMS while in other experiments the ignition temperature for the nanothermites are monitored using an optical detector couple to the T-jump TOFMS. Results indicate that some nanothermites like Al-CuO ignite simultaneously with gas release from the oxidizer suggesting that ignition is caused by the reaction of aluminum with gas phase oxygen. Other nanothermites (e.g. Al-$Bi_2O_3$) react before oxygen is released from the oxidizer. There are also nanothermites (e.g. Al-$WO_3$) where the oxidizer does not release any gas suggesting that condensed phase reactions may be responsible for initiation of these nanothermite reactions. To verify this assumption, high heating rate microscopy was carried out on Al-CuO, Al-$Fe_2O_3$ and Al-$WO_3$ in a special heating holder. Images suggest that large scale structures form very early during the reaction under extremely low pressure, suggesting condensed phase reactions. Reactive sintering is suggested to be the dominant mode of ignition initiation and this idea was extended to the nanothermites where no gas is released upon heating of the oxidizer concluding that gas phase oxygen is not an essential prerequisite to ignition.

The role of ion generation and transport due to electric field gradients across the alumina shell as related to ignition is also studied for selected nanothermites in the T-Jump TOFMS using a different configuration. The electron impact ionization source is turned off to allow for detection of positive ions generated from the nanothermite reactions which have been shown to occur concurrently/precede ignition. Results from our experiments indicate that positive ions are generated simultaneous to ignition for all the nanothermites tested in this work. Molecular dynamics simulations from literature supports the fact that these ions are generated by the diffusion of $Al^+$ ions from the core to the surface of the aluminum particles during heating under the intense electric field directed radially outwards from the core. We thus conclude that driven by the intrinsic electric field, positively charged aluminum ions diffuse out prior to ignition and react with the oxidizer. This does not require the role of any gas phase oxygen from the oxidizer, can occur in the condense phase and thus the results obtained in this work are self-consistent.

## *6.2 Recommendations*

### 6.2.1 In-situ microscopy

The in-situ electron microscopy experiments were restricted to only a few nanothermites due to the limited availability of the heating holders. Further experiments should be conducted on other nanothermites to verify the reactive sintering mechanism. It would also provide us with a better idea regarding the morphological changes taking place during the course of the reaction and would definitively prove the role of sintering towards ignition of nanothermites in general.

### 6.2.2 Ignition under High Pressure Conditions

Experiments conducted in the T-jump TOFMS and the electron microscope occur at extremely low pressures where the presence of gas phase oxygen is minimal. If our hypothesis about condensed phase ignition initiation is true, we should not observe any change in the ignition temperature of the nanothermite at higher pressure. Thus, it is suggested that the experiments be conducted under high pressure (say 20 bars) to see if there is any apparent shift in the ignition temperature. While a change would not necessarily mean our hypothesis is wrong, it would certainly rule out the possibility of condensed state reactions over the entire range of pressure.

### 6.2.3 Synthesis and use of perovskite materials as oxidizers

In this dissertation we have limited ourselves mostly to metal oxidizers. Metal oxidizers are usually stable until a high temperature and release oxygen by decomposition only at high temperature ~ 1000 K. However, there is a class of materials called perovskite materials which have an important material characteristic of releasing oxygen at lower temperatures. For example, LaSrCoFe perovskites have been reported to release oxygen at about 625 – 650 K. It would be interesting to see the ignition temperature for mixtures when these perovskite materials are mixed with nanoaluminum. A low ignition temperature would certainly indicate condensed phase reactions and corroborate our results.

# Appendix A.1 Calibration of Wire Temperature

The resistance of a platinum wire is well calibrated against temperature by the Callendar-Van Dusen equation [41]. The equation is given by the following equation

$$R_T = R_{T=0}(1 + 3.907x10^{-3}T - 5.91x10^{-7}T^2)$$

where $R_T$ and $R_{T=0}$ are the resistance of the wire at temperature T and 0 $^0$C and T is the temperature in degree Celsius. In order to calculate the resistance from the above formula, one needs to know the value of the resistance at T=0 $^0$C.

For any temperature calculation, it is necessary to measure the length of the wire and the $R_{T=0}$ value. Since we could not measure the value at 0 $^0$C, we measured the value of various lengths of platinum wires at laboratory temperature (20 $^0$C). Then we extrapolated this value based on the Callendar-Van Dusen equation to find out the resistance of the wire at 0 $^0$C. Figure A.1.1 below shows the measured value of the resistance at laboratory temperature using a Wheatstone bridge. The slope of the line in Figure A.1.1 gives the resistance of the wire per unit length.

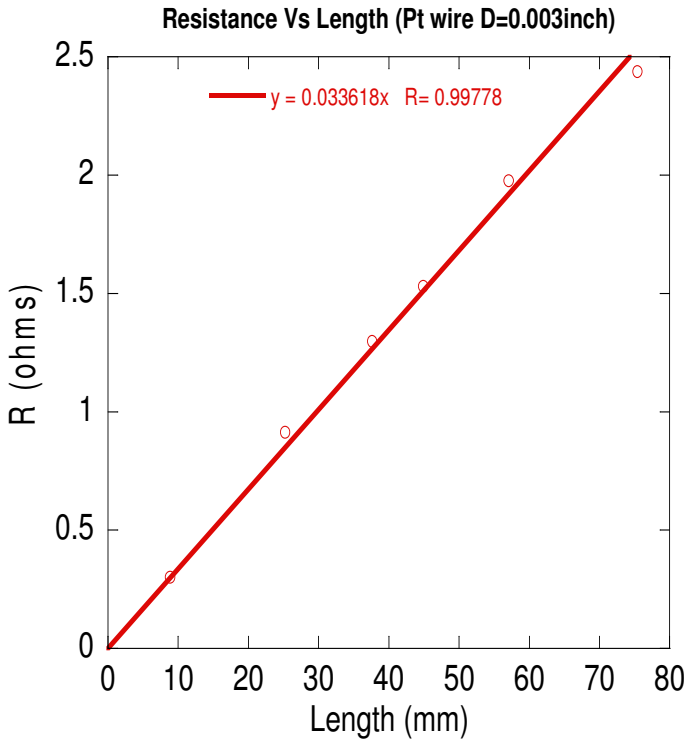


Figure A.1.1 Resistance as a function of length of the platinum wire as measured with a Wheatstone bridge. The slope represents the resistance per unit length of the wire.

Using the resistance per unit length the resistance for any length of the wire is calculated and then extrapolated to $0^0$ C. The Table A.1.1 below shows the range of values for wire lengths between 9 and 14 mm, which is typically the length of the wire used in various experiments. When the length of the wire falls in between these values, the resistance is found by interpolation.

Table A.1.1 Resistance at $0^0$C for various lengths of the platinum wire. Resistances for lengths falling in between these values are interpolated.

| Length (mm) | R @ $20^0$ C (Ω) | R @ $0^0$C (Ω) |
|---|---|---|
| 9 | 0.303 | 0.281 |
| 10 | 0.336 | 0.312 |
| 11 | 0.370 | 0.343 |
| 12 | 0.403 | 0.374 |
| 13 | 0.437 | 0.405 |
| 14 | 0.471 | 0.437 |

The equation mentioned above is however, valid only until 933 K. However the platinum wire can be heated well beyond that temperature. Consequently, two color pyrometry is used to calibrate the temperature of the wire at higher temperatures.

### *A.1.1 Two Color Pyrometry*

Pyrometry is the determination of temperature from the radiation emitted by a body. Two color pyrometry is based on the principle that the ratio of the intensity emitted at two wavelengths is constant and is only a function of temperature. For a black body, the intensity $I_{BB}$ at any given temperature T K and at a wavelength λ is governed by Planck's law of blackbody radiation.

$$I_{BB}(T, \lambda) = 2hc^2/ \lambda^5 * (e^{-hc/\lambda kT})^{-1}$$

where h is the Planck's constant, c is the velocity of light and k is the Boltzmann

constant. The intensity ratio of black body emission at a given temperature T K at two different wavelengths $\lambda_1$ and $\lambda_2$ is thus

$$I_{\lambda 1} / I_{\lambda 2} = \text{constant} = f(T)$$

The intensity ratio for a given temperature is thus fixed. However, experimentally when we use a detector to measure this intensity ratio, several other factors come into play. The spectral response of the detector material may different. To avoid this problem often two photodetectors are used for the wavelengths $\lambda_1$ and $\lambda_2$. Under those circumstances, the ratio $I_{\lambda 1} / I_{\lambda 2}$ is given by

$$I_{\lambda 1} / I_{\lambda 2} = f(T) * f(\lambda)$$

where $f(\lambda)$ is a ratio of the spectral response of the two detectors and is a known fixed value. The spectral response curve for the detectors is usually supplied by the manufacturer. The intensity ratio is a function of temperature only. The detectors could thus be calibrated against a blackbody for a range of temperatures and the intensity ratios would be known. The detectors are then used to measure the intensity ratio for the heated platinum wire with known emissivity and the temperature is determined from the intensity ratio chart.

We can now outline the steps required for the optical calibration of the temperature of the platinum wire. They are:

**Step 1**. Identification of the photodetectors and wavelengths $\lambda_1$ and $\lambda_2$

Two photo detectors procured from Thorlabs Inc. (DET 100A and DET 10C) are used for this experiment. The maximum spectral response for DET 100A is at 970 nm while that of DET 10C is at 1550 nm as outlined in the manufacturer's specification sheet based on the spectral response of the detectors. The centering was done by

placing two bandpass filters (970 ±5 nm and 1550±6 nm) right in front of the detectors. The DET 10C is an InGaAs detector with 0.8 $mm^2$ detection area while the DET 100A is a silicon detector with 75.4 $mm^2$ detection area. In order to account for this variation of detection area, a steel plate was put in front of both the detectors having a central hole of 1 mm in diameter. This is the size of the detector area on the DET 10C. Their variation in detector geometry is thus accounted for.

**Step 2**: Calibrating these detectors against a standard blackbody

The detectors mentioned above are calibrated against a NIST calibrated standard black body (MIKRON M350). The temperature of the blackbody can be set in the range between 600 C and 1100 C (873 K to 1373 K). The blackbody is turned on and allowed to stabilize in temperature for 30 minutes so that the variation in temperature is within ±2 K. The optical detectors were placed about 10 inches away from the hole of the blackbody and the optical posts were moved up and down to align the axis of the detector and the blackbody. The readings for the two detectors were recorded with an oscilloscope at intervals of 50 $^0$C.

Due to the lack of any other calibrating source beyond 1373 K, we need to extrapolate the calibration of the detectors. This is generally done by finding the fitting parameters $a_1$, $a_2$ and $a_3$ for the individual detectors using the Sakuma Hattori equation [60] given below

$$S= a_1 \exp (-c_2/ (a_2T+a_3))$$

where S is the estimated signal at a given temperature T and $c_2$ is the second Planck's radiation constant having a value of 14387.69 µm/K . The value of $a_2$ gives a representative idea of the overall behavior of the detector in terms of spectral

responsivity and $a_3$ describes the effect of temperature dependence around the central wavelength. Table A.1.2 below shows the value of the fitted parameters for the two detectors.

The fit for the detectors are shown below along with their extrapolation.

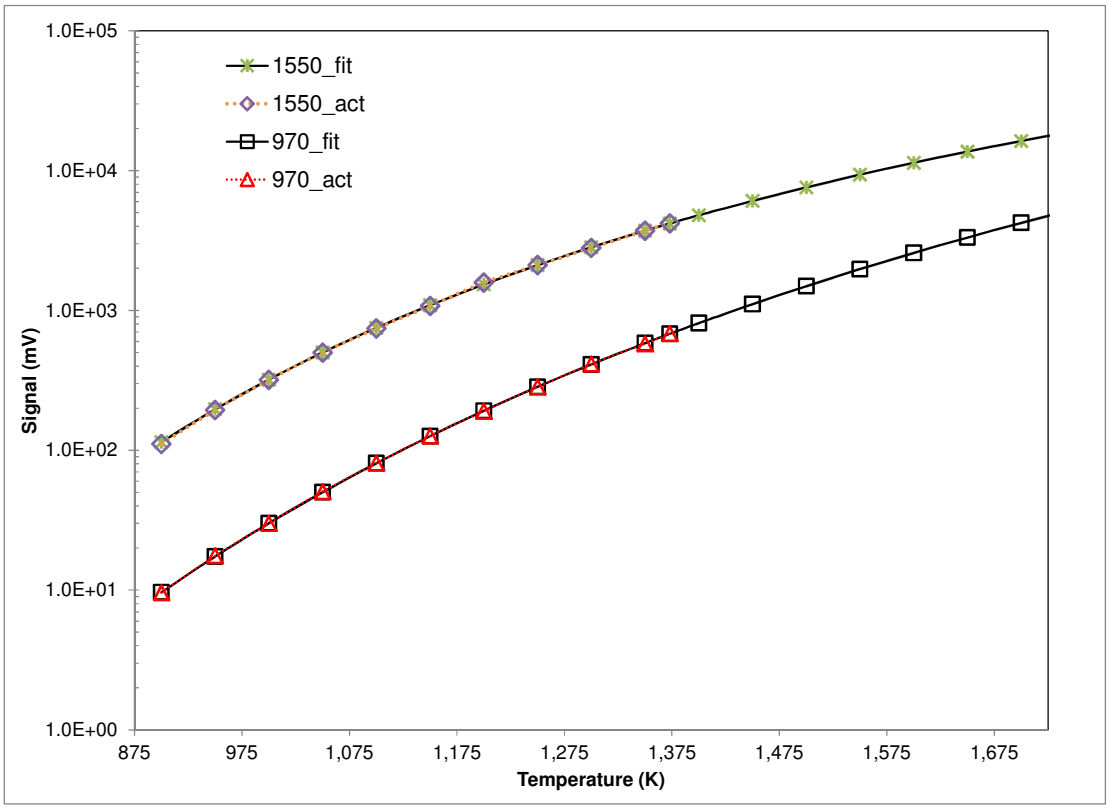


Figure A.1.2 Plot showing the measured and extrapolated values of the signal as measured for the two detectors.

Table A.1.2 Value of the parameters for the optical detectors based on curve fitting

| Detector | $a_1$ (mV) | $a_2$ (nm) | $a_3$ (µm-K) |
|---|---|---|---|
| DET 100 A | 89777600 | 684.3 | 280.75 |
| DET 10 C | 6232120 | 1374.6 | 82.25 |

The fit is seen to be very good and can be used for *estimating* the signal for the detectors at a higher temperature. However, to limit the chances of error, the extrapolation should not be done over a huge range of temperature. In our case we limit the range of extrapolation to 330 K.

The ratios of the intensity of the two detectors could thus be calculated for a series of temperatures. However, the platinum wire does not behave like a black body and has an emissivity $\varepsilon = \varepsilon(T, \lambda)$ which has temperature as well as spectral dependence. The temperature effect cancels out for each measurement as we take the ratio of the intensities. However, the variation due to wavelength does not cancel out and has to be accounted for. Based on reference [96] we assume that the ratio of the emissivity of platinum at 1550 nm is 1.3 times than that at 970 nm. Hence the intensity ratios obtained are divided further by this factor. The table below shows the calibrated intensity ratio of the detectors for a given temperature.

Table A.1.3 Table showing the calibration of the detectors with the blackbody and also the expected values of the signal.

| Source | Temp (K) | $I_{1550}$ (mV) | $I_{970}$ (mV) | $I_{1550}$/ $I_{970}$ (Ratio) | Ratio/1.3 |
|---|---|---|---|---|---|
| Blackbody | 900 | 111 | 9.6 | 11.6 | 8.9 |
| | 950 | 193 | 17 | 11.35 | 8.7 |
| | 1000 | 316 | 30 | 10.53 | 8.1 |
| | 1050 | 498 | 50 | 9.96 | 7.7 |
| | 1100 | 741 | 80 | 9.26 | 7.1 |
| | 1150 | 1070 | 124 | 8.63 | 6.6 |
| | 1200 | 1555 | 192 | 8.1 | 6.2 |
| | 1250 | 2101 | 282 | 7.45 | 5.7 |
| | 1300 | 2789 | 410 | 6.8 | 5.2 |
| | 1350 | 3673 | 578 | 6.35 | 4.9 |
| | 1373 | 4173 | 682 | 6.11 | 4.7 |
| Curve fit | 1400 | 4756 | 811 | 5.86 | 4.5 |
| | 1450 | 6028 | 1110 | 5.43 | 4.2 |
| | 1500 | 7525 | 1495 | 5.03 | 3.9 |
| | 1550 | 9264 | 1984 | 4.67 | 3.6 |
| | 1600 | 11265 | 2597 | 4.34 | 3.3 |
| | 1650 | 13539 | 3354 | 4.04 | 3.1 |

| | | | | | |
|---|---|---|---|---|---|
| | 1700 | 16104 | 4282 | 3.76 | 2.9 |

**Step 3:** Calibration of the fast heated platinum wire

For this purpose, a platinum wire is heated by a voltage pulse (22 V on the setting) and is heated to different temperature by changing the pulse width. The minimum temperature that we can calibrate by this method is governed by the sensitivity of the detectors. We start with a pulse width of 2.1 ms and increase the temperature of the pulse up to ~ 3 ms, which is typically the time frame where we see nanothermites react. Since the light emitted from the wire is really low for pulse widths of 2 ms, a lens was used to capture and focus the light on the detectors.

The procedure mentioned above is applicable to the calibrated wire only. A different platinum wire would have different length and resistance and would be heated to a different temperature. In order to eliminate this problem, we use a non-dimensional resistance of the platinum wire to calibrate against the optical intensity ratio. The non-dimensional resistance is given by $R_{max}/R_0$, where $R_{max}$ is the maximum resistance recorded at the end of the pulse. It must be noted that this non-dimensional resistance is assumed to be a function of temperature only as is done in the Callendar-Van Dusen equation. The table below describes the details of these measurements.

Table A.1.4 Details of the calibration of the wire resistance against the detector signals. 3-4 experiments were conducted for each detector corresponding to 6-8 measurements of

resistance. The typical variation in resistance at a given pulse width is ~ 2-3 %.

| Length of wire = 11.60 mm, $R_0$=0.362 Ω | | | | | | | | |
|---|---|---|---|---|---|---|---|---|
| Pulse width (ms) | $R_{max}$ (mV) | $R_{max}/R_0$ | Av. $R_{max}/R_0$ | $I_{970}$ (mV) | $I_{1550}$ (mV) | Av. $I_{970}$ (mV) | Av. $I_{1550}$ (mV) | Int. Ratio (Ratio) |
| 2.07 | 1.404 | 3.882 | 3.874 | 42 | | 43 | 264 | 6.14 |
| | 1.388 | 3.837 | | 48 | | | | |
| | 1.395 | 3.857 | | 42 | | | | |
| | 1.400 | 3.871 | | 40 | | | | |
| | 1.408 | 3.894 | | | 263 | | | |
| | 1.408 | 3.894 | | | 263 | | | |
| | 1.39 | 3.842 | | | 266 | | | |
| | 1.417 | 3.918 | | | 263 | | | |
| 2.2 | 1.440 | 3.980 | 3.983 | 69 | | 68 | 355 | 5.22 |
| | 1.434 | 3.963 | | 67 | | | | |
| | 1.434 | 3.963 | | 67 | | | | |
| | 1.440 | 3.980 | | | 346 | | | |
| | 1.455 | 4.022 | | | 362 | | | |
| | 1.443 | 3.990 | | | 356 | | | |
| 2.3 | 1.472 | 4.068 | 4.072 | 87 | | 87 | 426 | 4.90 |
| | 1.468 | 4.058 | | 86 | | | | |

| | | | | | | | | |
|---|---|---|---|---|---|---|---|---|
| | 1.486 | 4.108 | | 87 | | | | |
| | 1.469 | 4.060 | | | 422 | | | |
| | 1.472 | 4.07 | | | 432 | | | |
| | 1.472 | 4.07 | | | 424 | | | |
| | 1.508 | 4.167 | | 109 | | | | |
| | 1.503 | 4.156 | | 107 | | | | |
| | 1.529 | 4.227 | | 106 | | | | |
| 2.4 | 1.503 | 4.156 | 4.187 | | 491 | 107 | 496 | 4.64 |
| | 1.522 | 4.206 | | | 498 | | | |
| | 1.522 | 4.206 | | | 499 | | | |
| Length = 11.75 mm, $R_0$ = 0.366 Ω | | | | | | | | |
| | 1.540 | 4.204 | | 118 | | | | |
| 2.5 | 1.540 | 4.204 | 4.215 | 118 | | 119 | 523 | 4.39 |
| | 1.559 | 4.253 | | 120 | | | | |
| | 1.540 | 4.204 | | | 524 | | | |
| 2.5 | 1.544 | 4.214 | 4.215 | | 519 | 119 | 523 | 4.39 |
| | 1.543 | 4.210 | | | 526 | | | |
| | 1.574 | 4.294 | | 155 | | | | |
| | 1.574 | 4.294 | | 155 | | | | |
| 2.6 | 1.570 | 4.284 | 4.294 | 152 | | 154 | 628 | 4.08 |
| | 1.578 | 4.306 | | | 634 | | | |
| | 1.578 | 4.306 | | | 629 | | | |

| | | | | | | | | |
|---|---|---|---|---|---|---|---|---|
| | 1.570 | 4.284 | | | 622 | | | |
| 2.8 | 1.624 | 4.432 | 4.421 | 223 | | 224 | 796 | 3.55 |
| | 1.616 | 4.410 | | 225 | | | | |
| | 1.616 | 4.410 | | 224 | | | | |
| | 1.616 | 4.410 | | | 782 | | | |
| | 1.616 | 4.410 | | | 793 | | | |
| | 1.632 | 4.454 | | | 814 | | | |
| 2.9 | 1.640 | 4.477 | 4.477 | 268 | | 265 | 858 | 3.24 |
| | 1.649 | 4.499 | | 266 | | | | |
| | 1.649 | 4.499 | | 262 | | | | |
| 2.9 | 1.640 | 4.477 | 4.477 | | 871 | 265 | 858 | 3.24 |
| | 1.633 | 4.456 | | | 854 | | | |
| | 1.633 | 4.456 | | | 850 | | | |
| 3.0 | 1.693 | 4.621 | 4.595 | 338 | | 333 | 1006 | 3.02 |
| | 1.685 | 4.598 | | 334 | | | | |
| | 1.685 | 4.598 | | 326 | | | | |
| | 1.677 | 4.576 | | | 1014 | | | |
| | 1.689 | 4.610 | | | 1005 | | | |
| | 1.673 | 4.565 | | | 999 | | | |
| 3.1 | 1.736 | 4.738 | 4.708 | 409 | | 412 | 1183 | 2.87 |
| | 1.723 | 4.702 | | 419 | | | | |
| | 1.724 | 4.704 | | 410 | | | | |

| | | | | | | | | |
|---|---|---|---|---|---|---|---|---|
| | 1.723 | 4.702 | | | 1176 | | | |
| | 1.723 | 4.702 | | | 1186 | | | |
| | 1.724 | 4.704 | | | 1185 | | | |

The above measurements make it amply clear that our calibration of the wire could only be done for $R/R_0 \geq 3.874$. For any event occurring at a time corresponding to which the $R/R_0 < 3.874$, we use the Callendar-Van Dusen equation to find the temperature. Once the lower limit of the blackbody calibration is known, we can compare the intensity ratios obtained in Table A.1.4 and compare it with the intensity ratios obtained through blackbody calibration in Table A.1.3 and calculate the temperature corresponding to any given $R/R_0$. For example, let's say that an ignition event occurs corresponding to which $R/R_0 = 4.3$. From Figure A.1.3 below, we find that the corresponding intensity ratio found from our wire calibration is 4.08. Then we look for the temperature corresponding to this intensity ratio as calibrated from the black body along the secondary y-axis. The temperature at which ignition occurred is thus 1450 K.

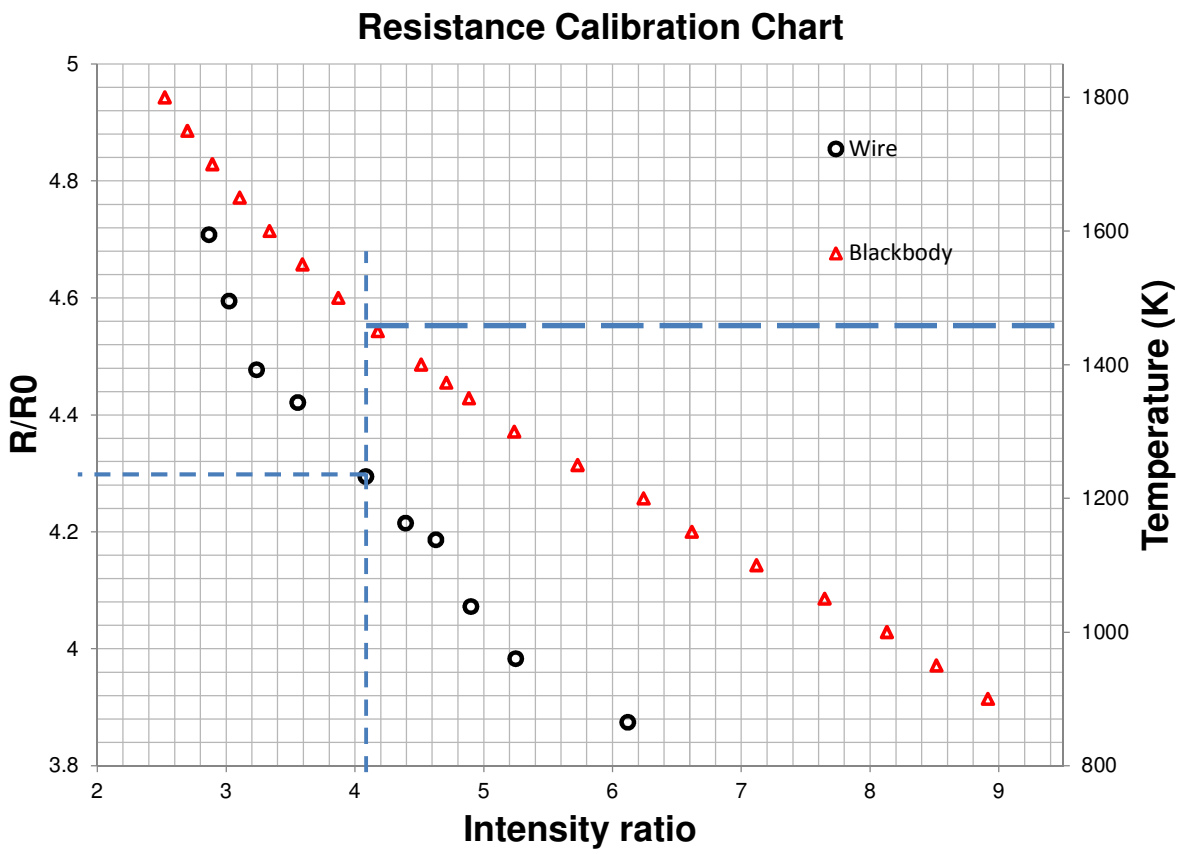


Figure A.1.3 Plot showing the temperature calibration with the resistance for the platinum wire. For any given $R/R_0$ ratio, the intensity ratio is found out from the abscissa. The temperature on the secondary y-axis corresponding to this intensity ratio is the temperature of the wire. For any $R/R_0 < 3.874$, the temperature is found out from the Callendar-Van Dusen equation.

# Bibliography


1. Fischer, S.H. and M.C. Grubelich, in *AIAA/ASME/SAE/ASEE Joint Propulsion Conference*. 1996: Lake Buena Vista, Florida.
2. Wilson, D.E. and K. Kim, *Combustion of Consolidated and Confined Metastable Intermolecular Composites*, in *43 rd AIAA Aerospace Sciences Meeting*. 2005: Reno, Nevada.
3. Aumann, C.E., G.L. Skofronick, and J.A. Martin, *Oxidation Behavior of Aluminum Nanopowders.* Journal of Vacuum Science & Technology B, 1995. **13**(3): p. 1178-1183.
4. Yetter, R.A., G.A. Risha, and S.F. Son, *Metal particle combustion and nanotechnology.* Proceedings of the Combustion Institute, 2009. **32**: p. 1819-1838.
5. Wilson, D.E. and K. Kim, *A Simplified Model for the Combustion of Al/$MoO_3$ Nanocomposite Thermites*, in *39th AIAA/ASME/SAE/ASEE Joint Propulsion Conference*. 2003: Huntsville, Alabama, USA.
6. Huang, Y., et al., *Combustion of bimodal nano/micron-sized aluminum particle dust in air.* Proceedings of the Combustion Institute, 2007. **31**: p. 2001-2009.
7. Huang, Y., et al., *Effect of particle size on combustion of aluminum particle dust in air.* Combustion and Flame, 2009. **156**(1): p. 5-13.
8. Sullivan, K., *Ignition, Combustion and Tuning of Nanocomposite Thermites*. 2010, University of Maryland: College Park.
9. Levitas, V.I., M.L. Pantoya, and B. Dikici, *Melt dispersion versus diffusive oxidation mechanism for aluminum nanoparticles: Critical experiments and controlling parameters.* Applied Physics Letters, 2008. **92**(1).
10. Levitas, V.I., et al., *Melt dispersion mechanism for fast reaction of nanothermites.* Applied Physics Letters, 2006. **89**(7).
11. Rai, A., et al., *Understanding the mechanism of aluminium nanoparticle oxidation.* Combustion Theory and Modelling, 2006. **10**(5): p. 843-859.
12. Trunov, M.A., M. Schoenitz, and E.L. Dreizin, *Effect of polymorphic phase transformations in alumina layer on ignition of aluminium particles.* Combustion Theory and Modelling, 2006. **10**(4): p. 603-623.
13. Trunov, M.A., et al., *Effect of polymorphic phase transformations in Al2O3 film on oxidation kinetics of aluminum powders.* Combustion and Flame, 2005. **140**(4): p. 310-318.
14. Dreizin, E.L., *Metal-based reactive nanomaterials.* Progress in Energy and Combustion Science, 2009. **35**(2): p. 141-167.
15. Pantoya, M.L. and J.J. Granier, *The effect of slow heating rates on the reaction mechanisms of nano and micron composite thermite reactions.* Journal of Thermal Analysis and Calorimetry, 2006. **85**(1): p. 37-43.
16. Sun, J., M.L. Pantoya, and S.L. Simon, *Dependence of size and size distribution on reactivity of aluminum nanoparticles in reactions with oxygen and MoO3.* Thermochimica Acta, 2006. **444**(2): p. 117-127.

17. Umbrajkar, S.M., M. Schoenitz, and E.L. Dreizin, *Exothermic reactions in Al-CuO nanocomposites.* Thermochimica Acta, 2006. **451**(1-2): p. 34-43.
18. Bockmon, B.S., et al., *Combustion velocities and propagation mechanisms of metastable interstitial composites.* Journal of Applied Physics, 2005. **98**(6).
19. Bockmon, B.S., et al. *Burn rate Measurements of Nanocomposite Thermites*. in *41st Aerospace Sciences Meeting and Exhibit*. 2003. Reno, Nevada, U.S.A.
20. Bazyn, T., H. Krier, and N. Glumac, *Combustion of nanoaluminum at elevated pressure and temperature behind reflected shock waves.* Combustion and Flame, 2006. **145**(4): p. 703-713.
21. Bazyn, T., et al., *Reflected shock ignition and combustion of aluminum and nanocomposite thermite powders.* Combustion Science and Technology, 2007. **179**(3): p. 457-476.
22. Hunt, E.M. and M.L. Pantoya, *Ignition dynamics and activation energies of metallic thermites: From nano- to micron-scale particulate composites.* Journal of Applied Physics, 2005. **98**(3).
23. Sullivan, K.T., et al., *In situ microscopy of rapidly heated nano-Al and nano-Al/WO3 thermites.* Applied Physics Letters, 2010. **97**(13).
24. Puri, P. and V. Yang, *Effect of particle size on melting of aluminum at nano scales.* Journal of Physical Chemistry C, 2007. **111**(32): p. 11776-11783.
25. Alavi, S., J.W. Mintmire, and D.L. Thompson, *Molecular dynamics simulations of the oxidation of aluminum nanoparticles.* Journal of Physical Chemistry B, 2005. **109**(1): p. 209-214.
26. Moore, K., M.L. Pantoya, and S.F. Son, *Combustion behaviors resulting from bimodal aluminum size distributions in thermites.* Journal of Propulsion and Power, 2007. **23**(1): p. 181-185.
27. Bulian, C.J., T.T. Kerr, and J.A. Puszynski. *Ignition Studies of Aluminum and Metal Oxide Nanopowders*. in *31st International Pyrotechnics Seminar*. 2004. Fort Collins, Colorado, USA.
28. Glassman, I. and R.A. Yetter, *Combustion*. 4th ed. 2003: Academic Press.
29. Dreizin, E.L., *Experimental study of stages in aluminum particle combustion in air.* Combustion and Flame, 1996. **105**(4): p. 541-556.
30. Friedman, R. and A. Macek, *Ignition and Combustion of Aluminum in Hot Ambient Gases.* Combustion and Flame, 1962. **6**(1): p. 9-19.
31. Merzhanov, A.G., Y.M. Grigorjev, and Y.A. Galchenko, *Aluminum Ignition.* Combustion and Flame, 1977. **29**(1): p. 1-14.
32. Trunov, M.A., M.Schoenitz, and E.L. Dreizin, in *Joint Meeting of the U.S. Sections of the Combustion Institute*. 2005: Philadelphia, Pennsylvania, U.S.A.
33. Levenspiel, O., *Chemical reaction Engineering*. 3rd ed. 1999, New York: John Wiley.
34. Trunov, M.A., M. Schoenitz, and E.L. Dreizin, *Ignition of aluminum powders under different experimental conditions.* Propellants Explosives Pyrotechnics, 2005. **30**(1): p. 36-43.
35. Park, K., et al., *Size-resolved kinetic measurements of aluminum nanoparticle oxidation with single particle mass spectrometry.* Journal of Physical Chemistry B, 2005. **109**(15): p. 7290-7299.

36. Rai, A., et al., *Importance of phase change of aluminum in oxidation of aluminum nanoparticles.* Journal of Physical Chemistry B, 2004. **108**(39): p. 14793-14795.
37. Mahadevan, R., et al., *Measurement of condensed-phase reaction kinetics in the aerosol phase using single particle mass spectrometry.* Journal of Physical Chemistry A, 2002. **106**(46): p. 11083-11092.
38. Ortega, A., *The kinetics of solid-state reactions toward consensus - Part I: Uncertainties, failures, and successes of conventional methods.* International Journal of Chemical Kinetics, 2001. **33**(6): p. 343-353.
39. Campbell, T., et al., *Dynamics of oxidation of aluminum nanoclusters using variable charge molecular-dynamics simulations on parallel computers.* Physical Review Letters, 1999. **82**(24): p. 4866-4869.
40. Levitas, V.I., *Burn time of aluminum nanoparticles: Strong effect of the heating rate and melt-dispersion mechanism.* Combustion and Flame, 2009. **156**(2): p. 543-546.
41. Childs, P.R.N., *Practical Temperature Measurement*. 2001: Butterworth-Heineman.
42. Zhou, L., et al., *T-Jump/time-of-flight mass spectrometry for time-resolved analysis of energetic materials.* Rapid Communications in Mass Spectrometry, 2009. **23**(1): p. 194-202.
43. Zhou, L., et al., *Time-Resolved Mass Spectrometry of the Exothermic Reaction between Nanoaluminum and Metal Oxides: The Role of Oxygen Release.* Journal of Physical Chemistry C, 2010. **114**(33): p. 14269-14275.
44. Ward, T.S., et al., *Experimental methodology and heat transfer model for identification of ignition kinetics of powdered fuels.* International Journal of Heat and Mass Transfer, 2006. **49**(25-26): p. 4943-4954.
45. Levitas, V.I., M.L. Pantoya, and K.W. Watson, *Melt-dispersion mechanism for fast reaction of aluminum particles: Extension for micron scale particles and fluorination.* Applied Physics Letters, 2008. **92**(20).
46. Nakamura, R., et al., *Hollow oxide formation by oxidation of Al and Cu nanoparticles.* Journal of Applied Physics, 2007. **101**(7).
47. Henz, B.J., T. Hawa, and M.R. Zachariah, *On the role of built-in electric fields on the ignition of oxide coated nanoaluminum: Ion mobility versus Fickian diffusion.* Journal of Applied Physics. **107**(2).
48. Young, G., et al., *Combustion characteristics of boron nanoparticles.* Combustion and Flame, 2009. **156**(2): p. 322-333.
49. Mason, B.A., et al. *Silicon-Based Nanoenergetic Composites*. in *Proceedings of the 6th U.S. Combustion Meeting*. 2009.
50. Sullivan, K. and M.R. Zachariah, *Simultaneous Pressure and Optical Measurements of Nanoaluminum Thermites: Investigating the Reaction Mechanism.* Journal of Propulsion and Power, 2010. **26**(3): p. 467-472.
51. Granier, J.J. and M.L. Pantoya, *Laser ignition of nanocomposite thermites.* Combustion and Flame, 2004. **138**(4): p. 373-383.
52. Sanders, V.E., et al., *Reaction propagation of four nanoscale energetic composites (Al/MoO3, Al/WO3, Al/CuO, and Bi2O3).* Journal of Propulsion and Power, 2007. **23**(4): p. 707-714.

53. Schoenitz, M., S. Umbrajkar, and E.L. Dreizin, *Kinetic analysis of thermite reactions in Al-MoO3 nanocomposites.* Journal of Propulsion and Power, 2007. **23**(4): p. 683-687.
54. Son, S.F., et al., *Combustion of nanoscale Al/MoO3 thermite in microchannels.* Journal of Propulsion and Power, 2007. **23**(4): p. 715-721.
55. Puszynski, J.A., C.J. Bulian, and J.J. Swiatkiewicz, *Processing and ignition characteristics of aluminum-bismuth trioxide nanothermite system.* Journal of Propulsion and Power, 2007. **23**(4): p. 698-706.
56. Kaplowitz, D.A., R.J. Jouet, and M.R. Zachariah, *Aerosol synthesis and reactive behavior of faceted aluminum nanocrystals.* Journal of Crystal Growth. **312**(24): p. 3625-3630.
57. Apperson, S., et al., *Generation of fast propagating combustion and shock waves with copper oxide/aluminum nanothermite composites (vol 91, art no 243109, 2008).* Applied Physics Letters, 2008. **92**(22).
58. Chowdhury, S., et al., *Diffusive vs Explosive Reaction at the Nanoscale.* Journal of Physical Chemistry C, 2010. **114**(20): p. 9191-9195.
59. Sullivan, K., et al., *Reactive Sintering : An important Concept in the Combustion of Nanocomposite Thermites.* Combustion and Flame, 2012. **159**(1): p. 2-15.
60. Saunders, P. and D.R. White, *Physical basis of interpolation equations for radiation thermometry.* Metrologia, 2003. **40**(4): p. 195-203.
61. Gordon, S. and B.J. McBride, *Computer Program for Calculation of Complex Chemical Equilibrium Compositions and Analysis*. 1994, NASA RP-1311: Washington D.C., U.S.A.
62. Stern, K.H., *High Temperature Properties and Thermal Decomposition of Inorganic Salts with Oxyanions*. 2000, Boca Raton, Florida, USA: CRC Press.
63. Haynes, W.M., *CRC Handbook of Chemistry and Physics*. 92 ed. 2011-2012.
64. Pourmortazavi, S.M., et al., *Thermal behavior of aluminum powder and potassium perchlorate mixtures by DTA and TG.* Thermochimica Acta, 2006. **443**(1): p. 129-131.
65. 3.0, I.D.o.T.V.V.,2001.
66. Piekiel, N., et al., *Initiation and reaction in Al/$Bi_2O_3$ nanothermites: Evidence for Condensed Phase Chemistry (unpublished results).*
67. Satterfield, C.N., *Heterogeneous catalysis in industrial practice*. 2nd ed. 1991.
68. Siriwardane, R., et al., *Evaluation of reaction mechanism of coal-metal oxide interactions in chemical-looping combustion.* Combustion and Flame, 2010. **157**(11): p. 2198-2208.
69. Shuk, P., et al., *Oxide ion conducting solid electrolytes based on Bi2O3.* Solid State Ionics, 1996. **89**(3-4): p. 179-196.
70. Fialkov, A.B., *Investigations on ions in flames.* Progress in Energy and Combustion Science, 1997. **23**(5-6): p. 399-528.
71. Filimonov, I. and D. Luss, *High-temperature oxidation of a metal particle: Nonisothermal model.* Aiche Journal, 2005. **51**(5): p. 1521-1531.
72. Filimonov, I.A. and N.I. Kidin, *High-temperature combustion synthesis: Generation of electromagnetic radiation and the effect of external electromagnetic fields (review).* Combustion Explosion and Shock Waves,

2005. **41**(6): p. 639-656.
73. Ershov, A.P., *Ionization During Detonation of Solid Explosives.* Combustion Explosion and Shock Waves, 1975. **11**(6): p. 798-803.
74. Martirosyan, K.S., et al., *Electric field formation during combustion of single metal particles.* Journal of the Electrochemical Society, 2003. **150**(5): p. J9-J16.
75. Carleton, F.B. and F.J. Weinberg, *Electric Field -Induced Flame Convection in the Absence of Gravity.* Nature, 1987. **330**(6149): p. 635-636.
76. Ewald, K.H., U. Anselmi-Tamburini, and Z.A. Munir, *A finite difference model for the combustion of zirconium in oxygen.* Journal of Materials Research, 2000. **15**(9): p. 1922-1935.
77. Munir, Z.A., *The effect of external electric fields on the nature and properties of materials synthesized by self-propagating combustion.* Materials Science and Engineering a-Structural Materials Properties Microstructure and Processing, 2000. **287**(2): p. 125-137.
78. Tasker, D.G., et al., *Dynamic measurements of electrical conductivity in metastable intermolecular composites.* Journal of Applied Physics, 2006. **99**(2).
79. Korogodov, V.S., et al., *Microwave radiation from combustion of an iron-aluminum thermite mixture.* Combustion Explosion and Shock Waves, 2005. **41**(4): p. 481-483.
80. Zhou, L., et al., *Transient ion ejection during nanocomposite thermite reactions.* Journal of Applied Physics, 2009. **106**(8).
81. Roberts, M.W., *Metal Oxidation.* Quarterly Reviews, 1962. **16**(1): p. 71-99.
82. Fromhold, A.T., *Justification of Local Space-Charge Neutrality Hypothesis in Metal Oxidation.* Physics Letters A, 1976. **58**(2): p. 118-120.
83. Fromhold, A.T., *Metal Oxidation from the Viewpoint of a Physicist.* Abstracts of Papers of the American Chemical Society, 1986. **191**: p. 10-COLL.
84. Fromhold, A.T., *Metal Oxidation-Kinetics from the Viewpoint of a Physicist - The Microscopic Motion of Charged Defects Through Oxides.* Langmuir, 1987. **3**(6): p. 886-896.
85. Wagner, C., *50 Years Research on Oxidation of Metals and Alloys - Retrospect and Prospect.* Journal of the Electrochemical Society, 1970. **117**(8): p. C251-&.
86. Wang, W.Q., et al., *Effects of oxide-shell structures on the dynamics of oxidation of Al nanoparticles.* Applied Physics Letters. **96**(18).
87. Fromhold, A.T., *Parabolic Oxidation of Metals.* Physics Letters A, 1969. **A 29**(3): p. 157-&.
88. Fromhold, A.T., *Parabolic Oxidation of Metals in Homogeneous Electric-Fields.* Journal of Physics and Chemistry of Solids, 1972. **33**(1): p. 95-&.
89. Atkinson, A., *Grain-Boundary Diffusion-Structural Effects and Mechanisms.* Journal De Physique, 1985. **46**(NC-4): p. 379-391.
90. Atkinson, A., *Diffusion-Processes in Oxides.* Annales De Chimie-Science Des Materiaux, 1985. **10**(3): p. 245-256.
91. Cabrera, N. and N.F. Mott, *Theory of the Oxidation of Metals.* Reports on Progress in Physics, 1948. **12**: p. 163-184.

92. Fromhold, A.T. and E.L. Cook, *Kinetics of Oxide Film Growth on Metal Crystals - Electronic and Ionic Diffusion in Large Surface-Charge and Space-Charge Fields.* Physical Review, 1968. **175**(3): p. 877.
93. Zhdanov, V.P. and B. Kasemo, *Cabrera-Mott kinetics of oxidation of nm-sized metal particles.* Chemical Physics Letters, 2008. **452**(4-6): p. 285-288.
94. Ermoline, A. and E.L. Dreizin, *Equations for the Cabrera-Mott kinetics of oxidation for spherical nanoparticles.* Chemical Physics Letters. **505**(1-3): p. 47-50.
95. Chakraborty, P. and M.R. Zachariah, *Do Nanoparticles Remain Nano-sized During Combustion*. manuscript in preparation.
96. Deemyad, S. and I.F. Silvera, *Temperature dependence of the emissivity of platinum in the IR.* Review of Scientific Instruments, 2008. **79**(8).